Charging phenomena in single molecules and ordered molecular islands

DISSERTATION ZUR ERLANGUNG DES DOKTORGRADES
DER NATURWISSENSCHAFTEN (DR. RER. NAT.)
DER FAKULTÄT FÜR PHYSIK

DER UNIVERSITÄT REGENSBURG

vorgelegt von:
Philipp Thomas Scheuerer
aus Regensburg

Im Jahr 2020

Das Promotionsgesuch wurde am 15. Januar 2020 eingereicht.
Die Arbeit wurde von Prof. Dr. Jascha Repp angeleitet.

Prüfungsausschuss:

Vorsitzender:	Prof. Dr. Jörg Wunderlich
1. Gutachter:	Prof. Dr. Jascha Repp
2. Gutachter:	PD Dr. Andrea Donarini
Weiterer Prüfer:	Prof. Dr. John Lupton

Contents

1 Introduction

Electron transfer is ubiquitous in nature and plays a central role, for example, in chemical reactions such as photosynthesis or corrosion, as well as organic light-emitting diodes, transistors, and photovoltaic devices.
Even though electron transfer processes are generally well understood, their investigation at the atomic-scale could provide novel insights and push forward the ongoing development of organic electronics.

Scanning tunneling microscopy (STM) and atomic force microscopy (AFM) have made tremendous progress since their invention in the 1980s [1, 2]. Especially within the past 20 years, those techniques have become powerful tools for atomic-scale surface characterization, and in particular, for the investigation of single atoms or molecules and their properties in real space.
Already shortly after its invention, STM was used to controllably move single Xe atoms on a metallic surface [3]. Another impressive example was the measurement of vibrational and rotational excitations of single molecules, adsorbed on a surface [4, 5]. After it was found that ultra-thin insulating films can be used to decouple a molecule from the supporting conductive substrate [6], scanning tunneling microscopy has been exploited for electronic structure investigations of single molecules, for example, to map the frontier orbitals of an individual molecule [6]. One of the most relevant applications of STM for this thesis is the possibility to resolve and manipulate charge states of single atoms and molecules [7, 8]. This possibility of charge state control was utilized to derive the distribution of an excess electron within a molecule, based on the electron's impact on the tunneling barrier [8].

Also, AFM has provided fascinating insights into physical and chemical processes at the atomic scale. Whereas STM primarily measures the electronic properties of single molecules, the strength of atomic force microscopy is its sensitivity to the geometric structure of single molecules, which makes those two techniques complementary. The discovery that AFM with CO-functionalized tips enables to resolve the details of the chemical structure within single molecules represents another recent breakthrough [9]. This technique was proven to be even sensitive enough to distinguish bond order differences within single molecules [10].
Furthermore, it was shown that charge states of single molecules can be resolved and manipulated by means of AFM [11]. Recently, it was demonstrated how bond orders within a molecule change upon charging by combining the ability of charge manipulation and structural resolution [12].
Those examples show that STM and AFM, in combination, provide us with a com-

plete toolbox for the investigation of electron transfer processes within single molecules.

In this thesis, we make use of STM and AFM to study and resolve the structural and electronic effects accompanying electron transfer reactions within single molecules and small ordered islands of molecules with atomic-scale resolution. The experiments, which will be presented in this thesis, can be divided into three projects:

The effect of charging on the geometric structure of a single molecule.
In chapter 4, AFM experiments of individual molecules adsorbed on ultrathin NaCl films, which were grown on a supporting metal surface, are presented. Individual molecules were controllably switched between two different charge states using scanning probe microscopy. We acquired AFM images of single molecules in both charge states and analyzed the differences in image contrast. From those contrast changes in AFM images due to charging and supporting density functional theory (DFT) simulations, the geometrical changes of a molecule upon charging were elucidated.

The stability of electron distributions within molecular islands in different charge states, and the role of electrostatic interactions.
Chapter 6 is the main project of this thesis. For these experiments, we grew highly-ordered islands, consisting of a few tunnel-coupled molecules, by a thermally activated diffusion process known as molecular self-assembly [13]. The islands were grown on a many monolayers thick NaCl film on a supporting Au(110) substrate, to suppress charge transfer between molecular islands and the metal substrate. We probe and manipulate the charge state of self-assembled molecular islands with single-electron control by means of AFM [14, 15]. From imaging and spectroscopy, we could gain insight into the distribution of excess electrons within an island. We found that the islands exhibit a probe-driven intra-island electron transfer in most charge states.
This allows us to directly observe and simulate the mutual interactions between individual charges and the stability of specific charge configurations within atomically-precise ordered molecular structures.
We find that the total number of excess electrons within a molecular island has a crucial influence on the stability of their distribution. Finally, we estimate the tunneling rates of the intra-island charge transfer from the experimental data.

A novel tentative mechanism of charge stabilization in a single molecule, based on strong polaronic shifts due to charge confinement.
In chapter 7, experiments on self-assembled PTCDA islands and individual PTCDA molecules on ultrathin NaCl films are presented. It was found that PTCDA molecules can be switched by applying voltage pulses. STM and AFM images suggest that this switching is related to charging, accompanied by structural changes. However, instead of occupying the lowest unoccupied molecular orbital, the experiments suggest that the excess charge could be localized at a molecule's functional group. There, it might be stabilized due to an exceptionally large energy gain, arising from strong spatial confinement of the excess electron.

2 Theoretical background

In this chapter, the imaging techniques and the underlying principles of scanning tunneling microscopy (STM) and atomic force microscopy (AFM) are introduced, which are commonly summarized under the term scanning probe microscopy (SPM). Further, a brief overview of specific imaging techniques will be given that were used in the experiments.

2.1 Scanning Tunneling Microscopy

In 1981 Binnig et al. reported on an experimental setup that enabled tunneling through a vacuum gap with precise control of the tunnel barrier width [16]. Shortly afterwards, they presented the first scanning tunneling microscope, which allowed to resolve conductive surfaces with atomic-scale resolution [1, 17].

Figure 2.1a shows the basic setup of an STM. It consists of an atomically sharp metal tip, whose position can be controlled with sub-angstrom accuracy in x-,y- and z-direction, and a flat conductive sample to be probed. If the tip is positioned sufficiently close (a few angstroms) to the sample surface and a bias voltage is applied, there is a finite probability for electron tunneling between tip and sample through the vacuum barrier, which gives rise to a measurable tunneling current. By recording this tunneling current while raster-scanning the sample, atomic-scale surface profiles can be obtained. This can be done in two different operational modes: in *constant-height mode* the tip is raster-scanned at a pre-defined plane above the sample surface. The obtained image contrast is then based on variations in the measured tunneling current.

Alternatively, as depicted, in *constant-current mode* the vertical position of the tip is adjusted by a feedback loop to keep the tunneling current at a predefined value.

The working principle of STM is based on the effect of quantum mechanical tunneling. In a one-dimensional picture of tunneling through a potential barrier, tip and sample can be considered as two metal electrodes separated by a potential barrier of height Φ and width $2a$, corresponding to the vacuum gap between tip and sample (see Fig.2.1b). For simplicity, it is assumed that the work functions Φ of tip and sample are identical. By applying a positive bias voltage to the sample with respect to the tip, the Fermi levels are shifted with respect to each other, such that in the sample unoccupied states become available for electrons below the Fermi level in the tip. In the following consideration it is assumed that the potential Φ is constant within

$-a < z < a$ (the latter is valid in the limit of small bias voltages $V << \Phi/e$). In a classical picture, an electron of energy $E < \Phi$, propagating in $+z$-direction, would simply be reflected at the barrier. In quantum mechanics, an electron is described by a wave function $\psi(r,t)$, and its probability density is given by $|\psi(r,t)|^2$ [18].

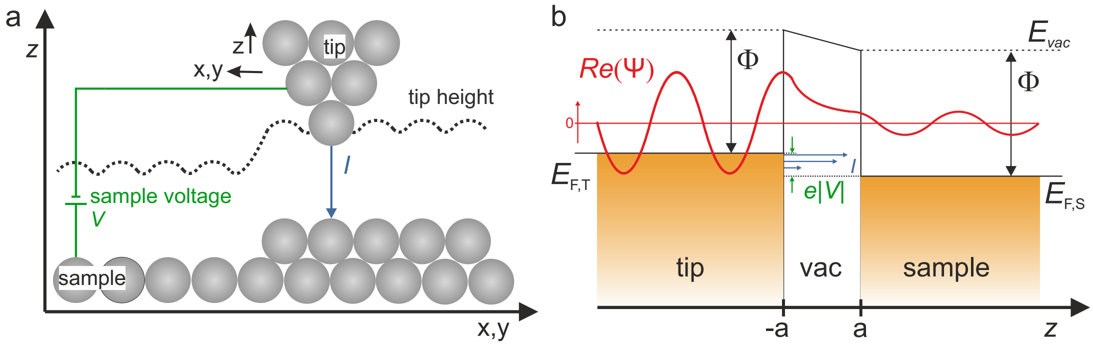

Figure 2.1: **a** The operation principle of an STM, using constant-current mode. **b** Schematic picture of quantum mechanical tunneling through a one-dimensional potential barrier. Tip and sample resemble the two electrodes separated by a potential barrier of height Φ. Further, the real part of an electron wave function of energy $E < \Phi$ is depicted, for propagation in $+z$-direction. after [19, 20]

To obtain the transmission probability for an electron of energy E through the barrier, the stationary Schrödinger equation has to be solved separately for the tip, sample, and vacuum region [18]. Outside the vacuum gap, where the electron can freely propagate, the solution is given by

$$\psi(z) = Ae^{ikz} + Be^{-ikz} \quad \text{for } z < -a \tag{2.1}$$

$$\psi(z) = Fe^{ikz} + Ge^{-ikz} \quad \text{for } a < z \tag{2.2}$$

with a wave number $k = \sqrt{2mE}/\hbar$. Within the vacuum gap the solution reads as

$$\psi(z) = Ce^{-\kappa z} + De^{\kappa x} \quad \text{for } -a < z < a \tag{2.3}$$

with a wave number $\kappa = \sqrt{2m(\Phi - E)}/\hbar$. The prefactors can be determined by using the boundary conditions at the sample/tip-vacuum interface z = +/-a. From this coefficients, one can approximate the transmission probability $|S(E)|^2 = |F|^2 / |A|^2$ through the barrier to [18]

$$|S(E)|^2 \approx e^{-2\sqrt{2m(\Phi - E)}\frac{2a}{\hbar}} \quad . \tag{2.4}$$

This consideration shows that the tunneling probability scales exponentially with the barrier width $2a$ (the vacuum gap) separating the two electrodes.
In the limit of $E << \Phi$, the decay constant may be expressed as $\kappa = \sqrt{2m\Phi}/\hbar$. For typical metal work functions of $\Phi \approx 5eV$ this yields a decay constant $\kappa \approx 10\,\mathrm{nm}^{-1}$ [20]. Hence, it becomes clear that the tunneling current is reduced by one order of magnitude if the vacuum gap is increased by 1 Å. If one considers that monoatomic step edges at metallic surfaces have a height on the order of 2 Å, this underlines the large sensitivity of STM to atomic-scale distance variations.

A more realistic treatment of the tunneling between two electrodes in three dimensions was developed by Bardeen [21] and applied to STM by Tersoff and Hamann for the case of an s-wave tip [22, 23]. They found that for small bias voltages, the tunneling current is proportional to the local density of states (LDOS) of the probed surface. Hence, images measured at constant current resemble a topographic map of constant LDOS at the surface [22, 23].
For a spherically symmetric tip, in the limit of small temperatures, and under the assumption that the tip density of states is constant within the range $(E_F - eV)$, it can be shown that the tunneling current at a finite bias voltage may be expressed as [20]

$$I \propto \int_0^{eV} \rho_s\left(E_F + \epsilon, \vec{r}_0\right) d\epsilon \quad , \tag{2.5}$$

where ρ_s denotes the local density of states of the sample and $\vec{r}_0$ is the position of the tip. Hence, the measured tunneling current is proportional to the surface LDOS integrated over the range of the applied bias voltage.

2.1.1 Scanning Tunneling Spectroscopy

Apart from the capability to image conductive surfaces with atomic resolution, STM can be used to probe the local electronic structure at a surface, which opened the door for the investigation of the electronic structure of single molecules [6, 24].

The derivative of the expression for the tunneling current from eq. 2.5 with respect to the voltage, reads [20]

$$\frac{dI}{dV}(V) \propto \rho_s\left(E_F + eV, \vec{r}_0\right) \quad . \tag{2.6}$$

From this, it becomes clear that the differential conductance is proportional to the LDOS of the sample. Hence, the energy-dependent density of states of single molecules can be probed by recoding the current vs. voltage characteristics and then taking the numerical derivative of the measured signal. Alternatively, as was done for all dI/dV measurements throughout this thesis, the dI/dV signal can be directly measured by lock-in detection. To this end, a small sinusoidal modulation voltage V_{mod} is added to the applied bias voltage, while the latter is swept within the range of interest.

2.1.2 Double barrier tunneling junction

As mentioned above, STS opens up the possibility to characterize the electronic structure of individual molecules and to resolve their frontier orbitals. However, molecules that are adsorbed on a metallic surface exhibit a large level broadening due to hybridization with the metal surface [6]. In 2005 Repp and coworkers showed that this electronic coupling to the supporting substrate can be avoided by using a few monolayers (ML) thin insulating NaCl separation layer [6]. Due to the large band gap of NaCl a strong hybridization of a molecule's frontier orbitals is prevented, whereas tunneling through such thin NaCl films occurs at rates that enable STM operation [6].

STM on such ultra-thin films can be described in the picture of a double barrier tunneling junction, as shown in Fig. 2.2. Here, tip and sample correspond to the two metal electrodes, and the vacuum gap and the NaCl layer correspond to the two tunneling barriers, separating the molecular levels from the two electrodes. $E_{F,T}$ and $E_{F,S}$ refer to the Fermi level of tip and sample, respectively. For simplicity, it is assumed that the work functions of the tip and the sample are identical. The molecular states are indicated as discrete levels, however, in practice these levels generally experience a broadening of $\approx 300\,\mathrm{meV}$ due to coupling of molecular states to phonon modes of the NaCl film [25].

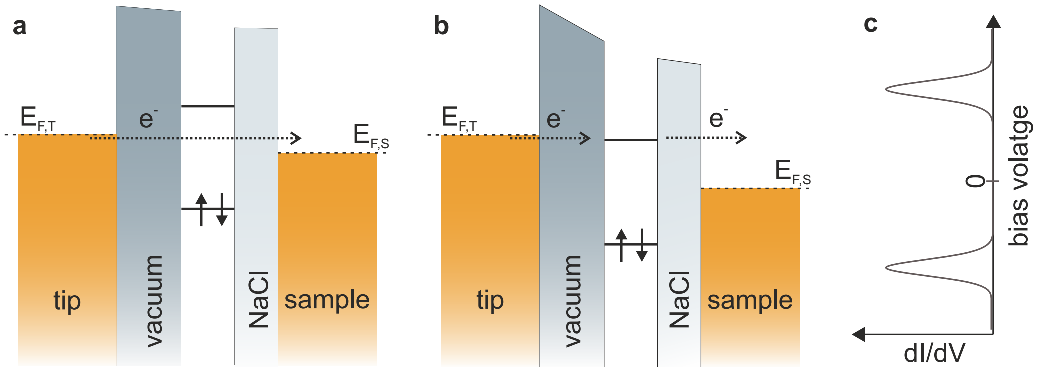

Figure 2.2: Tunneling through a double barrier tunneling junction. **a** Direct tunneling at small voltages (in gap). **b** Sequential tunneling through an unoccupied molecular state in resonance with the Fermi level of the tip. Electrons can tunnel from the tip into a molecular state, which is rapidly emptied via tunneling of the electron to the sample. **c** Idealized differential conductance curve.

By applying a positive bias voltage to the sample with respect to the tip, the Fermi levels are shifted relative to each other such that electrons from occupied states in the tip can tunnel into empty states at the surface. At a small bias voltage (Fig. 2.2a), no unoccupied states are available in the molecule, and electrons can only tunnel directly from the tip to the sample. If the bias voltage is large large enough that the Fermi level of the tip aligns with an unoccupied molecular state, electrons can resonantly tunnel from the tip to a molecular level to the sample (Fig. 2.2b). The additional possibility of resonant tunneling through a molecular level, gives rise to a peak in the conductance dI/dV at the corresponding voltage (Fig. 2.2c).
Similarly, at a sufficiently large negative sample voltage, tunneling from the sample via occupied molecular levels into free states in the tip can occur, also giving rise to a peak in differential conductance at negative bias voltage.

2.2 Atomic Force Microscopy

In 1986 Binnig, Quate, and Gerber introduced the atomic force microscope (AFM) [2]. Analogous to STM, an atomic-scale sharp tip is used to scan a surface. Instead of measuring tunneling currents, the working principle of AFM is based on the detection of the tiny forces that act between a tip, which is mounted to a flexible cantilever, and the sample surface. A force, acting between tip and sample, will cause a deflection of the cantilever. This force can be determined by measuring the cantilever deflection. Since AFM is based on measuring forces, it is not limited to conductive materials, thereby enabling the atomic-scale surface investigation of insulating materials.

An AFM can be operated in several different modes. The simplest one is the static mode, where the tip-sample force is directly determined from the static deflection of the cantilever. However, in static AFM the interacting forces between tip and sample can lead to a jump-to-contact, which occurs because of the requirement to use very soft cantilevers in order to measure tiny forces [26, 27].
For non-destructive measurements with ultimate resolution, it is required to operate in a dynamic mode, where the cantilever is externally driven to oscillate at or close to its resonance frequency. In general, there are two methods for dynamic operation, namely, amplitude-modulation (AM) and frequency-modulation (FM) mode [26]. Throughout this thesis, we exclusively used FM-AFM. Hence, only this operational mode will be discussed in the following. FM-AFM was first proposed by Albrecht et al. [29] and its operating principle is shown Figure 2.3a.
In this mode, the cantilever is driven to oscillate at its resonance frequency f_0, and when being brought close to a surface, the interaction with the surface causes a measurable frequency shift Δf. For this operational mode, several external circuits are necessary which will be described in the following. The deflection of the cantilever is recorded and amplified. A phase-locked loop detects the frequency shift with respect to the resonance frequency f_0 of the unperturbed cantilever. Additionally, an automatic gain control is used to keep the cantilever oscillating at a constant oscillation

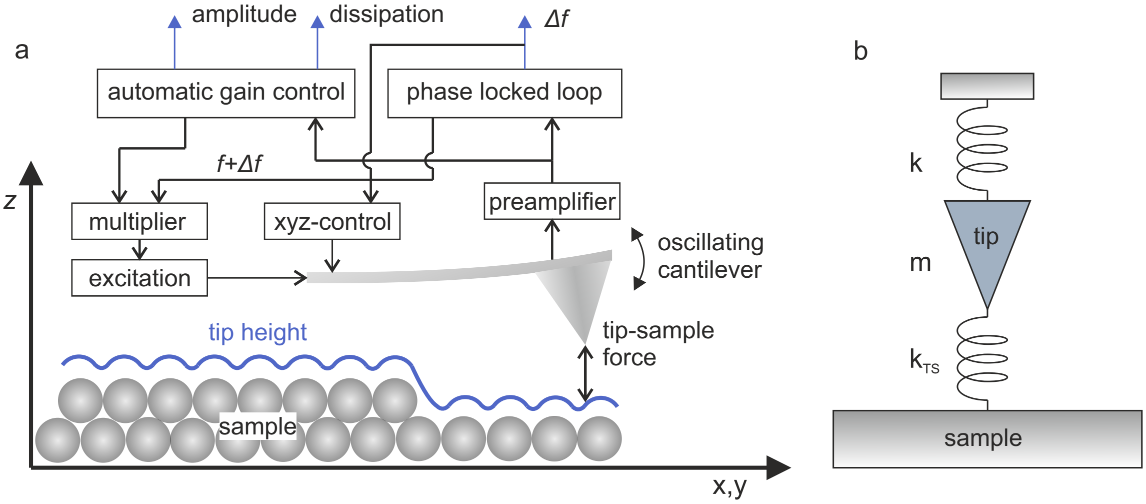

Figure 2.3: **a** Schematic picture of the operation principle of an AFM in frequency modulation mode. **b** Mass and spring model of cantilever and tip-sample forces. After [28].

amplitude. To this end, the output signal of the automatic gain control and the resonance frequency $f+\Delta f$ are multiplied, and applied as an excitation signal to the cantilever [28, 29]. Analogous to STM, there are two common operational modes. In *constant-height* mode the tip is scanned in a plane parallel to the sample surface, to map the local frequency shift variations.
Alternatively, the AFM can be operated in *constant-Δf mode*, where the tip-sample distance is adjusted by an additional feedback loop to maintain a cantilever oscillation at constant amplitude at a predefined Δf set point.

In the following, it will be derived how the frequency shift relates to the forces that act between tip and sample according to reference [28]. As illustrated in Fig 2.3b, the oscillating cantilever can be considered as a mass m^* attached to a spring with an effective stiffness k and hence its unperturbed resonance frequency f_0 is given by

$$f_0 = \frac{1}{2\pi}\sqrt{\frac{k}{m^*}} \quad . \tag{2.7}$$

The force F_{ts} arising from the tip-sample interaction potential U_{ts} can be considered as an additional spring of stiffness k_{ts} attached to the tip,

$$F_{ts} = -k_{ts} z \quad , \tag{2.8}$$

where $k_{ts} = -\frac{\partial F_{ts}}{\partial z}$ is the effective spring constant, and z the tip-sample distance. This approximation is only valid in the limit of small cantilever oscillation amplitudes, for which k_{ts} can be assumed as constant within the range of the cantilever oscillation (for the experiments, shown in this thesis, the oscillation amplitude was $\leq 2\,\text{Å}$). Under this assumption, the resonance frequency of the perturbed cantilever may be expressed as

$$f = \frac{1}{2\pi}\sqrt{\frac{k + k_{ts}}{m}} \quad . \tag{2.9}$$

If it is further assumed that $k >> k_{ts}$, f can be written as

$$f = f_0\left(1 + \frac{k_{ts}}{2k}\right) \quad . \tag{2.10}$$

This is justified since our AFM cantilevers have stiffnesses of $k = 1800\,\text{N/m}$[28], while tip-sample stiffnesses are typically below $10\,\text{N/m}$. Hence, the frequency shift Δf can be given as

$$\Delta f = f - f_0 \approx f_0\frac{k_{ts}}{2k_0} = -\frac{f_0}{2k_0}\frac{\partial F_{ts}}{\partial z} = \frac{f_0}{2k_0}\frac{\partial U_{ts}^2}{\partial z^2} \quad . \tag{2.11}$$

Equation 2.11 shows that the measured frequency shift is proportional to the gradient of the force that acts between tip and sample and hence proportional to the second derivative of the tip-sample interaction potential U_{ts}.

In general, there are several types of forces, with different decay lengths that can act between the tip and a surface [28]. For resolving the structure of individual molecules, the relevant forces are the rather long-range attractive van der Waals forces and short range Pauli repulsion [9]. The interaction potential corresponding to these force contributions is often empirically modeled with a Lennard-Jones potential [28, 30]. Further, electrostatic forces play a crucial role for detecting charge states of atoms or molecules and charging events by means of AFM [11, 31]. Thus, their role will be discussed in more detail in the next section.

2.2.1 Kelvin probe force spectroscopy

Kelvin probe force spectroscopy (KPFS) is a method by which local variations of the sample work function can be detected. It is related to the Kelvin Probe method, which was first reported by Lord Kelvin in 1898 [32]. In this technique, two metals plates of different materials, which are in electrical contact, are being brought close. If the distance between these plates is modulated at a frequency ω the capacitance periodically changes, causing an alternating current between the two plates. The resulting current is minimized if an additional bias voltage is applied between the two plates that equals the contact potential difference of the two metal plates [33]. This can be rationalized in the following picture, where the tip and sample are considered as the two metal electrodes with distinct work functions Φ_T, Φ_S, as shown in Fig. 2.4. For the electrodes being not in electric contact, the difference between their Fermi levels is given by their difference in work functions $\Delta\Phi = \Phi_\text{T} - \Phi_\text{S}$ (Fig. 2.4a). Upon electric contact formation, charge carriers will flow from the electrode with the

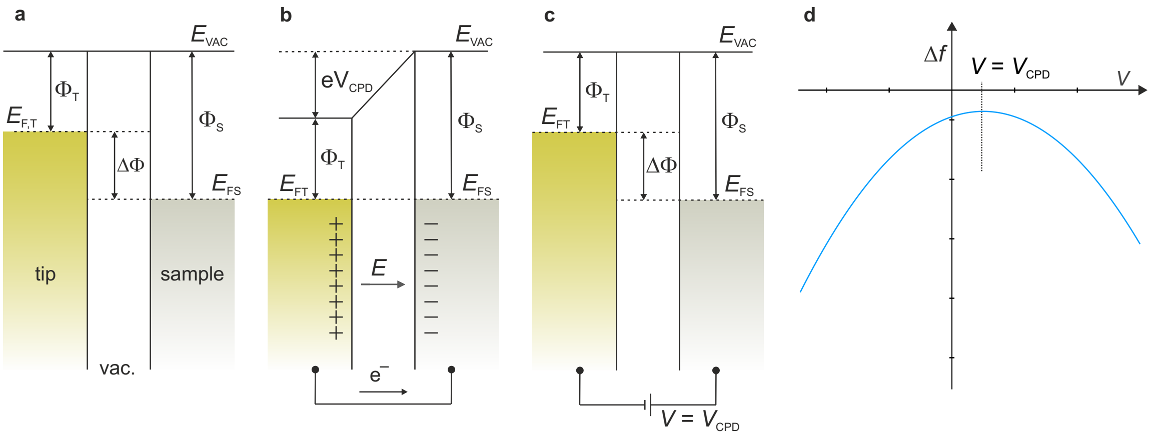

Figure 2.4: Principle of KPFS. **a** Tip and sample before electric contact formation. **b** Tip and sample in electric contact. Surface charges accumulate upon alignment of the Fermi levels, which gives rise to an electrostatic force. **c** A voltage V_{CPD} is applied to compensate for this electrostatic force. **d** Schematic $\Delta f(V)$ curve. The electrostatic force contribution becomes minimal at $V = V_{CPD}$. Figure after [34].

lower work function to the one with the larger work function until their Fermi levels align (Fig. 2.4b). This gives rise to an electrostatic potential commonly referred to as contact potential difference $V_{CPD} = \Delta\Phi/e$ and hence to an electrostatic force between the electrodes. This contact potential difference and the resulting electrostatic force can be compensated by applying a bias voltage $V = V_{CPD}$ between the electrodes (Fig. 2.4c). Hence, for the case of the Kelvin Probe method, the current will go to zero if the contact potential is compensated.

Instead, KPFS relies on the sensitivity of AFM to electrostatic forces. In the following, it will be briefly explained how the electrostatic force and the resulting frequency shift depend on the applied voltage. If the curvature of the tip is neglected, tip and sample can be described as a plate capacitor, with tip and sample as the two plates [33]. If one takes into account the contact potential difference between tip and sample, the energy U_{el} stored in the capacitor is given by

$$U_{el} = \frac{1}{2}C(z)\left(V - V_{CPD}\right)^2 \ , \tag{2.12}$$

where z denotes the tip-sample distance, C the tip-sample capacitance and V the applied bias voltage. According to eq. 2.11 the dependence of the frequency shift, arising from electrostatic forces, on the applied bias voltage reads as

$$\Delta f_{el} \propto \frac{\partial F_{el}}{\partial z} \propto \frac{\partial U_{el}^2}{\partial z^2} \propto \frac{1}{2}\frac{\partial C^2}{\partial z^2}\left(V - V_{CPD}\right)^2 \ . \tag{2.13}$$

From this relation, one can see that the frequency shift has a square dependence of the applied bias voltage. Hence, the electrostatic contribution to the measured frequency shift becomes minimal, when the applied sample voltage equals the V_{CPD}. In KPFS, the frequency shift Δf is recorded as a function of the applied bias voltage, which is schematically shown Figure 2.4d. The horizontal shift of the minimum of the parabolic curve gives the contact potential difference between tip and sample.

Nonnenmacher and colleagues first applied the principle of minimizing the electrostatic forces to AFM, when they proposed the method of Kelvin Probe Force Microscopy [35]. This method allowed them to detect local work function differences while at the same time recording topographic images of a surface by means of AFM with a spatial resolution below 50 nm.
This opended the door to the distinction of different charge states of atoms and molecules [11, 12, 14, 15, 36] and even to the detection of subtle work function variations caused by a non-homogeneous distribution of charges within single molecules by means of KPFS [37–39].
Since AFM measures contact potential differences with high spatial resolution, the voltage needed to compensate the contact potential difference (V_{CPD}) is often referred to as local contact potential difference (LCPD).

2.2.2 Dissipation

Dissipative forces will be important for the interpretation of the results presented in chapter 6. Therefore, a brief introduction into their role in FM-AFM will be given and what physical origins can potentially give rise to dissipation in experiments.

A freely oscillating cantilever can be described as a weakly damped harmonic oscillator, and hence its energy loss per oscillation cycle $\Delta E_{cantilever}$ is given by

$$\Delta E_{cantilever} = 2\pi \frac{E}{Q}, \quad \text{with} \quad E = k\frac{A^2}{2}, \tag{2.14}$$

where E is the energy stored in a cantilever oscillating at an amplitude A, k its stiffness and Q the quality factor [26, 28]. When the AFM tip is brought close to a surface, tip-sample forces arise. In FM-AFM, conservative forces lead to a change in the resonance frequency, whereas non-conservative forces cause dissipation [26, 40]. If the tip-sample forces occurring during image acquisition are conservative, the tip-sample force will result only in a frequency shift of the cantilever. Since this intrinsic dissipation of the cantilever depends on fixed parameters, it will not lead to any spatial signatures in AFM measurements, irrespective of local tip-sample force variations.
However, a non-conservative tip-sample force can lead to an additional energy change ΔE_{ts} per cycle [26].
Such a non-conservative tip-sample interaction is schematically shown in Fig. 2.5. Variations of the force, for example, arising from charging a single molecule [36],

can give rise to abrupt shifts in a measured $F(z)$ curve. Under the condition that charging and discharging occur at different cantilever positions, this will open up a hysteresis in the probed $F(z)$ signal and hence give rise to an increase or decrease in dissipation, depending on the direction of the force shifts.
Hence, ΔE_{ts} per cycle is given by the integral of the tip-sample force F_{ts} along the cantilever pathway within one oscillation cycle [26]

$$\Delta E_{ts} = \oint F_{ts}(z + q')dq'. \tag{2.15}$$

This additional contribution will affect the measured dissipation. In general, such dissipative forces can be of different origins. For example, Lotze et al. found that molecular hydrogen trapped between tip and surface can drive an AFM cantilever by inducing motions of the molecular hydrogen via inelastic electron tunneling [41]. Further, such non-conservative forces can arise from variations of the electrostatic force during a cantilever oscillation cycle. This was exploited in the group of Grutter, for example, to map single-electron charging events of quantum dots [42–44]. Ondráček, Hapala and Jelínek, simulated how such perodic charge modulations affect the cantilever dynamics [45]. Further, Steurer and colleagues examined the relation between tunneling rate and dissipation for the sequential tunneling through vacancy states in

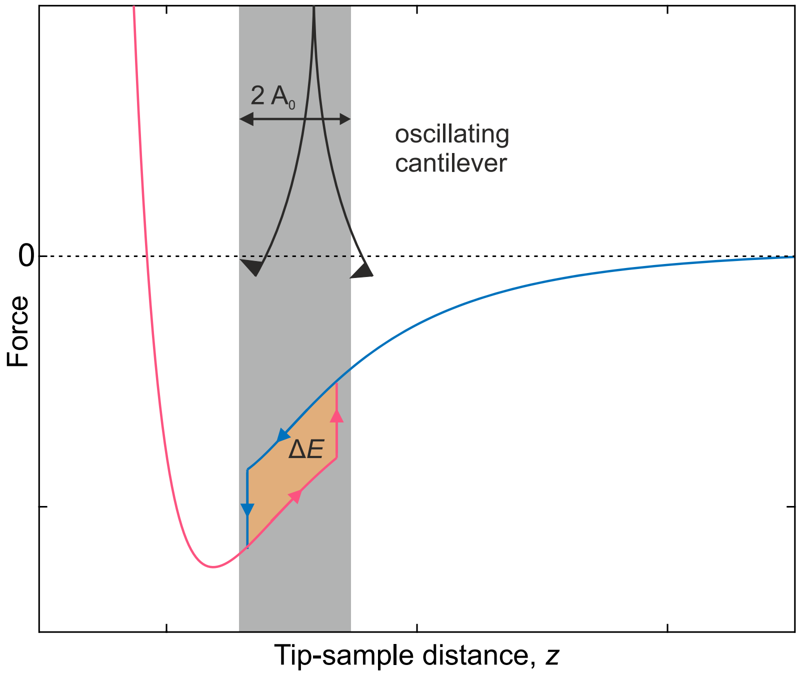

Figure 2.5: Cantilever dissipation due to non-conservative forces. The vertical range of cantilever motion is defined by the cantilever oscillation amplitude (width of grey shaded area). The orange area corresponds to the dissipated energy. Arrows indicate trajectory of the force curve.

NaCl [46]. Recently, we made use of dissipative forces to image molecular orbitals on insulators [36].

In our experimental setup, the dissipated energy is not directly measured, instead the excitation signal A is recorded that is needed to keep the cantilever oscillate at a constant amplitude. However, it can be derived that the microscopic dissipation can be quantified by relating the measured excitation signal A to the excitation of the unperturbed cantilever A_0, using [26, 28]

$$\Delta E_{ts} = 2\pi \frac{E}{Q} \left(\frac{A - A_0}{A_0} \right). \tag{2.16}$$

2.3 Charge transfer processes in SPM

Since charge transfer processes play a central role in all the experiments presented in this thesis, a brief literature overview of charge state manipulation and detection by means of SPM will be given. Further, the concept of Marcus reorganization energy [47], which is an important mechanism for charge stabilization, will be briefly explained.

In 2004 Repp and colleagues investigated individual Au atoms adsorbed on an ultrathin decoupling NaCl layer, grown on a Cu(111) substrate, by means of STM [7]. They found that the charge state of Au atoms can be switched by applying voltage pulses and, moreover, that the atoms exhibit charge bistability, which means that an atom can stably exist, either, in its neutral or singly negative charge state within a certain range of the applied bias voltage [7]. Shortly after, such bistability was also observed for single molecules by Wu et al. [48, 49], Leoni et al. [50], and Swart et al. [8]. Further, it was found by Olsson and colleagues [51] and Steurer and colleagues [31] that atoms can be stable in three different charges states on thin NaCl films.

Since the early 1990s several pioneering studies have appeared that demonstrated the capability of AFM to measure charge state transitions with single electron sensitivity [52–56]. In 2009 Gross et al. demonstrated that AFM can even resolve different charge states of individual Au atoms, adsorbed on ultrathin insulating films by means of KPFS [11].

As discussed in section 2.2.1, the measured Δf signal has a square dependence of the applied bias voltage. Upon charging, the electrostatic contribution to the force will change. Furthermore, the additional charge will affect the local work function and hence distinct charge states are assigned to distinct parabolic $\Delta f(V)$ curves [11]. Such parabolic curves are schematically shown in Fig. 2.6a for two distinct charge states as dashed red and blue curves. The horizontal shift of the parabolas is related to the change of the LCPD due to the additional charge. However, the vertical shift is in many cases difficult to interpret and can not straightforwardly be assigned to a difference in electrostatic forces [31]. For example, vertical relaxations of the probed atom or molecule upon charging can also account for a vertical shift of a $\Delta f(V)$ curve. In AFM measurements, such charge state transitions appear as distinct steps in $\Delta f(V)$ due to the fact that each charge state is assigned to a distinct parabolic curve [11, 31]. Such a charging spectra is schematically depicted as a solid black curve in Fig. 2.6a, with a hysteresis due to charge bistability.

The aforementioned studies on charging single adsorbates were predominantly carried out for adsorbates on thin insulating films [7, 8, 31, 48–51], where the tunnel coupling to the conductive substrate is very large and hence a transiently occupied state would in most cases be immediately emptied. However, if the electron affinity of an adsorbate is close to the Fermi level of the substrate, a transiently occupied state can shift across the Fermi level of the substrate, and hence be stabilized, due geometrical relaxations of the adsorbate and the NaCl film as a response to the additional charge in the adsorbate [7, 8, 51]. This energy gain upon relaxations of the molecular geometry and its environment is commonly known as Marcus reorganization energy [47, 57–60].
Beyond experiments on ultrathin films, where charge bistability is only possible with certain restrictions, AFM enabled to investigate charge state transitions for molecules adsorbed on insulating substrates, where tunneling is only possible between tip and molecule [14, 15, 60].

Following reference [60], the concept of reorganization energy for a single molecule can be explained in a Franck-Condon picture. As shown in Fig. 2.6b, each charge state is attributed to a distinct potential energy curve with corresponding vibrational states. The horizontal axis refers to the generalized coordinate, which takes into account the geometric structure of the molecule and its environment. The underlying idea of the Franck-Condon principle is that electronic transitions occur fast compared to the timescales of nuclear motions, for which reason only vertical transitions are allowed [61]. This picture is often used in the context of optical spectroscopy, where these vertical transitions correspond to the absorption and emission of photons. There, both curves represent electronic states with the same number of electrons.
In contrast, here, transitions require an electron exchange with the tip. Therefore, the free energies of the two charge states have to be considered with respect to electron exchange with the tip and thereby the free energy curves are shifted vertically with respect to each other by the applied bias voltage.
At the voltage V_{deg} that corresponds to the degeneracy of the neutral and anionic vibrational ground states, a charge transfer is very unlikely due to the weak spatial overlap of the vibrational wave functions (wave functions of the nuclear coordinates - see Fig. 2.6c). If the bias voltage is increased further ($V = V_{red}$, Fig. 2.6d), the vibrational ground state of the neutral molecule energetically aligns with an vibrationally excited anionic state, whose vibrational wave function has a significant spatial overlap with the vibrational wave function of the neutral molecule, and hence a charge state transition can occur with significant probability. Once being charged, the molecule-substrate system relaxes into the anionic vibrational ground state. The resulting energy gain is called relaxation energy λ_{red} [60].

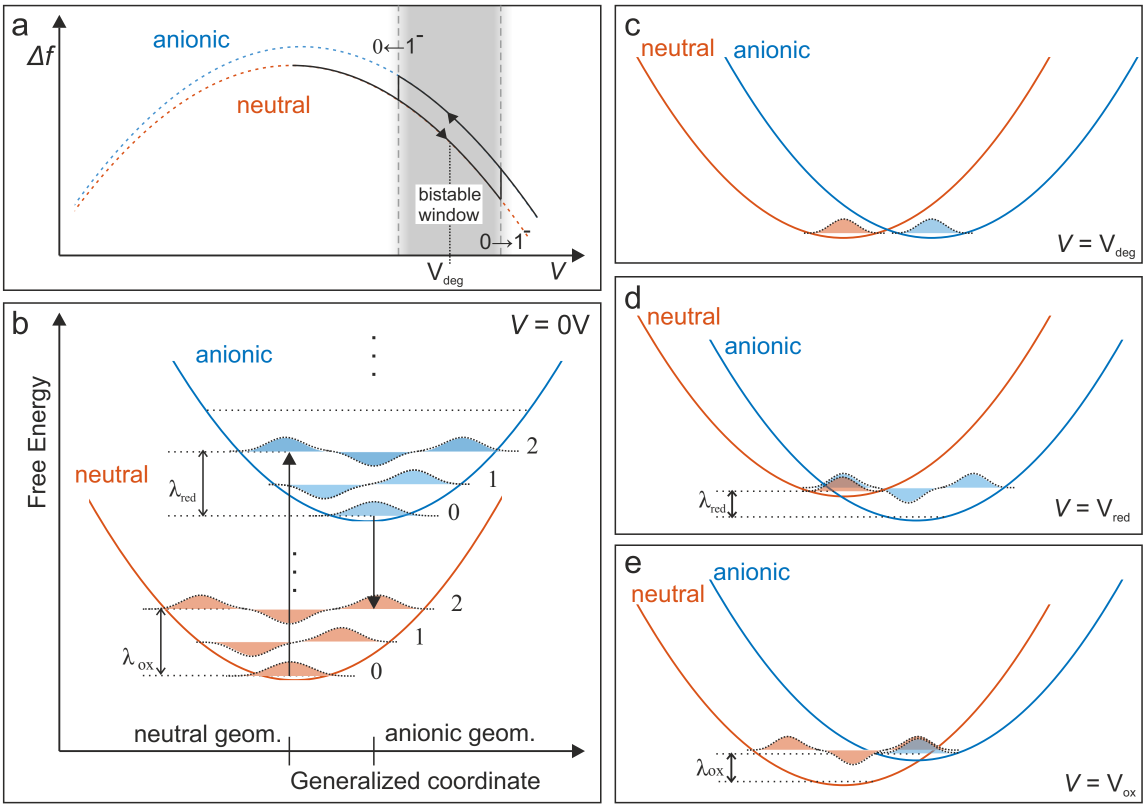

Figure 2.6: **a** Schematic picture of an electron transfer processes as observed in AFM $\Delta f(V)$ spectroscopy experiments. The solid curve indicates a Δf spectrum and dashed curves correspond to the parabolic Δf curves of two distinct charge states. **b-e** Electron transfer in a Franck-Condon Picture. **b** Free energy curves of a molecule in the neutral an anionic state and the corresponding vibrational modes, without applied bias voltage. **c** Both charge states are brought to degeneracy by an applied bias voltage V_{deg}. **d** Reduction occurs if a transition between the neutral vibrational ground state and an vibrational state of the anionic molecule, with significant spatial overlap, becomes energetically allowed ($V = V_{red}$). **e** Similarly, at $V = V_{ox}$ oxidation takes places if the anionic vibrational ground state energetically aligns with an excited neutral state with significant vibrational wave function overlap. The figure was adapted from [60].

Fully analogous, the discharging can only occur with significant probability if the anionic vibrational ground state energy intersects with a neutral state with a large overlap of the respective vibrational wave functions, being accompanied by a relaxation energy λ_{ox} ($V = V_{ox}$, Fig. 2.6e). The reorganization energy is defined as $E_{reorg} = \lambda_{ox} + \lambda_{red}$ and is responsible for the hysteretic nature of the charge transfer in single molecules [60]. For adsorbates on NaCl, this reorganization energy was reported to be in the order of 1 eV [7, 60].

In experiments, however, we observe that the hysteresis can be much narrower than one would expect from those values. Furthermore, the width of the observed hysteresis reduces with reduced tip-sample distance and ultimately collapses. The reason behind this is that the strength of the tunnel coupling to the conductive electrodes is not taken into account in the above model. If this tunnel coupling becomes large, charge transitions can even occur at $V = V_{deg}$. Further taking into account that all the levels exhibit a broadening of $\approx 300\,\mathrm{meV}$ [25], it becomes clear that the transitions voltages V_{ox} and V_{red} are not discrete values but underlie a certain stochasticity, for which reason the transitions of the bistable window are indicated as blurred in Fig. 2.6a. Hence, the observed hysteresis width must not be directly interpreted as a measure for the reorganization energy, but rather reflects the product of tunnel coupling and reorganization energy.

2.4 Alternate-charging scanning tunneling microscopy

The use of insulating films as a decoupling layer [6] has become indispensable for the investigation of the electronic structure of individual molecules in scanning probe microscopy. Especially AFM allowed to gain fascinating insights into electron transfer processes at the single-molecule scale [12, 14, 31, 60]. To access such out of equilibrium charge states, in most cases, a thick insulating NaCl film is required to suppress charge transfer to the conductive substrate. Thereby, the characterization of the electronic structure by means of STM is inhibited.
Recently, we developed a novel imaging technique that enables the mapping of molecular orbitals on insulators with atomic-scale resolution, which is called alternate-charging scanning tunneling microscopy (AC-STM) [36, 62–64].

Figure 2.7 shows the working principle of this technique. The d.c. bias voltage $V_{\mathrm{d.c.}}$ is chosen to lie within the bistable window of a certain charge state transition of a molecule to be investigated (compare Fig. 2.6a). By applying suitable voltage pulses of opposite polarity (*Set* and *Reset*, $t \approx 100\,\mathrm{ns}$), synchronized with the AFM cantilever oscillation, the charge state is periodically switched. Importantly, the phase of the pulses with respect to the cantilever motion is chosen such that the *Set* pulse occurs at the upper and the *Reset* pulse at the lower turnaround point of the cantilever. This results in different electrostatic forces acting on the cantilever during up- and downward movement and, hence, causes a measurable dissipation of the cantilever motion [36].
The key to spatial resolution is the exponential nature of tunneling. Given an amplitude of $A = 1\,\text{Å}$ the tunneling probability at the upper turnaround point is reduced by a factor of ≈ 100. In experiments, the tip height is chosen such that the efficiency of switching the charge state of the molecule with the *Reset* pulse is one irrespective of the spatial tip position above the molecule. In contrast, the efficiency of switching the charge state with the *Set* pulse is strongly reduced since it occurs at significantly larger tip height. Hence, the *Set* pulse becomes sensitive to the spatial orbital density,

and thereby enables to obtain images of the latter based on the spatial modulation of tunneling probability.
For a detailed description of the experimental technique and its applications, it is referred to [36, 62, 64].

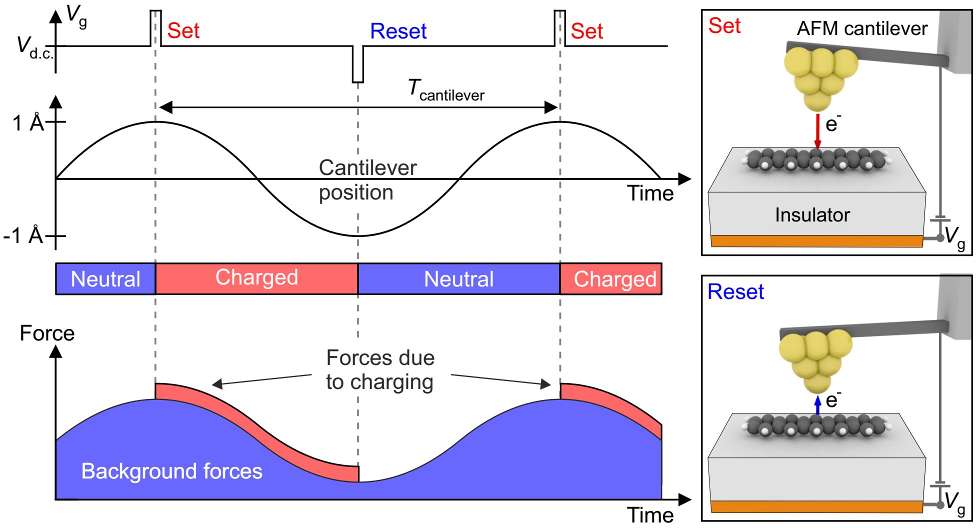

Figure 2.7: Working principle of AC-STM. Pulses of opposite polarity (*Set*, *Reset*) are used to charge and discharge a molecule, synchronized with the oscillatory motion of the cantilever. This causes periodic changes of the measured force thereby leading to an increase in dissipation. The schematic pictures indicate the direction of electron transfer corresponding to the *Set* and *Reset* pulses. The figure was adapted from [36].

2.5 AFM with functionalized tips

In 2009 Gross et al. demonstrated that AFM can be used to resolve the chemical structures of single molecules [9]. To this end, a single carbon monoxide (CO) molecule was transferred to apex of the tip. When imaging individual molecules with such a CO-functionalized tip, sharp lines appear in the AFM image contrast that resemble the chemical structure of the probed molecule. This technique has become a powerful tool for resolving the chemical structure of individual molecules at the atomic scale and enabled characterizing of on-surface reactions [65–71] adsorption geometries [72, 73], and even distinguishing bond orders within a single molecule [10, 12].
It was found that the observed intramolecular contrast in such images originates from Pauli repulsion, arising from the overlap of electron densities of the CO molecule at the tip and the probed molecule at the surface at very small tip-sample distances [9, 30]. Van-der-Waals (vdW) forces, instead, only lead to a featureless attractive background signal, due to their long-range nature [9, 30]. Further, Hapala et al. found that the low lateral stiffness of the CO molecule at the tip leads to

an additional contrast sharpening and the observation of sharp ridges in the image contrast that have a close resemblance to chemical structure drawings [74]. However, those sharp ridges can not always be simply interpreted as actual bonds. Instead, they could also result from the specific interaction potential landscape, as shown in studies by Pavliček et al. and Hämäläinen et al. [75, 76]. The fact that the CO molecule easily bends at the tip due to the tip-sample interactions can give rise to strong distortions of the apparent molecular structure in AFM images [74, 76, 77]. Apart from CO, several other tip functionalizations have been reported to be useful for specific aspects of AFM. For example, Mönig et al. found that an oxygenated copper tip enables much less distorted imaging of individual molecules [78]. Further, Br-terminated tips were reported to be useful for lateral manipulation of molecules on an insulating surface, and Xenon tips were recommended for KPFS measurements by Mohn and colleagues [79].

3 Experimental setup and methods

In this chapter the experimental setup will be introduced. Further, a general description of the sample preparation will be given.

3.1 Experimental setup

All the experiments were conducted in a home-built low-temperature combined STM and AFM based on the design of Meyer [80], which is shown in Figure 3.1.[1] The chamber consists of three separable units: sample holder and molecule evaporators are introduced into the UHV chamber via the load-lock. This chamber is pumped with a diaphragm pump and a turbomolecular pump, which enables pressures down to $\approx 1 \times 10^{-9}$ mbar. The preparation chamber contains the instruments for sample preparation, which are sputter gun, leak-valve for sputtering gas, salt evaporators, and a quartz crystal microbalance for deposition rate detection. Also, a Ti sublimation pump and an ion pump are installed at the preparation chamber, which enable a base pressure of $< 10^{-10}$ mbar. Further, the chamber is equipped with a manipulator to move samples and evaporators, and to transfer samples into the STM. The STM scan head is mounted at the bottom of a liquid-He bath cryostat, which allows operational temperatures of $T < 10\,\mathrm{K}$.

3.1.1 The scan unit

Figure 3.2 shows the scanner, which is suspended from the bottom of the bath cryostat by three springs to provide mechanical decoupling. In combination with three magnets at the bottom of the STM head, those springs serve as an eddy current damping in order to reduce mechanical noise. For further noise reduction, the ground below the entire chamber is decoupled from the foundation of the building.

The STM/AFM preamplifiers are directly mounted to the scan unit. In our setup the bias is applied to the sample with respect to the tip, which is on virtual ground. The STM/AFM sensor is mounted at the bottom of the ramp ring in a Besocke design [81]. In this design, the STM/AFM sensor is mounted in the center of a ring-like

---

[1] The are two equivalent home-built microscopes in our labs. A part of the measurements was done with the setup shown here, and the rest was carried out with the other one.

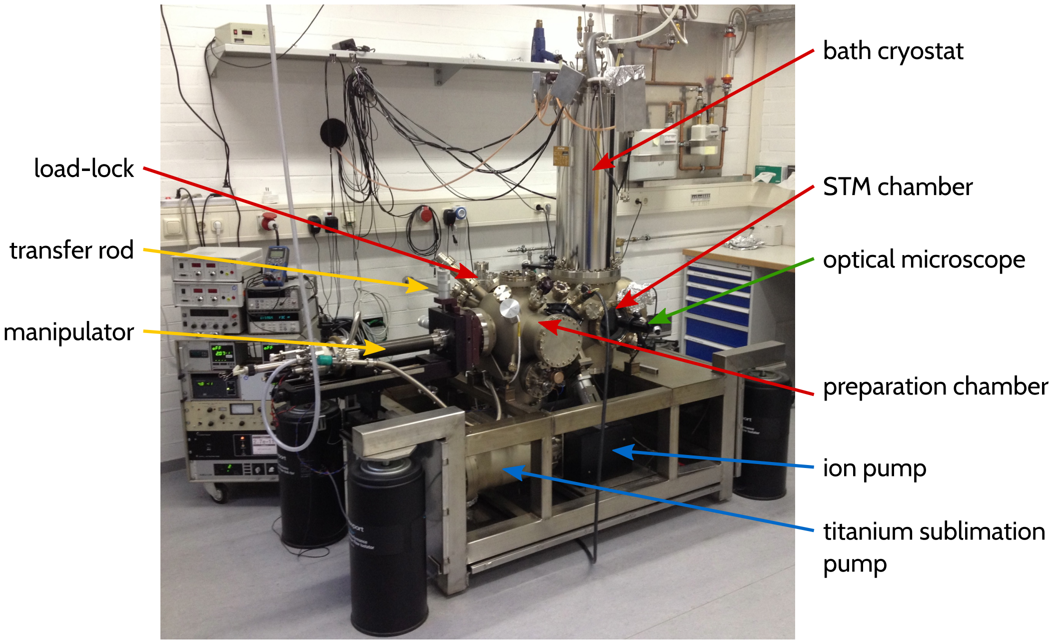

Figure 3.1: Image of a combined, low-temperature, ultra-high-vacuum STM and AFM, with bath cryostat. The image was kindly provided by N. Pavliček [82].

copper device (ramp ring), which consists of three separate inclined segments. This device lies atop of three piezo tubes. For vertical coarse approach, specific voltage pulses are applied to the piezo tubes, resulting in a slip-stick rotation of the ring. Due to the inclination of the ring segments, this rotational motion results in a vertical motion of the tip. These piezo tubes also serve as x-, y-, and z-position control. The AFM cantilever is excited to oscillate with a piezo plate on which the sensor is mounted to the center of the ramp ring (not visible here).

3.1.2 qPlus sensor

Our microscopes are operated with a qPlus sensor, which was introduced by Giessibl in 1998 and has become one of the most commonly used types of force sensors in high-resolution AFM [83, 84]. This type of sensor has several advantages. It has a much higher stiffness on the order of 10^3 N/m compared to other commonly used cantilever materials like silicon ($10^1 - 10^2$ N/m [29, 85]). The high stiffness allows stable operation at very low amplitudes ($A < 1$ Å) with an appreciable signal-to-noise ratio and without the risk of a jump-to contact [28, 84]. Furthermore, AFM operation at low cantilever amplitudes increases the sensitivity to short-range forces compared to long-range forces and hence can increase the spatial resolution [84]. Since quartz is a piezoelectric material the motion of the oscillating tuning fork can be directly detected [84]. Figure 3.3 shows a qPlus sensor with the electrodes for

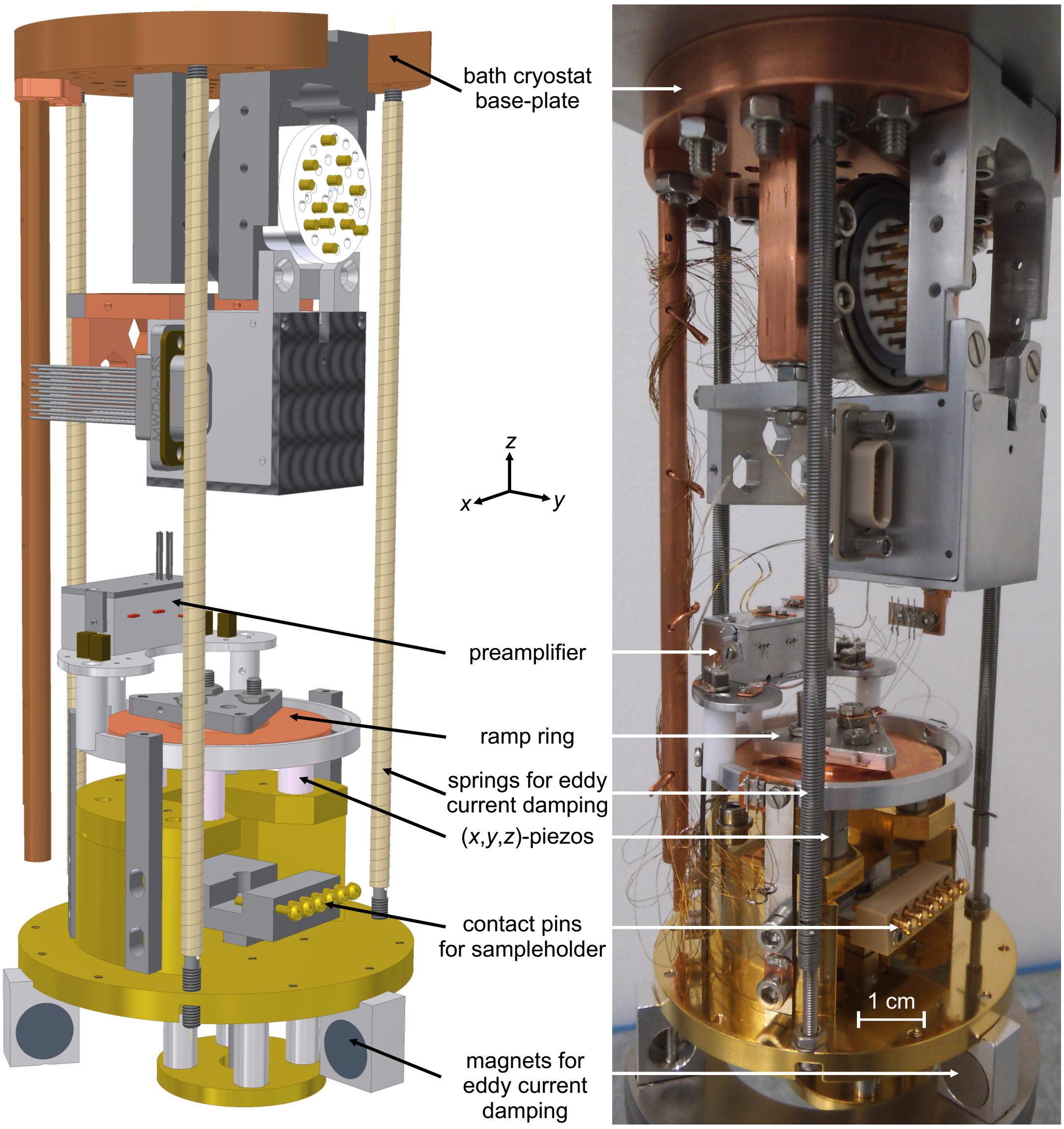

Figure 3.2: Drawing and photograph of the combined STM/AFM scan unit, being mounted to the bottom of the bath cryostat. The image was kindly provided by G. Münnich [19].

tunneling current and deflection detection and a cut PtIr tip glued to the end of the prong. This sensor has an asymmetric design (type S1.0 in ref. [26]), with the same dimension of the free prong as a conventional qPlus sensor. This sensor type was used for most of the measurements. Some measurements in chapters 6 and 7 were carried out with a standard qPlus sensor similar to ref. [84].

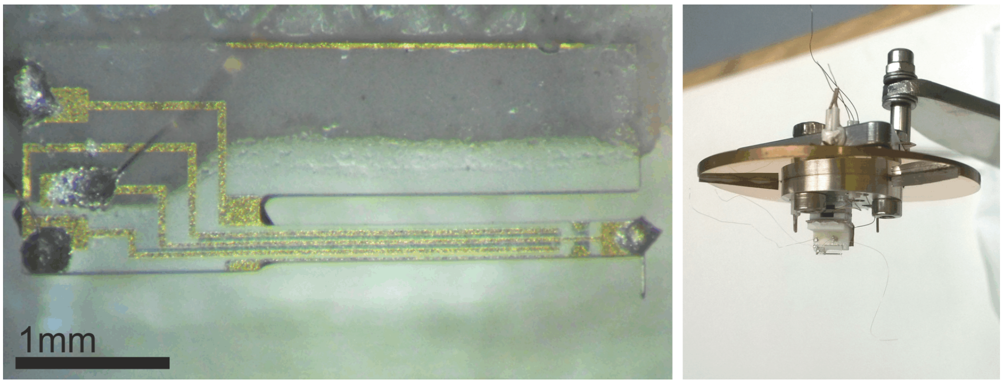

Figure 3.3: Images of a qPlus-based STM/AFM sensor in different build-up stages. **Left:** qPlus sensor with a tip (cut PtIr wire, diameter 25 μm) glued to the prong and electrical connections for deflection detection and tunneling current. **Right:** Image of the qPlus sensor mounted to the ramp ring giving view to one of the inclined ramp planes.

3.2 Sample preparation

For the projects throughout this thesis, either Cu(100) or Au(110) surfaces were used as substrates. In order to obtain clean, flat surfaces for the measurements, a series of sputtering and annealing cycles was performed. We used neon as a sputtering gas, which was dosed into the preparation chamber up to a partial pressure $p \approx 5 \times 10^{-5}$ mbar. The sputter gun is operated at an emission current of 20 mA and a beam energy of 1 keV. After each sputter cycle (≈ 30 minutes), the sample is annealed at $T = 550\,°\mathrm{C}$ using a button heater, on which the sample is mounted to the sample holder. During the last annealing cycle the sample is heated to $T = 500\,°\mathrm{C}$. This is followed by the deposition of NaCl, which is thermally evaporated from a tantalum crucible. The NaCl deposition rate is measured with a calibrated quartz crystal microbalance. This is oscillated at its resonance frequency, which is lowered due to the amount of deposited NaCl. The sample temperature was held at 5 °C during NaCl deposition in the experiments with the Cu(100) samples, whereas for Au(110), the temperature was held at 160 °C.

Finally, the sample is cooled down ≈ 80 K with the liquid-nitrogen cooled manipulator and inserted into the < 10 K cold STM. All molecules were sublimed in-situ onto the cold sample being inside the STM chamber. To this end, we used a molecule

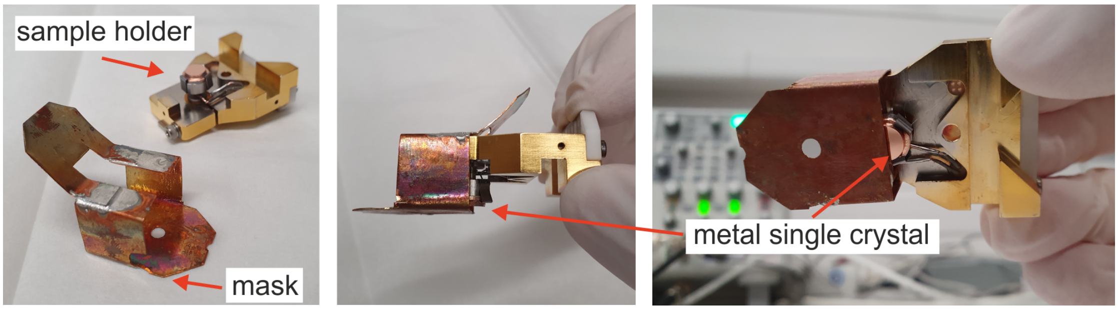

Figure 3.4: **Left:** image of the mask and a sample holder. **Middle**: side view on a sample holder with the mask, **Right**: top view onto the screened sample holder.

evaporator that is loaded with molecules under ambient conditions and then introduced into the UHV chamber.
CO molecules for tip functionalization [9] were dosed onto the cold sample by exposing the chamber to CO gas at a partial pressure of 2×10^{-7} mbar while opening the shutter to the STM for ≈ 5 s.

The experiments shown in chapters 5-7 require NaCl coverages of > 2 monolayers. For such a sample preparation, the whole surface is completely covered with NaCl. Crashing the tip on NaCl can lead to severe contamination of the tip and thereby impedes the preparation of a sharp and clean tip. For this reason we designed a mask, which is shown in Fig. 3.4. This mask is slipped onto the sample holder after preparing a clean metal surface to screen half of the surface during NaCl evaporation. In this way, one part of the surface remains clean metal. Before starting an experiment, the tip can be prepared on the clean metal side and then moved to the NaCl covered side for experiments.

4 Determination of structural relaxations in a single molecule upon charging

The experiments presented in this chapter were carried out and interpreted in collaboration with Laerte Patera, Felix Simbürger, Fabian Queck, Ingmar Swart, Bruno Schuler, Leo Gross, Nikolaj Moll, and Jascha Repp and were published in the journal Physical Review Letters [71][1]*. Parts of the text and figures are identical to the publication. Most of the experimental data shown here have been acquired in collaboration with Felix Simbürger and Laerte Patera. The data is also presented in great detail in Felix Simbürger's Master Thesis* [86]*. In order to be able to interpret the experimental data, supporting DFT calculations had to be done. These calculations were preformed by Nikolaj Moll and allowed a detailed understanding of the experimentally observed relaxations. The interpretation and analysis of experimental data based on the supporting simulations will be presented in this chapter.*

The structural changes within copper(II)phthalocyanine deposited on an ultrathin NaCl film grown on Cu(100) upon single-electron charging are quantified by means of AFM.

Making use of the charge bistability on this specific substrate system, we imaged the same molecules in different charge states. Those images reveal distinct contrast changes upon charging.

A comparison to density functional theory (DFT) simulations allowed us to relate these contrast changes to relaxations of the molecule's geometric structure upon charging. The DFT calculations further indicate that the primary origin of the contrast differences can be related to structural changes within the molecule, whereas local variations of the electrostatic interaction due to the excess charge seem to be negligible.

---

[1] P. Scheuerer, L. L. Patera, F. Simbürger, F. Queck, I. Swart, B. Schuler, L. Gross, N. Moll, and J. Repp. *Charge-Induced Structural Changes in a single Molecule Investigated by Atomic Force Microscopy.* Physical Review Letters **123**, 066001 (2019)

4.1 Introduction

Many chemical reactions rely on electron transfer [47, 87–90]. Such electron-transfer reactions are accompanied by structural relaxations of a molecule and its environment, which in turn act back on the electronic states. These relaxations upon charge transfer cause an energy gain, which is known as Marcus reorganization energy [47]. The magnitude of the reorganization energy is decisive for the rate of redox reactions and hopping conduction in organic materials, for example [91–93].

In the last years several STM studies have provided insights into impacts of electron transfer on the electronic properties of single atoms and molecules [7, 8, 11, 14, 31, 36, 48–51, 60, 94–102]. Furthermore, recent AFM experiments based on detecting single-electron tunneling events in individual molecules, adsorbed on insulating materials, enabled to quantify the hole reorganization energy [60], and to resolve orbital changes upon electron transfer with ångström resolution [36].

Whereas those studies allowed to gain valuable insights into the effect of electron transfer on the electronic structure, so far, the geometric changes within a single-molecule upon charge transfer have not been investigated in detail. However, to gain a fundamental understanding of the interplay of charge and structure, both the geometric and electronic effects need to be considered. For example, a deeper insight into such charge-induced relaxations could open the possibility to engineer hopping conduction.

The results, presented in this chapter, were motivated by previous experiments in our research group by Swart and coworkers, who measured the influence of an additional electron on the tunneling barrier by means of STM [8]. Therefore, they exploited the fact that copper(II)phthalocyanine (CuPc) molecules adsorbed on a bilayer of NaCl on Cu(100) can stably exist in two different charge states, which is commonly referred to as charge bistability. This coexistence of two stable charge states is limited only to a small range of bias voltages - typically in the order of tens of mV up to several hundreds of mV - and depends mainly on the reorganization energy but also the tunnel coupling to the tip and the underlying conductive substrate [8].

Making use of this bistability, they subsequently recorded STM images of CuPc in distinct charge states at the same bias voltage. The corresponding difference image indicated a two-fold symmetric electron distribution despite the molecule's four-fold rotational symmetry [8]. This symmetry breaking was found to originate from a lifted degeneracy of the formerly two-fold degenerate LUMO upon charging, caused by a geometrical distortion due to the Jahn-Teller effect [99]. The Jahn-Teller effect is a structural distortion that causes an energetic lowering of one of the formerly degenerate LUMO levels at the cost of increasing the energy of the other upon adding a single electron [99, 103].

This raised the question, how the structure of CuPc changes upon charging. In order to gain insight into these relaxations, we used AFM with CO-functionalized tips [9] to image CuPc subsequently in both charge states with sub-angstrom resolution. To visualize the subtle local contrast changes in the AFM images, we created difference images. In combination with simulated AFM images, based on relaxed geometries as obtained from DFT, we could interpret and quantify the minute relaxations that occur within single CuPc molecules upon charging.

4.2 Methods

For the experiments shown in this chapter, we used a Cu(100) surface, which was prepared as described in the previous chapter. NaCl of ≈ 0.3 monolayer coverage was deposited onto the sample at a temperature $T \approx 5\,^{\circ}\mathrm{C}$. Both, CO molecules for tip functionalization [9] and Copper(II)phthalocyanine were deposited onto the 7 K cold sample.

The given bias voltages refer to the sample with respect to the tip. All AFM images were acquired at constant height (i.e. with disabled feedback-loop) with a CO-functionalized tip at zero bias for molecules adsorbed on a two monolayers (2ML) NaCl film. The experimental tip heights are provided as z-offsets relative to the constant-current STM set-point, where a positive value (z-offset > 0) indicates a displacement away from the sample. Whereas CuPc can adsorb both centered at Cl^{-} and at Na^{+}, charge bistability only occurs in the latter adsorption site [99], which is therefore the only one considered here. In this configuration the four isoindole units are aligned with the non-polar directions of NaCl. Density functional theory (DFT) calculations were performed using the FHI-aims code with numerical atomic orbitals as the basis functions [104]. The Heyd-Scuseria-Ernzerhof (HSE) [105] exchange-correlation functional with an admixture of exact exchange of 0.8 and a van der Waals (vdW) method [106, 107] was applied for all calculations. AFM image simulations are based on a vdW attraction derived from semiempirical potential [108] and Pauli repulsion calculated from the electron densities from DFT [109]. The latter are converted to a frequency shift using the experimental k_{qPlus}. Lateral distortions due to the CO-functionalized tip [110] are simulated using a lateral spring constant of $k_{\mathrm{CO}} = 0.14\,\mathrm{N/m}$ [77]. Relative tip height changes in experiments are well-controlled and were enforced in the simulations, only the global offset to an absolute tip height was adjusted in the simulations. Tip heights of the latter refer to distances between the CuPc molecular plane and the center of carbon in the CO-tip. For better comparison, the attractive Δf background value from the clean surface was subtracted from the AFM images shown in Figs. 4.3-4.9.

4.3 Charge bistabiltiy of CuPc

As found by Swart et al., CuPc (see Fig. 4.1a for a structure model) exhibits charge bistability if being adsorbed on bilayer NaCl/Cu(100), which becomes clear from the hysteresis in $I(V)$-spectra acquired above the center of a molecule as shown in Fig. 4.1b [8]. In the forward voltage sweep the current drops around 200 mV, indicating

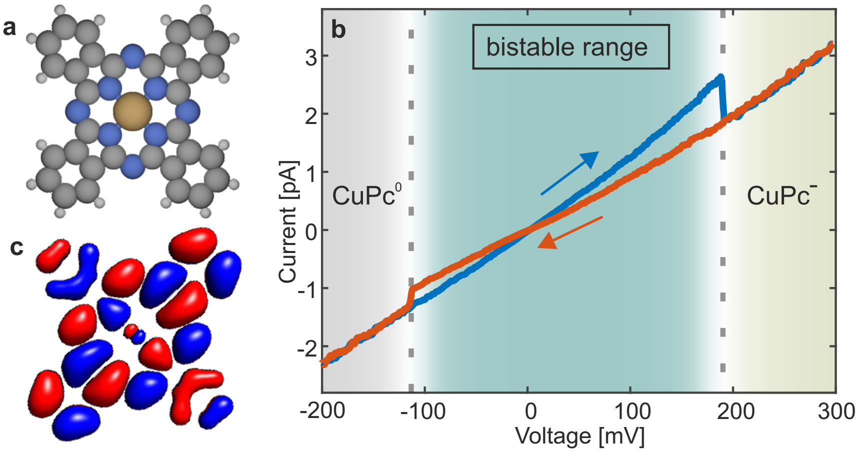

Figure 4.1: **a** Structure model of a CuPc molecule. Hydrogens (white), carbons (grey), nitrogens (blue) and copper (brown). **b** $I(V)$-spectrum of a CuPc molecule on NaCl(2ML)/Cu(100). **c** LUMO of CuPc.

that the molecule became negatively charged, whereas the discharging event in reverse sweep direction occurs at a lower bias voltage ($\approx -100\,\text{mV}$). Within this voltage range the molecule is bistable and can be deliberately imaged in both charge states. The charge bistability originates from the CuPc's LUMO energy (which is related to the molecule's electron affinity) being roughly aligned with the Fermi level of the supporting conductive substrate [6, 8, 99]. Upon charging, one of the former LUMO levels shifts across the Fermi level due to the reorganization energy [47], which enables the stabilization of the molecule in its anionic state in a limited voltage range. Figure 4.1c shows one of the two degenerate lowest unoccupied molecular orbitals (LUMO) as calculated for the neutral molecule in the gas phase. Due to the Jahn-Teller effect, the orbital degeneracy is lifted upon electron injection [99]. Hence, the additional charge is distributed non-homogeneously over the molecule.

4.4 Analysis of the AFM contrast

Figures 4.2a and 4.2b show zero-bias constant-height CO-tip AFM images of two CuPc molecules, where one molecule was selectively charged between the image acquisitions. To highlight the changes in the AFM contrast upon charging, the second image was subtracted from the first. The resulting difference image is shown in Fig. 4.2c, and reveals distinct intra-molecular contrast for the molecule that became charged. The fact that the contrast difference for the lower molecule is vanishing, rules out that the two AFM images were acquired at different heights or that a tip change occurred in between acquisition of the images. Hence, these intra-molecular contrast changes are attributed to the addition of a single electron.

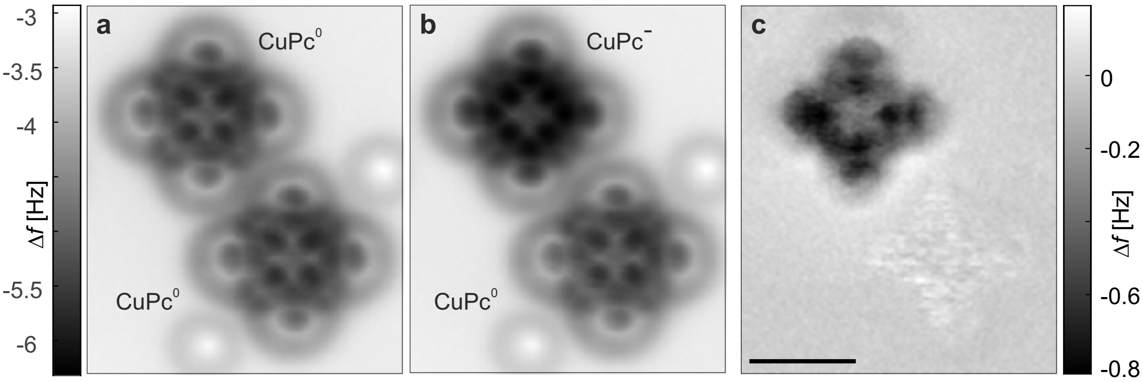

Figure 4.2: Constant-height AFM images recorded with a CO-tip of **a** two neutral CuPc and **b** after charging the top-left molecule with a single electron. **c** Difference image (**b**−**a**). AFM images were recorded with a z-offset of 1.65 Å with respect to the STM set-point ($I = 1\,\mathrm{pA}$, $V = -0.2\,\mathrm{V}$). The scale bar corresponds to 10 Å.

To clarify the subtle details of this contrast change upon charging, we took images of a CuPc molecule subsequently in both charge states at ultimate resolution, which is shown in Fig. 4.3. Here, red and yellow crosses mark the positions of the bond ridges corresponding to the peripheral rings, and black and blue crosses mark characteristic positions at the central unit of the molecule. Importantly, all markers are at identical positions in all three images, such that contrast differences in Fig. 4.3c can be attributed to different regions in Figs. 4.3a and 4.3b.

From comparison of Figs. 4.3a and 4.3b it becomes clear that the contrast at the central unit varies most in intensity. Notably, the bond ridges at the periphery appear at identical lateral positions. The fact that there are no apparent lateral shifts of bond ridges suggests that image distortions due to CO bending at the tip apex [74, 77, 111–114] are similar in both cases and contrast in the difference image in Fig. 4.3c is not dominated by CO bending. If the contrast differences were dominated by such image distortions, they should exhibit features that locally match a lateral derivative of the original images. The contrast in the difference image in Fig. 4.3 is incompatible with that, further indicating that CO bending is not dominant here. In contrast to STM, which essentially measures the LDOS near the Fermi level [9, 30], AFM is rather sensitive to the total electron density [38]. CuPc^0 has a total number of 293 electrons. Considering that the additional charge is rather delocalized over the entire molecule [8, 99], it is not surprising that the CO bending does not play a crucial role here.

Beside other possible contributions, the charging will change the electrostatic contributions to the force [15, 43, 52–54, 115, 116] and should affect the local contact potential difference (LCPD), which can be quantified by Kelvin probe force spectroscopy (KPFS) [11, 14, 31, 38, 39]. Hence, KPFS could be employed to measure the difference in charge distribution within the molecule. However, due to the nar-

row voltage window of charge bistability, determination of the LCPD for both charge states, is prevented.
Irrespective of these considerations, due to the four-fold symmetry of the difference image, the contrast in the difference image cannot be simply ascribed to the charge distribution of the additional electron, since the occupied former LUMO of CuPc^- is two-fold symmetric [8, 99] (see Fig. 4.1c). For a further DFT based analysis of electrostatic contributions to the contrast formation, it is referred to the next section. Instead, the four-fold symmetric contrast of the difference image shows mainly two distinct features: except at the center, the contrast difference appears to be similar to the inverse of the intra-molecular contrast of the original AFM images. This could indicate that the observed contrast mainly originates from a vertical relaxation of the molecule: if the charged molecule was adsorbed closer to the surface than the neutral one, the short-ranged Pauli repulsion between tip and molecule would be decreased such that the intra-molecular contrast is weakened. Hence, the difference image should show an inverted intra-molecular contrast. This seems to qualitatively agree with the observed contrast in the difference image except for the molecule's center.

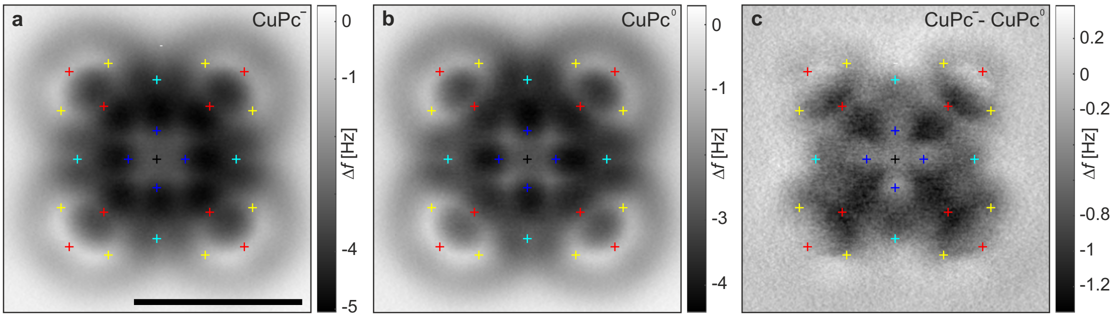

Figure 4.3: High-resolution AFM images recorded with a CO-tip of **a** CuPc^- and **b** CuPc^0. Both images were recorded at the same tip height (z-offset = 1.6 Å with respect to the STM set-point of 1.1 pA at 90 mV). **c** Difference image ($\mathrm{CuPc}^- - \mathrm{CuPc}^0$). Colored crosses indicate identical positions in all the AFM images to facilitate the comparison. The scale bar corresponds to 10 Å.

To shed more light onto the contrast change upon charging, DFT calculations were performed to determine the geometries of a CuPc molecule adsorbed on NaCl(100) in both charge states. Based on that DFT-calculated geometries, AFM images were simulated [109] and difference images were created by subtraction of simulated AFM images analogous to the experiment. Since the relative strength of short-range repulsive forces and rather long-range electrostatic forces depends on the absolute tip height, we acquired a set of constant-height AFM images of the molecule from Fig. 4.3 in both charge states at various tip heights and created corresponding simulated images for three distinct contrast regimes.

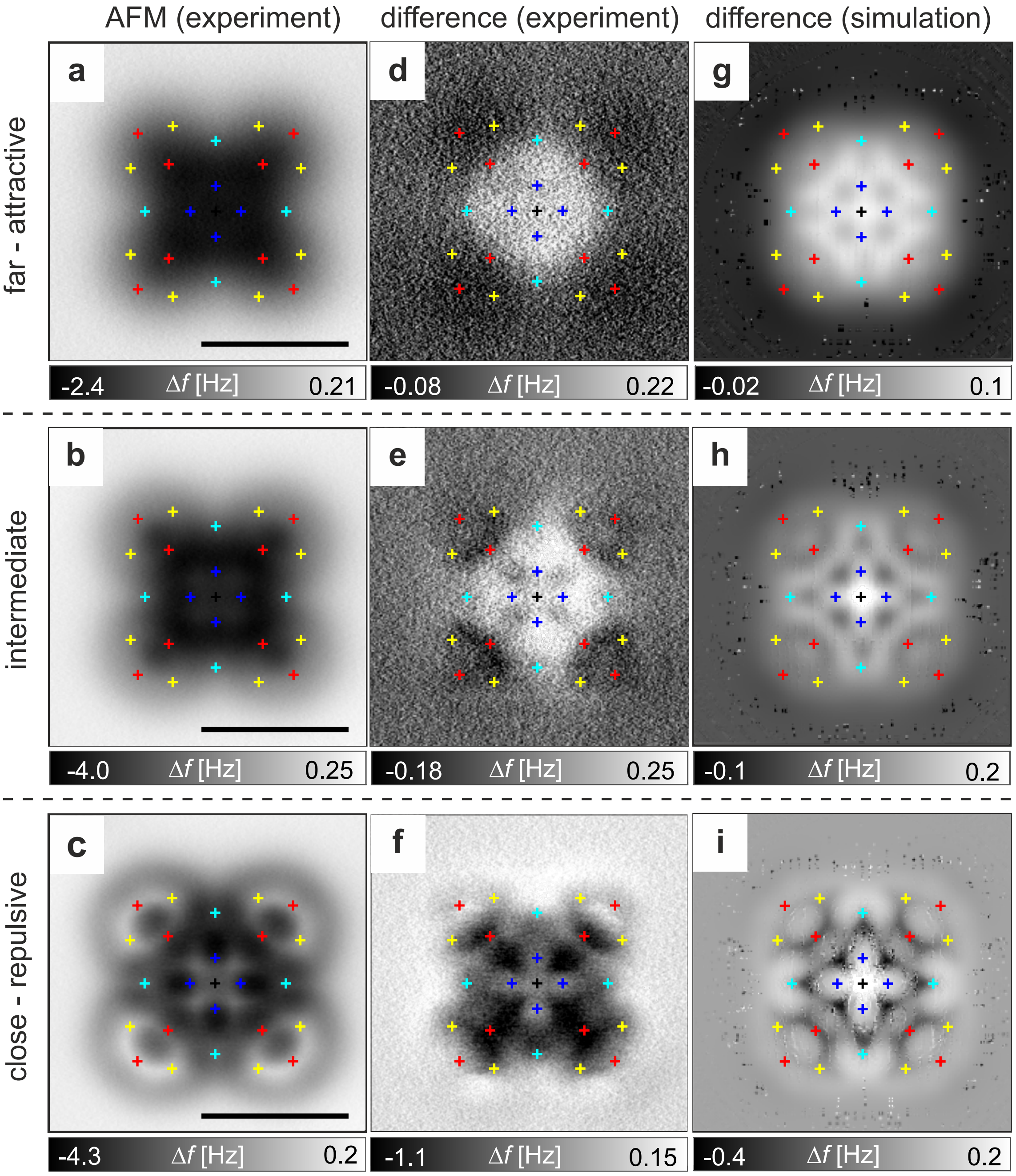

Figure 4.4: **a-c** Constant-height AFM images of CuPc^0 at different tip heights. **d-f** CuPc$^-$−CuPc^0 difference images from experimental AFM data and **g-i** from simulated AFM images. Z-offsets are **a, d** 2.6 Å, **b, e** 2.1 Å, **c, f** 1.6 Å with respect to an STM set-point of 1.1 pA and 90 mV. Tip heights for simulated images are 5.8 Å in **g**, 5.3 Å in **h**, 4.8 Å in **i**. Scale bars correspond to 10 Å.

Figure 4.4 shows a comparison of experimental and simulated difference images for three different height regimes. For each of the distances, the experimental AFM images of CuPc^0 (Figs. 4.4a-c), the corresponding experimental (Figs. 4.4d-f) and simulated (Figs. 4.4g-i) difference images are displayed. At close distance (Figs. 4.4c), the images of CuPc^0 show intramolecular contrast originating from Pauli repulsion superimposed to an attractive smooth background from vdW interactions. Due to the short-range nature of Pauli repulsion, at comparably large imaging distances (Fig. 4.4a), the long-range attractive vdW background forces determine the image contrast.

Remarkably, the key features in experiments and simulations are in good agreement at all tip heights. In the attractive regime (Figs. 4.4d,g), both experiment and simulation show a bright feature enclosed in the cyan markers. The experimental difference image displays faint depressions at the periphery, which are barely visible in the simulations. In the intermediate regime (Figs. 4.4e,h), the experimental and simulated image consistently show a bright feature enclosed in red and yellow markers and a bright cross in the center (black and blue markers). At close distances, similar observations can be made (Figs. 4.4f,i). Due to the increased intermolecular contrast in the experimental images the central cross can be clearly distinguished from the contrast features at the cyan markers, giving and excellent agreement with the simulations. Generally, most features look more blurred in the experimental data. This reduced sharpness could be caused by non-local force contributions from the metallic tip, which is not accounted for in the simulations.

Furthermore, electrostatic interactions between tip and molecule are not included in the simulations. Since the additional electron is expected to be rather delocalized over the entire molecule and electrostatic forces are comparatively long-range, we assume that such an electrostatic contribution in the AFM images should only cause a homogeneous contrast contribution over the molecule. In fact, such a homogeneous contribution would be in line with the differences between experiment and simulations. The fact that the experiments were conducted with a very small oscillation amplitude of 0.5 Å, also increases the sensitivity to short-range Pauli repulsion in comparison to the long-range electrostatic contributions [84]. Moreover, in probe-particle image simulations, CO-functionalized tips were approximated with a zero monopole charge for best agreement with experiment[113, 117]. For those reasons, we infer that CO-functionalized tips in our experiments are comparably insensitive to electrostatics.

4.5 Electrostatic contributions to AFM contrast

The experimental data suggest that the image contrast is not much affected by electrostatic contributions from the additional electron but is rather attributed to structural relaxations of the molecule. In the following, we discuss the role of those contributions based on the results of the DFT calculations and the image simulations.

4.5.1 Disentanglement of geometrical and charge contributions

As discussed for the experimental data, the contrast change upon charging could in general have two possible contributions, which are electrostatic contributions arising from the additional charge itself, but also from the geometrical relaxations that occur upon charging. Regardless of the aforementioned arguments for negligible electrostatic contributions based on plausibility considerations, in general, electrostatic forces can significantly contribute to the overall contrast change in AFM images upon charging [113, 114]. Hence, we made an attempt to disentangle the contribution from geometric relaxations upon charging in simulated images from the electrostatic contributions by performing the following DFT calculations: First, the neutral molecule is calculated in its fully relaxed geometry. Next, the calculations are performed for the system with one additional charge, but without relaxing the geometry. Finally, the latter system is allowed to relax again, resulting in the charged molecule in its relaxed geometry. In the following considerations, we refer to the relaxed geometry of the neutral molecule as *neutral geometry* and to the relaxed geometry of the charged molecule as *charged geometry*. Based on these three different geometries, namely, neutral in the *neutral geometry*, charged in the *neutral geometry*, and charged in the *charged geometry*, AFM images were simulated. We then created difference images according to the scheme in Fig. 4.5 which are compared in Fig. 4.6.

Figure 4.6a-c shows conventional difference images created from simulated AFM images for the different tip heights. Figure 4.6d-f shows corresponding simulated difference images that only contain contributions from geometrical changes because they are obtained by subtracting the molecule in the *neutral geometry* from the one in the *charged geometry*, both calculated for the anionic state. In contrast, Figure 4.6g-i shows the corresponding difference images arising solely from the additional charge, as they are obtained by subtracting the molecule fixed in the neutral geometry but different charge states (anionic minus neutral). Since the images of each row are displayed at the same grayscale, it becomes immediately apparent that the contribution from geometrical relaxations dominates whereas the charging effect itself makes up only a small fraction of the image contrast.

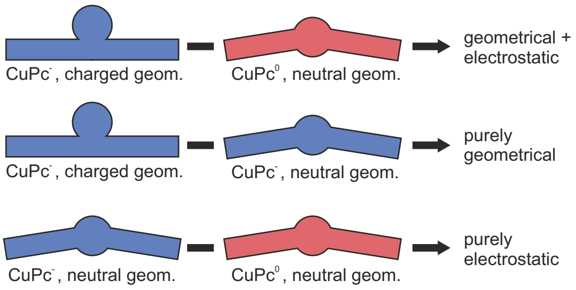

Figure 4.5: Schematic picture showing how the electrostatic and geometric contrast contributions can be disentangled by suitable image subtraction

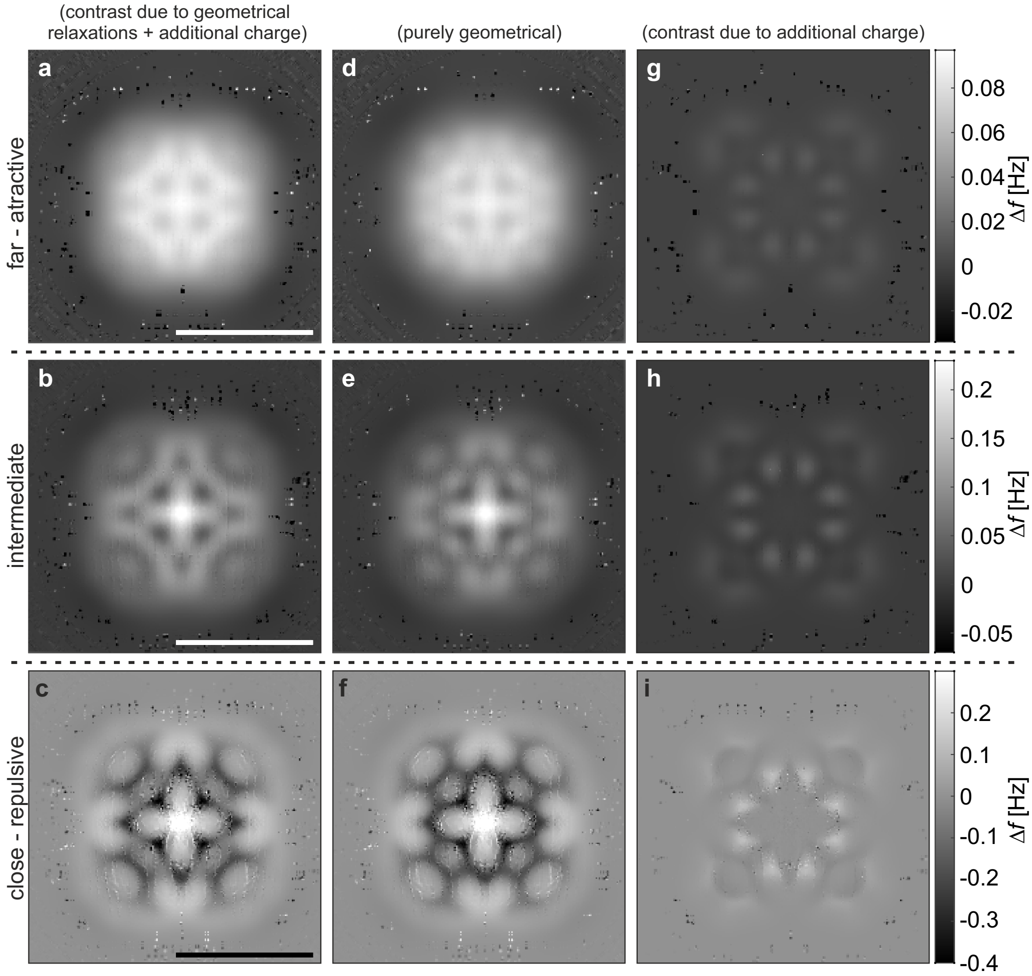

Figure 4.6: Difference images of simulated AFM images. **a, b, c** Conventional difference image of CuPc$^-$ in *charged geometry* minus CuPc^0 in *neutral geometry.* **d, e, f** Difference images related to geometric changes : CuPc$^-$ in *charged geometry* minus CuPc$^-$ in *neutral geometry.* **g, h, i**: Difference images related to the change in charge CuPc$^-$ in *neutral geometry* minus CuPc^0 in *neutral geometry.* Tip heights are 4.8 Å **a, d, g**, 5.3 Å **b, e, h**, and 5.8 Å **c, f, i** and refer to the distance between the molecular plane and the center of the carbon in the CO-tip. Scale bars correspond to 10 Å.

4.5.2 Role of a possible tip polarization

Even though electrostatic interactions are found to be negligible, the additional charge injected into the molecule upon charging might polarize the charge in the CO molecule at the tip, such that its imaging properties change. Such an interaction was described by Corso et al. [118]. If the CO molecule was affected in this way, it might simply image the sharp Pauli repulsion differently. To clarify whether such a polarization effect could contribute to the image contrast, we extracted the vertical derivative of the Hartree potential from the DFT calculations. Since the Hartree Potential represents approximately the classical electrostatic potential in DFT, its derivative should approximate the vertical component of the electric field E_Z^{Hartree}, which could potentially lead to a polarization of charge in the CO-tip.
By taking suitable differences from the three calculations in different geometries and charge states, according to the method described above, we disentangled the changes in E_Z^{Hartree} due to the geometrical changes (Fig. 4.7a) and those arising from the additional charge (Fig. 4.7b). The vertical planes in which the $\Delta E_Z^{\text{Hartree}}$ is visualized correspond to the tip heights in the simulations. The images are displayed at the same colorscale, and it becomes immediately apparent that also here, the geometrical relaxations affect E_Z more than the charging itself.

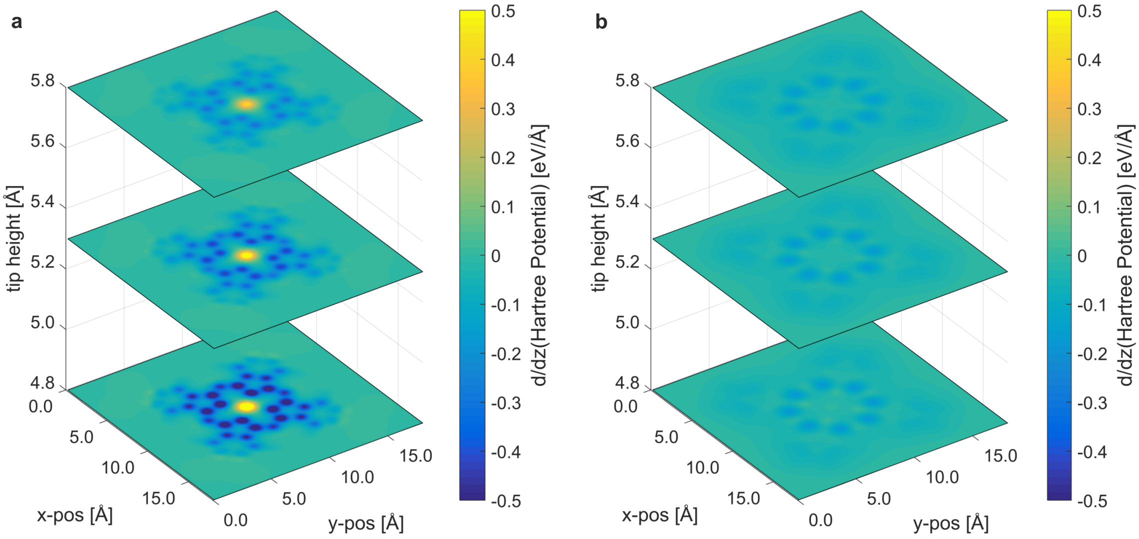

Figure 4.7: Slice plots of differences of the vertical component of the electric field $\Delta E_Z^{\text{Hartree}}$, derived from the vertical derivative of the Hartree potential. The three slices correspond to the tip heights 4.8 Å, 5.3 Å and 5.8 Å. **a** Contribution from geometrical changes in the molecule to $\Delta E_Z^{\text{Hartree}}$, derived as the difference of CuPc$^-$ in *charged geometry* minus CuPc$^-$ in *neutral geometry*. **b** Contribution to $\Delta E_Z^{\text{Hartree}}$ from charging, derived as the difference of CuPc$^-$ in *neutral geometry* minus CuPc^0 in *neutral geometry*.

These results suggest that different electrostatic interactions occurring upon charging, either directly in CuPc or indirectly in the CO molecule at the tip, are rather small and the main cause for the contrast change are the geometric relaxations that occur upon charging CuPc.

4.6 Structural changes upon charging

The relaxations of CuPc upon charging are analyzed in Fig. 4.8a,b based on the DFT calculated geometries. Since the relaxations and also the deviations from a planar geometry are tiny, we magnified them by a factor of 10 with respect to a plane of average height of atoms in CuPc^0. In the neutral state (Fig. 4.8a, the molecule has an umbrella-like geometry, being bent towards the NaCl surface at the periphery. Upon charging (Fig. 4.8b) the molecule relaxes towards the substrate and flattens out. Only the Cu-atom relaxes by 5 pm *away* from the surface. The height of the outmost carbons and hydrogens almost remains unchanged. This relaxation pattern rationalizes the observed contrast change in the images in Fig. 4.3. Whereas the very periphery looks almost identical in the AFM images, the contrast inversion at the central unit of the difference image is in line with the vertical relaxation towards the surface. The opposite relaxation of the central Cu atom is also in agreement with the experimental observations of an increased Δf at the very center of the difference image. The contrast change in the other distance regimes can be rationalized along similar lines. We note that the contrast change at the central metal atoms – although qualitatively reproduced – seems overestimated in the simulations.

Furthermore, the observed relaxation pattern can be related to the difference in charge densities between CuPc$^-$ and CuPc^0, as calculated from DFT, which is shown in Figs. 4.8(c-d). The charge density is increased in the π-system close to the molecule's center around the Cu atom. At the Cu atom, in contrast, the charge density appears to be decreased. Since the Cu is situated above a Na$^+$ ion, the decreased electron density causes a local repulsive electrostatic contribution that pushes the Cu atom upwards. The strongest increase in charge density occurs at the central unit of CuPc, whereas at the periphery, the charge density difference is much smaller. In general, neutral molecules primarily interact with insulating films via vdW forces, however, in case of polar functional groups or local charges, electrostatic forces can also significantly influence the adsorption energy of molecules [119–124]. Further stabilization can arise from charge screening in the substrate [7]. Here, the additional electron could lead to such an additional electrostatic contribution, and the non-homogeneous distribution of the additional charge in CuPc$^-$ agrees well with the relaxations described above. In STM experiments, we observe a two-fold symmetric appearance of the lowest-lying electronic resonance when tunneling into the already charged CuPc$^-$, in agreement with previous STM experiments, indicating that the extra electron populates one of the former LUMOs of CuPc. The DFT calculations, in contrast, claim that the excess charge in CuPc$^-$ populates the former singly occu-

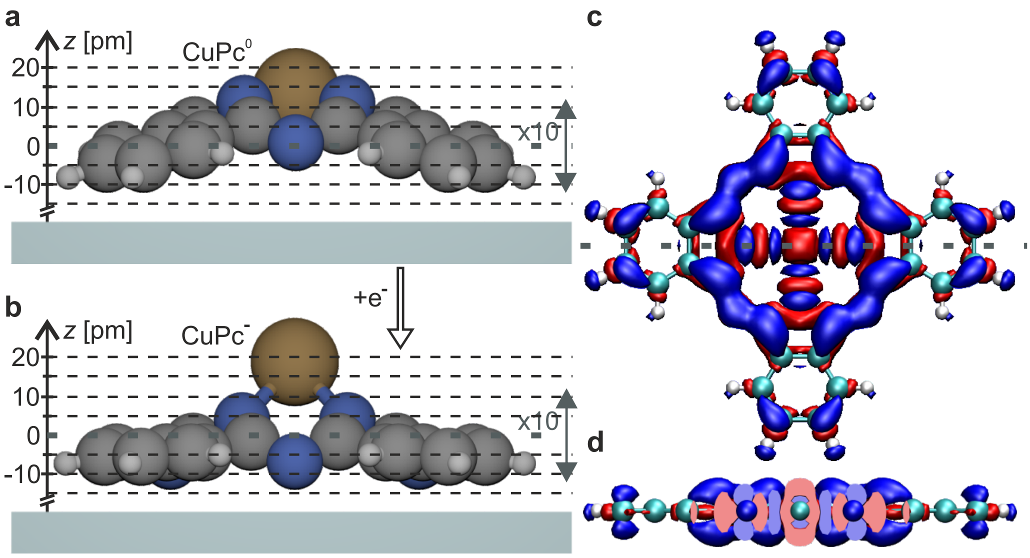

Figure 4.8: 3D models showing the geometry of **a** $CuPc^0$ and **b** $CuPc^-$. The differences of the vertical coordinates of both species with respect to a reference plane (dashed line) are displayed magnified by a factor 10 along the vertical direction. Charge density difference maps of a free CuPc molecule **c** top view and **d** cut through the molecule. Blue and red corresponds to an increase and decrease of electron density, respectively. The dashed line in **c** indicates the position of the cut through the molecule. The backbone of the molecule is shown for clarity.

pied b_{1g} orbital, being more strongly localized at the center. This may explain why the contrast change at the very center is overestimated in the simulations. We note that the question, which orbital the excess electron occupies is governed by a subtle energy balance, in which the Coulombic charging energy depends on the degree of delocalization [125], the surrounding [99] and screening. It is known that different DFT functionals favor delocalization to a different degree. We note that DFT calculations for the free anion in the gas phase provide a different population of states as compared to the adsorbed case.

Finally, we estimate this vertical relaxations based on experimental difference images. Therefore, we subtract AFM images of $CuPc^0$, which were recorded at different z-offsets, from an image of $CuPc^-$ at a given z-offset. The difference in z-offset between the subtracted images is defined as Δz, where $\Delta z < 0$ corresponds to a smaller tip height for $CuPc^-$. The idea is that the z-offset should cancel out the vertical relaxations of the molecule. If the z-offset equals the vertical relaxations, the intramolecular contrast arising from Pauli-repulsion should be similar in the images and hence the contrast in the difference images should vanish.

Figure 4.9a-c shows such difference images, for three different Δz values. These images show that the contrast is inverted in between $\Delta z = -0.05$ to $-0.15\,\text{Å}$ and is canceled out best at a height offset $\Delta z \approx -0.1\,\text{Å}$, which suggest that the average vertical relaxation upon charging is on the order of $-0.1\,\text{Å}$. This value has a good agreement with the vertical relaxations, which were found in the above DFT-calculated geometries. The remaining contrast in the images is in line with a non-homogeneous relaxation of the molecule. The fact that the vertical relaxations are stronger at the center than in the periphery of the molecule can qualitatively already be deduced from the difference image shown in Fig. 4.3. This analysis shows that vertical relaxations can be extracted from the experimental AFM data with a precision of about 5 pm.

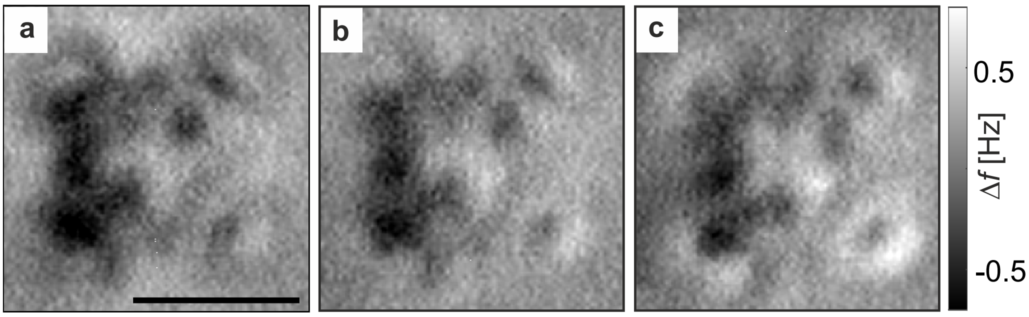

Figure 4.9: **a-c** Difference images of CuPc with $\Delta z = -0.05\,\text{Å}$ **e**, $-0.10\,\text{Å}$ **f**, and $-0.15\,\text{Å}$ **g**.

4.7 Conclusion

In this chapter we investigated how the molecular structure of individual CuPc molecules adsorbed on NaCl(2ML)/Cu(100) changes upon charging with a single electron. A comparison between subsequently recorded AFM images with sub-molecular resolution of the same molecule in the anionic and neutral state indicated a non-uniform relaxation of the molecule in the singly charged state. Those contrast changes were highlighted by image subtraction in different contrast regimes and yield good agreement with simulated difference images based on relaxed geometries obtained from DFT calculations. The calculated geometries of the two neutral and anionic states reveal non-homogeneous vertical relaxations of below 10 pm within the molecule upon charging, which is in agreement with the estimations based on experimental data. Further, the DFT calculations suggest that the observed contrast is dominated by the geometrical relaxations, whereas the contrast attributed to the electrostatic contributions is negligible. The fact that pm-scale relaxations can lead to distinct contrast changes in images underlines the large sensitivity of AFM.

5 Molecular self-assembly on insulating films

The remaining chapters of this thesis comprise experiments on self-assembled molecular structures on insulating films. This chapter gives a brief introduction and literature overview of molecular self-assembly on insulating surfaces. Further, the specific substrate system NaCl/Au(110) is introduced, which we used for the self-assembly experiments. Finally, we discuss the growth mode of self-assembled perylene-3,4,9,10-tetracarboxylic dianhydride (PTCDA).

5.1 Introduction

Molecular self-assembly is the process of forming ordered structures consisting of individual molecules based on non-covalent interactions [13, 126] and has become a common method to grow molecular structures with atomic-scale order on a supporting substrate [13, 15, 102, 120–124, 127–141]. The basic idea is schematically depicted in Fig. 5.1. Molecules are deposited on a crystalline sample, where their diffusive motion at the surface can be controlled by the temperature. Upon interactions of molecules with other diffusing molecules at the surface a nucleation process starts, where molecules arrange in energetically favorable structures. The precise structure of such assemblies depends on the specific molecules, especially the presence of functional groups, which determine the linking possibilities between molecules, e.g. via hydrogen bonds, and impact the adsorption geometry to some extent [13, 122, 123, 129]. Countless molecular self-assembly experiments in SPM have been conducted on metallic surfaces [13, 127–129, 142–145]. To maintain and study the electronic properties of self-assembled molecular structures, an insulating substrate is required.

However, insulating materials have the disadvantage that molecule-substrate interaction is typically much weaker than on metal substrates, which makes it more challenging to grow self-assembled molecular structures on insulating substrates [119, 122, 123, 134, 139, 141].

A review article of Rahe and colleagues [123] points out this challenges for self-assembly on insulating materials and shows how molecule-substrate interactions can be tuned by using molecules with functional groups that interact exceptionally strong with the substrate [121, 122, 140, 146], matching the geometry of molecules to the substrate [124, 133, 134] and by increasing the number of functional groups that provide a strong interaction with the substrate [121, 123, 147]. In general, the relative strength of intermolecular interactions and molecule-substrate interactions are considered to be important for the resulting structure of the molecular networks [122, 123, 133]. Based on these strategies for tuning intermolecular and molecule-substrate interactions, a variety of self-assembled molecular structures have been realized on insulator surfaces in the past years, paving the way to their investigation in an electrically-isolated environment by means of SPM [15, 102, 120–124, 133–141, 148].

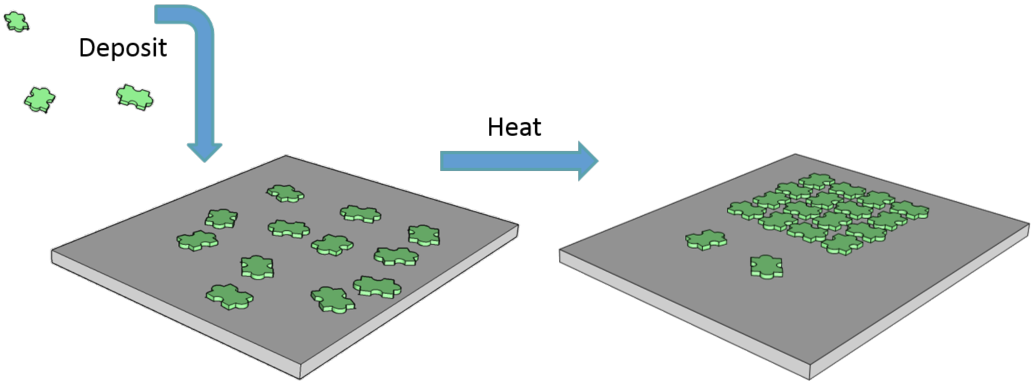

Figure 5.1: Schematic picture of molecular self assembly. **a** Deposition of molecules onto a cold substrate surface. **b** Diffusion and formation of ordered molecular structures at elevated temperature.

5.2 Au(110)

For all the self-assembly experiments Au(110) was used as a substrate, on which NaCl films of layer thicknesses ranging from below one to more than 20 monolayers (ML) were grown.

Au has a face-centered cubic (fcc) crystal structure with a lattice constant of ≈ 4.1 Å [149, 150], and its (110) plane has a rectangular unit cell with a size of 2.9 Å-by-4.1Å (see Fig. 5.2a). The (110) surface undergoes a (2x1)-reconstruction where every second row is missing, leading to a doubling of the unit cell in the direction of $\vec{a_1}$, as shown in Fig. 5.2b [151, 152]. This missing-row reconstruction can be clearly identified in STM images of a Au(110) surface as characteristic diagonal lines (see Figure 5.2c).

The molecular self-assembly experiments in this thesis require large terraces without step edges, in order to obtain isolated self-assembled islands with a homogeneous environment. We chose Au(110) as a supporting substrate because previous experiments in the group indicated that NaCl growth is commensurate with the substrate [153], which helps to achieve a homogeneous coverage with NaCl.

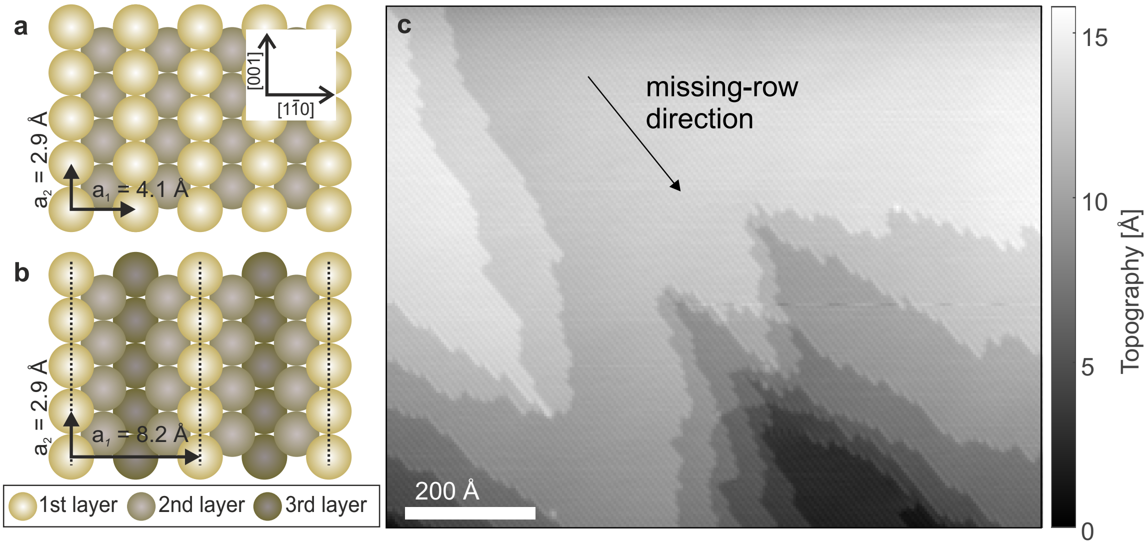

Figure 5.2: **a** Model of unreconstructed Au(110) surface. **b** Model of the missing row Au(110)-(1x2) surface reconstruction, where every second row (rows marked with dashed lines) is missing. **c** Constant-current STM image of a Au(110) surface, with characteristic diagonal lines due to the missing row reconstruction (setpoint: 4.5 pA, 0.98 V).

5.3 Growth Characterization of NaCl/Au(110)

For the purpose of electronic decoupling [6], NaCl is one of the most commonly used materials in scanning probe microscopy. Bulk NaCl has a fcc crystal structure with a lattice constant of 5.64 Å [154] with a two-atomic basis, which gives a next-neighbor distance of equal ions of ≈ 3.99 Å. Films of NaCl we grown by thermal evaporation onto a clean Au(110) surface as described in chapter 3.

Figure 5.3a shows a constant-current STM image of a Au(110) surface with an average coverage of ≈ 0.8 ML NaCl deposited at $T \approx 320$ K. The Au(110) surface missing rows run from top left top bottom right of the STM image. The islands with the stripe pattern perpendicular to the direction of the missing rows are attributed to monolayer islands of NaCl (partially highlighted with green frames). Those islands show a moiré pattern of ≈ 12 Å periodicity probably originating from the difference in the periodicity of Au(110) (2.9 Å) in direction of the missing rows and the distance of equal ions in NaCl (3.99 Å).
This growth mode and the resulting moiré pattern of monolayer NaCl on Au(110) is visualized in Fig. 5.3. Note that this scheme is intended only to highlight the lattice periodicities in the [100]-direction of the surface, whereas the alignment of the ionic species with respect to the [1$\bar{1}$0] direction of the surface is chosen arbitrarily.

Along the moiré stripes the NaCl film appears flat, indicating that the Au(110) surface is unreconstructed underneath the NaCl films. Indeed, this absence of the

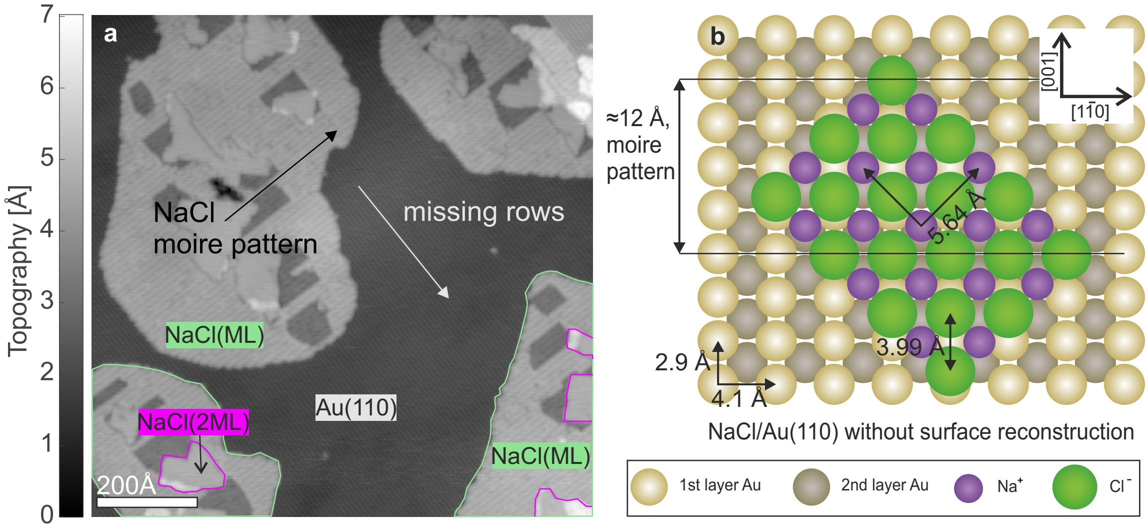

Figure 5.3: Growth mode of NaCl/Au(110). **a** Constant-current STM image of Au(110) with an average coverage of ≈ 0.8 ML NaCl grown at $T \approx 320\,\mathrm{K}$ (setpoint: 2.8 pA, 0.5 V). **b** Scheme of NaCl growth on a unreconstructed Au(110) surface.

Au(110)-(1x2) reconstruction depends on the sample temperature at which the NaCl films are grown. If NaCl is deposited at lower sample temperatures of $T \approx 295\,\mathrm{K}$, the reconstructed surface is maintained underneath the NaCl film [153]. The trenches within the monolayer NaCl islands are attributed to monolayer-deep pits in the underlying Au(110) substrate, probably resulting from a migration of Au atoms to eliminate the surface reconstruction and are absent if NaCl is deposited at higher sample temperatures. The patches (partially highlighted with purple frames) within the monolayer NaCl island that do not show the moiré pattern, are attributed to bilayer NaCl.

Figure 5.4 shows a constant-current STM image and the simultaneously recorded AFM image of an, on average, ≈ 2.5 ML thick NaCl film, which was grown at a sample temperature of $T \approx 455\,\mathrm{K}$. In the STM images, it is difficult to distinguish between the monolayer step edges of the underling Au surface and areas of different NaCl layer thickness, due to the similar apparent height of Au(110) and NaCl steps. From comparison to the simultaneously recorded Δf-image, however, the areas of different NaCl thickness can be identified from a significant change in Δf. This reveals that the whole imaged area is covered with at least two layers of NaCl, and approximately half of the area is covered with a three monolayer thick NaCl film, whereas only a small fraction of fourth and fifth layer NaCl coverage is observed. Further, it becomes evident that flat terraces of a size in the range of 100 nm can be obtained under these growth conditions, which provides an ideal basis for molecular self-assembly.

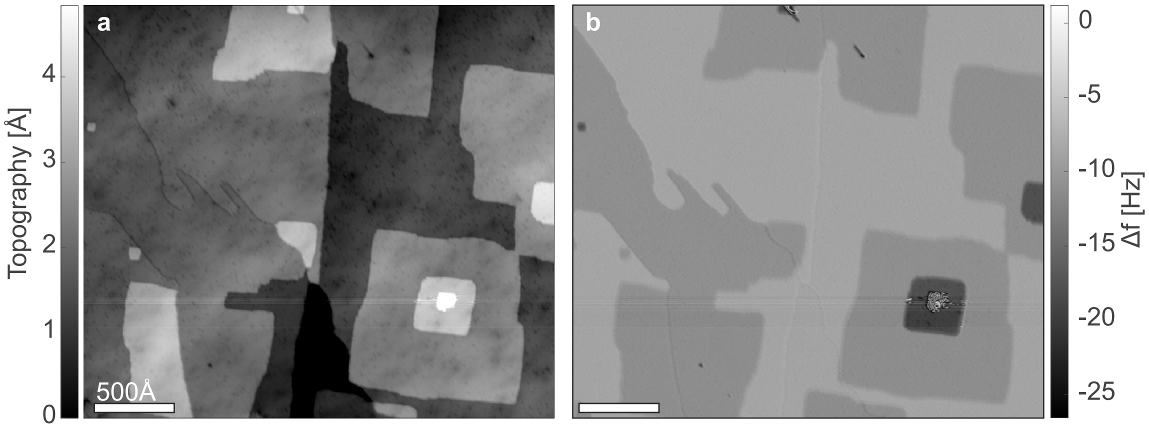

Figure 5.4: Growth mode of NaCl/Au(110). STM image **a** and simultaneously recorded Δf image **b** of Au(110) with an average coverage of ≈ 2.5 ML NaCl grown at $T \approx 455$ K (setpoint: 2.8 pA, 0,5 V).

5.4 Molecular self assembly of PTCDA on NaCl/Au(110)

For all the self-assembly experiments throughout this thesis, we used PTCDA as building blocks, whose structure is shown in Fig. 5.5. PTCDA consists of an aromatic perylene unit and two anhydride groups. Further, it is known from several studies that PTCDA forms stable self-assembled structures on insulating surfaces [141, 148, 155, 156].

After a NaCl film was grown on a clean Au(110) substrate, PTCDA molecules were deposited in-situ onto the 7 K cold sample surface by sublimation. Subsequently, the sample was taken out of the STM and annealed at ≈ 320 K for two minutes to initiate the self-assembly. Finally, the sample was transferred back to the STM.

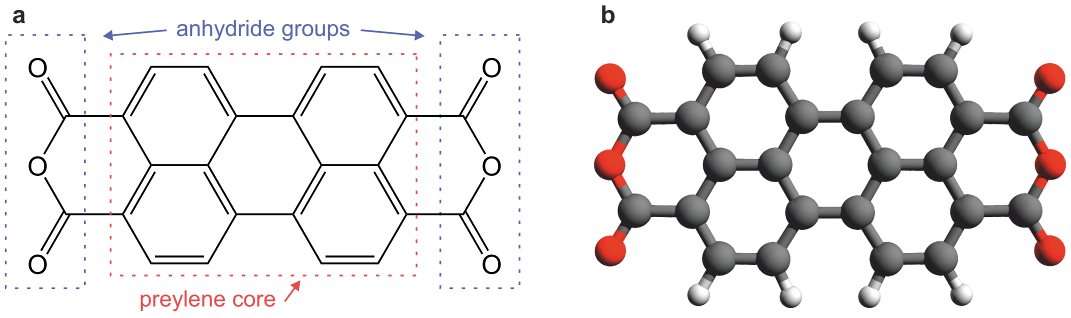

Figure 5.5: **a** Structure model of PTCDA, with the perylene core (dashed red rectangle) and the two functional anhydride groups (dashed blue rectangles). **b** Ball and stick model of PTCDA, with oxygens (red), carbons (grey) and hydrogens (white).

Figure 5.6 shows an STM image of a Au(110) surface, covered with an NaCl film of 3.5 monolayers of average thickness, after the self-assembly. Many isolated clusters of edge lengths < 100 Å can be recognized on large flat NaCl terraces. Further, it is observed that PTCDA molecules nucleate at step edges of NaCl islands.
All the self-assembled molecular structures show a diagonal stripe pattern from top left to bottom right of the image, which is parallel to the missing row direction of the underlying Au(110) substrate (not visible here).
This stripe pattern can be seen more clearly in the STM image of a 4-by-4 PTCDA molecular island (Fig. 5.7a). It originates from a superposition of dumbbell-shaped orbitals corresponding to the LUMO of individual molecules, with a nodal plane along the long molecular axis (see inset image of individual PTCDA for comparison) [148, 157, 158]. For clarity, the molecular structure of PTDCA molecules is superimposed in the upper half of the island.
The preferential growth orientation of the molecular islands with respect to the missing row direction might be related to a strained NaCl growth due to the slight mismatch of equal-ion, nearest-neighbor distance in the NaCl [100] surface (≈ 4 Å [154]) and the periodicity of Au(110) in $[1\bar{1}0]$ direction (≈ 4.1 Å [149]).

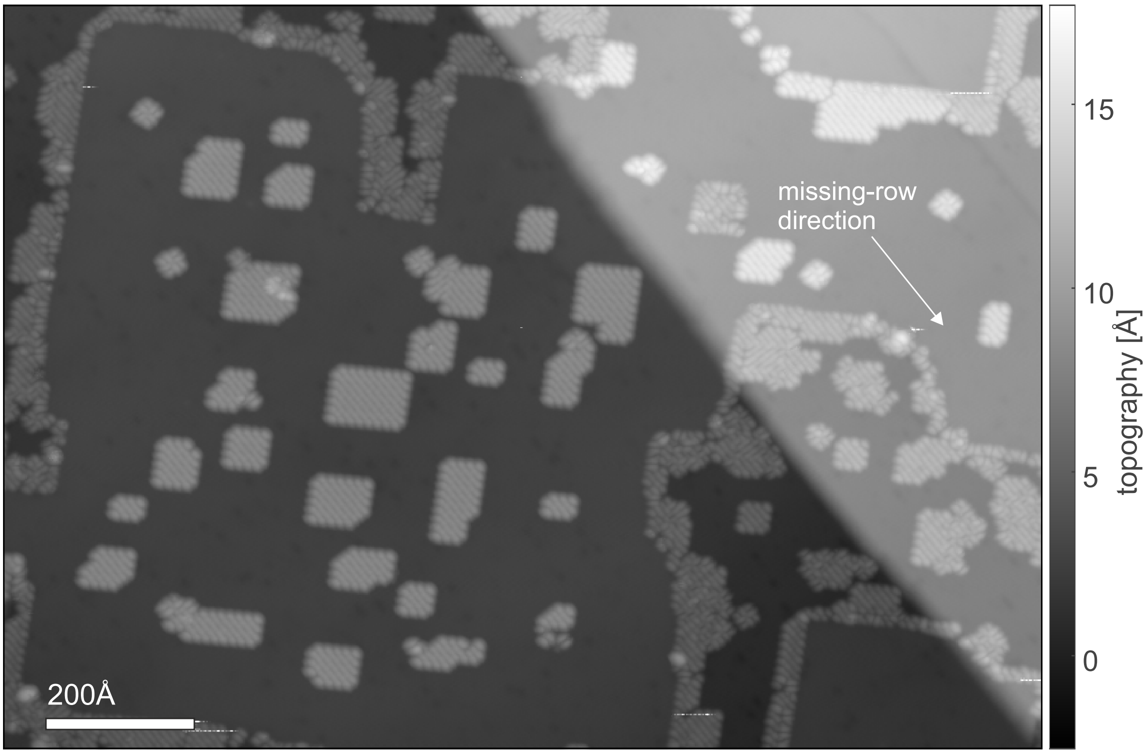

Figure 5.6: Constant-current STM image of self-assembled PTCDA islands on NaCl/Au(110). The islands show a stripe pattern, which is oriented in the same direction as the missing rows of the bare Au surface (compare Fig. 5.3) (setpoint: 1.4 pA, 1 V).

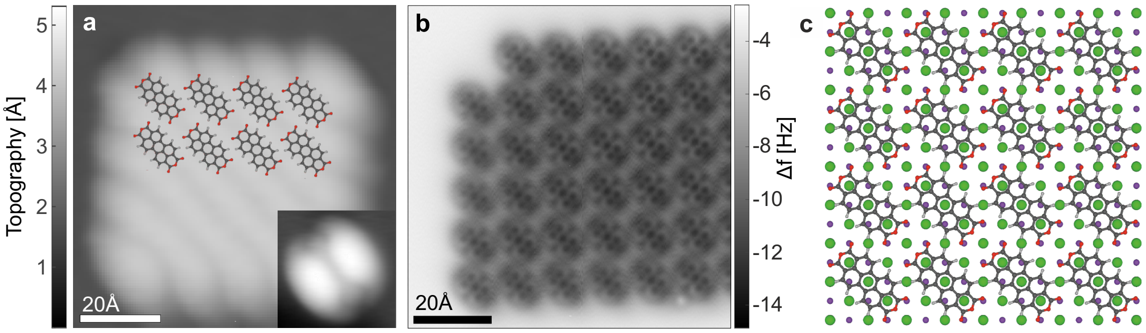

Figure 5.7: **a** STM image of a 4-by-4 PTCDA island (setpoint: 2.6 pA, 2 V). inset: STM image resembling the LUMO of individual PTCDA (setpoint: 1.8 pA, 0.93 V). **b** constant-height AFM image of a PTCDA island recorded with a CO-functionalized tip (setpoint: 2.8 pA, 50 mV, z-offset: 1.85 Å). **c** Model of the island structure and adsorption geometry of PTCDA on NaCl. C (gray), O (red), H (white), Na^+ (purple), Cl^- (green).

Figure 5.7b shows an AFM image of another PTCDA island reocrded with a CO-functionalized tip. In such AFM images of PTCDA on NaCl, typically, only the perylene unit is visible. This was also seen for individual PTCDA on NaCl by Mohn et al., who attributed this to a non-flat adsorption of PTCDA with the anhydride groups being bent towards the surface [159]. Further, previous studies reported that PTCDA is centered above Cl^- such that the two outer oxygens of the PTCDA anhydride groups are well aligned with the position of Na^+ ions of the topmost NaCl layer [148, 159, 160].

From this image, it can be concluded that PTCDA molecules assemble in a brick-wall $c(4 \times 4)$ superstructure as visualized in the adsorption geometry model in Fig. 5.7c. According to first principle calculations by Aldahhak, Schmidt, and Rauls, the observed brick-wall growth mode should be favorable for PTCDA/NaCl [160]. In total, four preparations under comparable conditions always showed this brick-wall type assembly. In contrast, an experimental AFM study by Burke et al. reports on different growth modes of PTCDA on bulk NaCl [141].

5.5 NaCl-induced reduction of the sample work function

In the measurements of self-assembled PTCDA/NaCl/Au(110), which will be presented in the following chapters, we recognized that the voltage necessary to compensate the contact potential difference V_{CPD} indicated a large negative value in the range of -1 V. A large negative V_{CPD} suggests that the work function of the tip is significantly larger than the work function of the substrate.

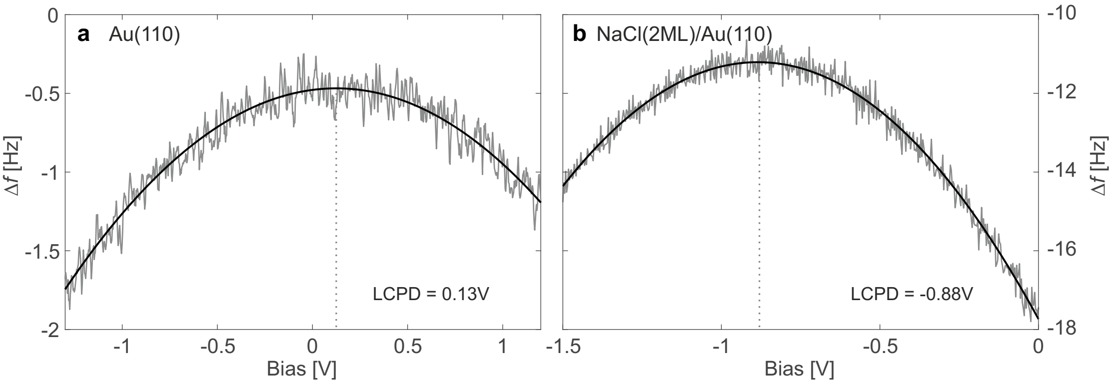

Figure 5.8: **a** $\Delta f(V)$ spectra on a clean Au(110) surface. **b** $\Delta f(V)$ spectra recorded in an area with, on average, two monolayer thick NaCl film grown on Au(110). (amplitude: 0.5 Å, z-offset: 0 Å **a**, 3 Å **b**; setpoint: 1.4 pA, 1.5 V)

To clarify whether this effect is attributed to the presence of PTCDA the V_{CPD} was determined on a clean Au(110) surface and compared to the V_{CPD} measured for clean NaCl/Au(110), which is shown in Fig. 5.8. From parabolic curve fits, we obtain $V_{\mathrm{CPD}}^{\mathrm{Au}} = 0.13\,\mathrm{V}$ for the bare Au(110) surface and $V_{\mathrm{CPD}}^{\mathrm{NaCl}} = -0.88\,\mathrm{V}$ for the Au(110) surface covered with a two monolayers thick NaCl film. This reveals that the NaCl film causes a reduction of the substrate work function on the order of 1 eV, which was reported for NaCl/Cu(111) by Bennewitz and colleagues [85]. Further, this shows that the large negative V_{CPD} values are not related to the presence of PTCDA, but primarily caused by the NaCl layer. However, it is conceivable that the presence of PTCDA might also cause a slight V_{CPD} shift.

6 Probing the electron distribution and electron transfer in charged self-assembled PTCDA islands

The results presented in this chapter have been acquired and interpreted in collaboration with Laerte Patera and Jascha Repp, and were published in Nano Letters [161][1]. *Parts of the text and figures are identical to the publication. Jascha Repp developed the code for the electrostatic model.*

In this chapter, AFM experiments on charging and probing the distributions of excess electrons within highly-ordered, electrically-isolated molecular islands are presented. Making use of self-assembly, molecular structures with atomic-scale order consisting of few molecules were grown on a NaCl layer, which was thick enough to suppress any charge transfer to the conductive substrate. By tuning the bias voltage applied between tip and sample, the charge state of the self-assembled clusters can be manipulated with single-electron control.
We found that, depending on the charge state, stable electron distributions or intra-island electron hopping are observed. This intermolecular charge transfer is driven by a local tip effect. A model allowed to reproduce the observed contrast features and hence, to clarify the charge-transfer pathways in the tunnel-coupled molecular structure. Further, we estimated the tunneling rates of the intra-island charge transfer based on the experimental frequency-shift and dissipation signal.

---

[1] P. Scheuerer, L. L. Patera, and J. Repp, *Manipulating and Probing the Distribution of Excess Electrons in an Electrically Isolated Self-Assembled Molecular Structure.* Nano Letters, **20**, 1839-1845 (2020)

6.1 Introduction

Conduction in molecule-based materials and structures arises from a hopping of charges between localized states, commonly referred to as hopping conduction [91–93]. The corresponding charge transfer rates and hence the conductivity strongly depend on the magnitude of reorganization energy and tunnel coupling between adjacent molecules [47, 60, 91, 92]. The investigation of such charge transfer processes within self-assembled confined molecular structures could provide insight into the influence of polaronic effects on the transfer rate, and how the distribution of charges within such structures could be affected by mutual charge interactions.

Further, a deeper understanding of charge transfer is important for engineering possible future devices for information storage and processing, based on individual atoms [7, 162], molecules [163, 164], atomic-scale logic gates [165], transistors [100, 166], and memories [167].

The effect of mutual charge interactions within confined structures is essential for the stability and realization of field-coupled cells, such as quantum cellular automata (QCA), which offer a possibility to reduce power consumption compared to conventional current-based semiconductor electronics [168, 169].

In 2009, Haider et al. made an important step towards the realization of field-based electronics at the atomic scale [170]. By STM manipulation, they created Si dangling bonds, which act as hosts for localized excess electrons, on a hydrogen-terminated silicon surface. They demonstrated that the charge distribution and occupation within tunnel-coupled dangling bond structures can be steered by electrostatic interactions [170]. In the same work group, Huff et al. recently reported on logic devices based on tunnel-coupled dangling bond structures [171], and Rashidi et al. demonstrated controllable charge-state switching and readout of weakly-coupled dangling-bond structures by means of AFM [116]. Even though these dangling bonds are created on a semiconducting surface, their states can be considered as electrically decoupled since they lie within the band gap of silicon.

Kocic et al. presented an alternative approach to realize field-based electronics by patterning self-assembled molecular structures with STM manipulation [145]. However, these functional cells are implemented in a molecular film grown on a conductive substrate and hence are not electrically isolated. This drawback can be overcome by making use of the decoupling properties of insulating films, which also suppress charge transfer to the conductive substrate at sufficient layer thickness [14, 31].

With regard to this, it is noteworthy that Steurer and colleagues investigated charging of individual tunnel-coupled pentacene molecules in an insulating environment [14]. By means of AFM $\Delta f(V)$ spectroscopy, they could track and manipulate the charge state of tunnel-coupled pentacene molecules and, moreover, identify lateral charge transfer events between adjacent pentacene molecules [14]. Further, Rahe and coworkers demonstrated controlled multiple charging of large self-assembled molecular islands with single-electron control at room temperature on an insulating calcite substrate [15]. Those experiments shed light on the charge transfer between tunnel-

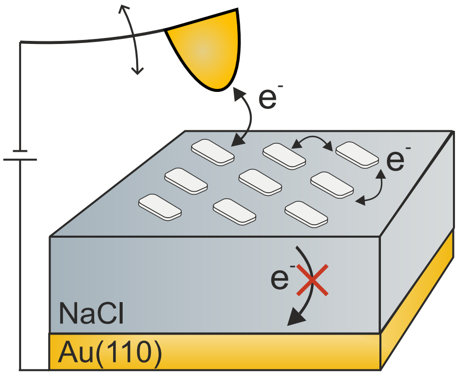

Figure 6.1: Schematic picture of the experiment showing a molecular island consisting of few molecules. Charge transfer to the conductive substrate is suppressed due to the thick NaCl film. The charge state of the island can be controlled by the applied bias voltage.

coupled molecules and molecular structures, even the role of Coulomb repulsion in charging adjacent molecules was investigated. Whereas in the experiments by Steurer et al. were limited to a few molecules, which are randomly arranged at the surface [14], in the studies by Rahe and colleagues, only the total charge state is accessible but the localization of charges within an island remained elusive [15].

The experiments that will be presented in this chapter continue at this point. We investigate multiple charging with single-electron control in highly-ordered tunnel-coupled molecular islands consisting of a few molecules, with a resolution at the single-molecule scale. To this end, we grew self-assembled islands of perylene-3,4,9,10-tetracarboxylic dianhydride (PTCDA) molecules on an insulating NaCl surface, which was thick enough to suppress charge transfer to the supporting conductive Au substrate (see Fig. 6.1 for a schematic of the experiment). By means of AFM, we characterized the voltage thresholds required to inject and remove individual charges, including their dependence on the tip position. Furthermore, by imaging the island in different charge states, we could drive and track intermolecular electron hopping. This allowed us to shed light on the localization and stability of charge distributions and how they depend on the charge state.

6.2 Sample preparation and methods

For the experiments shown in this chapter, a Au(110) single crystal was used as a supporting conductive substrate. An atomically flat, clean metal surface was prepared according to the procedure described in chapter 3. Subsequently, a NaCl layer of, on average, 22 monolayers thickness has been grown with the sample temperature held at 160° C. One half of the Au single crystal was screened by a mask during NaCl deposition, to maintain a clean Au surface for tip preparation. The molecules were sublimed in-situ from a Si wafer onto the $\approx 7\,\mathrm{K}$ cold sample surface. Finally, the sample was heated to 320 K for two minutes to initiate self-assembly and then cooled down to 7 K again. Sharp tips were prepared by repeated indentations into the clean Au substrate. The tip was considered to be suitable for imaging when both, STM and AFM images indicated a sharp symmetric tip and a $\Delta f < 5$ Hz was measured while operating in constant-current STM mode (set-point $\mathrm{V} \approx 0.5\,\mathrm{V}$, $\mathrm{I} \approx 1\,\mathrm{pA}$). The thick NaCl layer prohibits STM operation. Hence, we used AFM for imaging, which was operated either in constant-Δf feedback mode or in constant-height mode. The z-offsets, which are given for constant-height images, refer to the constant-Δf set-point and positive values indicate a displacement away from the surface.
In order to approach the tip on an insulator surface, special care has to be taken to avoid unintended crashing of the tip into the substrate. Therefore, relatively large cantilever oscillation amplitudes $A = 2 - 4\,\text{Å}$ were used for approaching. Since sharp tips do have a small contribution of attractive background forces the total Δf signal, the approach interruption Δf-limit has to be set to values <5 Hz. Further, the bias voltage was set to $> 2\,\mathrm{V}$ to increase long-range electrostatic contributions to the frequency shift. All three parameters generate a setpoint with large tip-sample distance and hence reduce the risk of tip crashes.

6.3 Geometrical structure of self-assembled PTCDA islands

Figure 6.2a shows a constant-Δf image of the NaCl surface after the self-assembly process, revealing the formation of small molecular islands. A high-resolution image of the island, marked with a square, reveals nine PTCDA molecules assembled in brick-wall 3-by-3 configuration (Fig. 6.2b). This adsorption geometry is in line with an AFM image of a self-assembled PTCDA island on NaCl(2ML)/Au(110) recorded with CO tip, revealing the intramolecular structures and the relative arrangement within the island (see Fig. 6.2c, the figure shows only a part of a larger island). This arrangement corresponds to a c(4×4)-superstructure of molecules with respect to the NaCl(100) surface [160], where PTCDA is centered above Cl^- ions and the anhydride oxygens are almost in registry with the Na^+ ions of the substrate [141, 148, 159]. For more details, it is referred to the previous chapter.

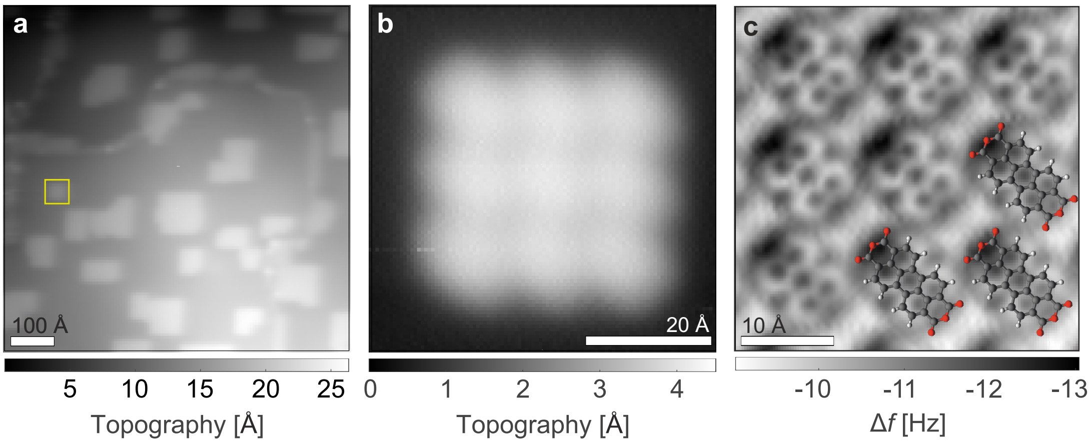

Figure 6.2: **a** Constant-Δf image of self-assembled PTCDA molecules on NaCl(22ML)/Au(110). **b** High-resolution image of the island marked with a square in **a**. **c** Zoom-in of an AFM image of a large self-assembled PTCDA island on NaCl(2ML)/Au(110) recorded with CO-tip.(setpoint: 1 mV, -1.0 Hz(a), -1.6 Hz(b), amplitude: 2 Å; setpoint: 2.8 pA, 50 mV, z-offset: 1.85 Å, amplitude: 0.5 Å(c))

6.4 Determination of the charge state of PTCDA on NaCl(22ML)

Due to the large electron affinity of PTCDA (4.6 eV) [172], which is comparable to the work function of the substrate ($\Phi_{Au(110)} = 5.4\,\text{eV}$[154][2]) its charge state on NaCl is not a-priori clear. Alternate-charging scanning tunneling microscopy (AC-STM), opens up the possibility to investigate the orbitals of molecules, adsorbed on insulating materials, by periodic charging and discharging synchronized with the cantilever motion [36, 62]. We made use of this technique to derive the charge state of PTCDA on thick insulating films by determining the energetic alignment of molecular orbitals with respect to the tip's Fermi level.

For these experiments, individual PTCDA molecules were deposited on a 20 monolayer thick NaCl film grown on a Au(110) substrate under the same conditions as in the self-assembled PTCDA island experiments. Figure 6.3 shows two $\Delta f(V)$ spectra of an individual PTCDA molecule, where abrupt Δf changes indicate charge-state transitions [11, 14]. In total, three charge-state transitions could be accessed, occurring around $\simeq$ -3.6 V, $\simeq$ 0.8 V and $\simeq$ 2.3 V. An AC-STM image corresponding to the charge transition at negative bias voltage reveals a contrast that is attributed to the HOMO of PTCDA [158]. Instead, the contrast of the two AC-STM images

---

[2] In fact, the NaCl film is expected cause a reduction of the sample work function on the order of 1 eV [85]. This is in line with the observed large VCPD shift for NaCl/Au(110) compared to Au(110), as discussed in the previous chapter and hence gives rise to a sample work function being comparable to the electron affinity of PTCDA.

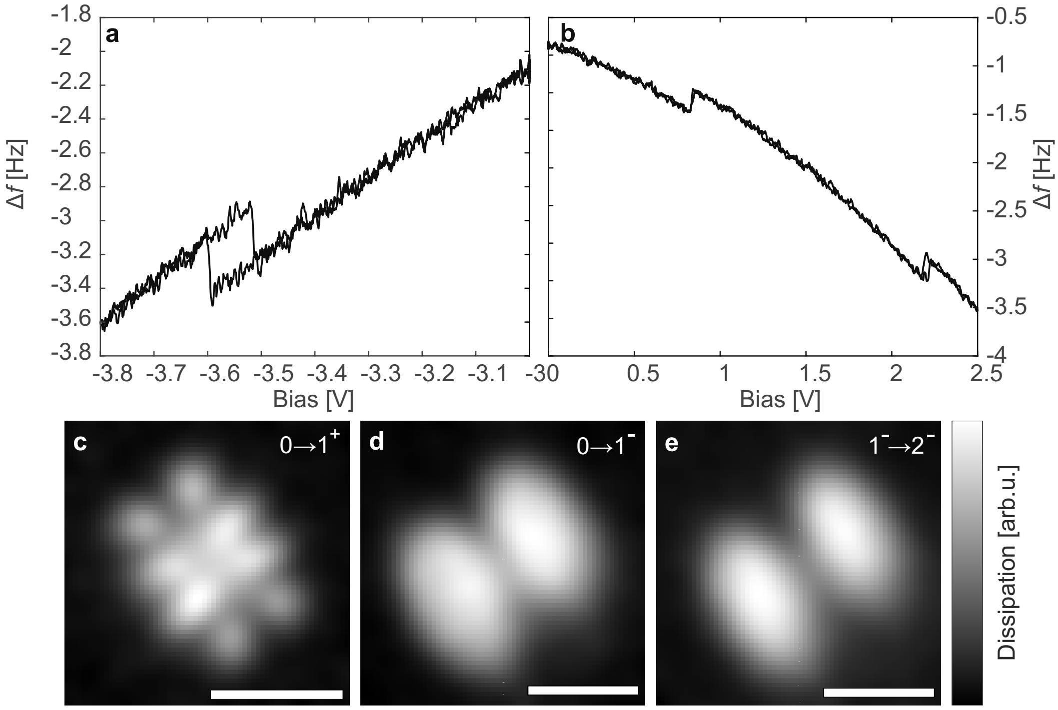

Figure 6.3: $\Delta f(V)$-spectra of the first charge state transition at negative bias **a** and two transitions at positive bias voltage **b**. Corresponding AC-STM images of the $0 \rightarrow 1^+$ **c**, $0 \rightarrow 1^-$ **d** and $1^- \rightarrow 2^-$ **e** ($V_{AC} = 1.7\,V_{pp}$, $A = 1\,$Å, **c** V_{dc} = -3.67 V, setpoint: Δf = 0.7 Hz at V = 0 V, z-offset: 0 Å), **d** V_{dc} = 0.91 V, setpoint: Δf = -1.5 Hz at V = 0 V, z-offset: 2.4 Å, **e** V_{dc} = 2.40 V, setpoint: Δf = -1.5 Hz at V = 0 V, z-offset: 1.0 Å

corresponding to the charge state transitions at positive bias voltage has close resemblance to the LUMO of PTCDA (Figs. 6.3c,d). Due to their similar appearance, both transitions are attributed to the LUMO. The voltage difference of $\approx 1.5\,$V is related to the electrostatic energy that is required for adding a further electron [82, 99, 157]. Based on these observations, we infer that PTCDA is neutral at $V = 0\,$V and that the first step in the Δf spectrum at positive bias voltage is attributed to the injection of an excess electron into the island. Accordingly, the shown images correspond to the $0 \rightarrow 1^+$ (HOMO), the $0 \rightarrow 1^-$ and $1^- \rightarrow 2^-$ (both LUMO) transitions.

6.5 Controlled charging and charge-state detection of a self-assembled PTCDA island

In order to achieve multiple charging and sense the corresponding charge state transitions, we acquired a $\Delta f(V)$ spectrum at the center of the 3-by-3 island from Fig. 6.2b, which is shown in Fig. 6.4. This $\Delta f(V)$ spectrum shows a series of distinct jumps in Δf while increasing the bias voltage up to 3 V (blue) and downward shifts when sweeping the bias voltage back to 0 V (orange), which can be regarded as signatures of charge state transitions [11, 31, 60]. Further, it can be seen that those charge transitions exhibit a hysteresis, which may result from the reorganization energy due to structural relaxations of a molecule and the substrate that stabilize an excess charge [14, 60]. For the following results, only voltages < 2 V are relevant. Bearing in mind that doubly charging of the LUMO required an ≈ 1.5 V larger voltage for single molecules, we can rule out doubly charging of a molecule within the island.

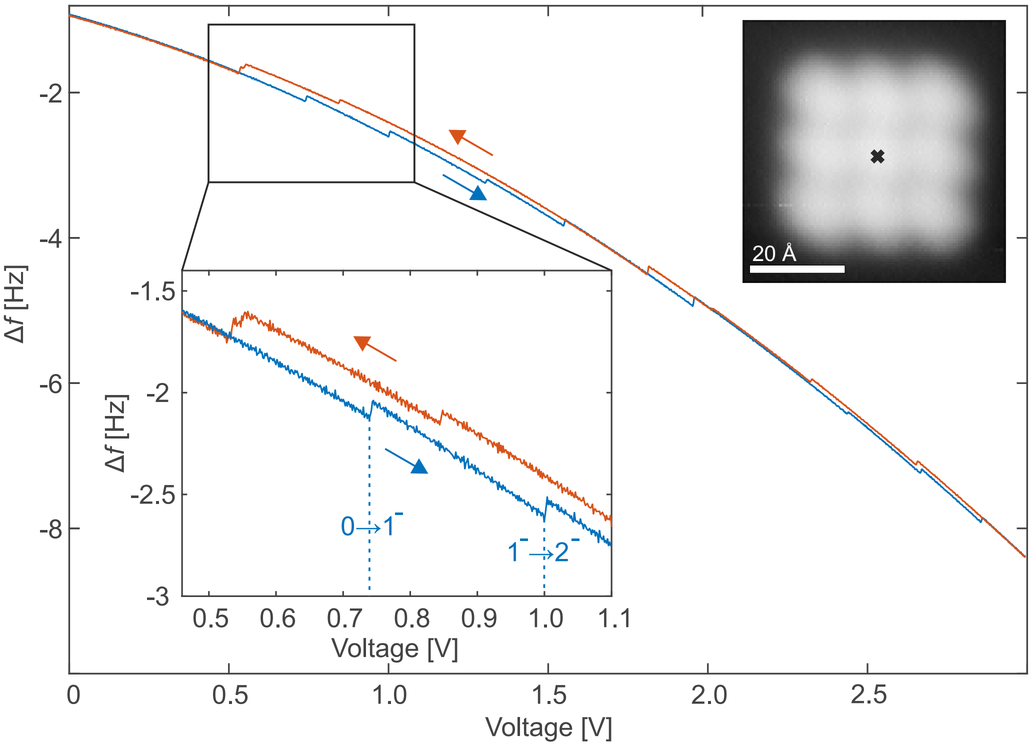

Figure 6.4: $\Delta f(V)$-spectrum, recorded at the center of the 3-by-3 PTCDA island. Forward (backward-) curve is shown in blue (orange). Insets: zoom-in of the spectrum, where the injection of the first and second excess electron is highlighted (setpoint: 1 mV, -1.6 Hz, z-offset: 7.5 Å, Amplitude: 2 Å)

6.6 Spatial dependence of the charging with one excess electron

Even though it will be shown later that all steps in Δf are indeed attributed to the injection (removal) of charges into (from) an island, the small intermolecular distances in those self-assembled structures allow for a lateral charge transfer between molecules within the island. Hence, some of the observed steps could also be signatures of lateral charge transfer, as observed by Steurer et al. for tunnel-coupled pentacene molecules [14]. However, the first charging event can be clearly attributed to the injection of a single electron into the PTCDA island. For this reason, only the first charging event was investigated for different spatial positions of the 3-by-3 island as a next step.

To this end, we acquired $\Delta f(V)$ spectra at various spatial positions of the island and kept the bias voltage below 0.8 V to ensure that only one excess electron is injected into the island. Figure 6.5a shows three representative $\Delta f(V)$ spectra that were recorded at different spatial positions of the island. The positions at which the spectra were acquired are indicated with colored dots in the AFM image in Fig. 6.5b, where different colors are used to distinguish between different sites, namely

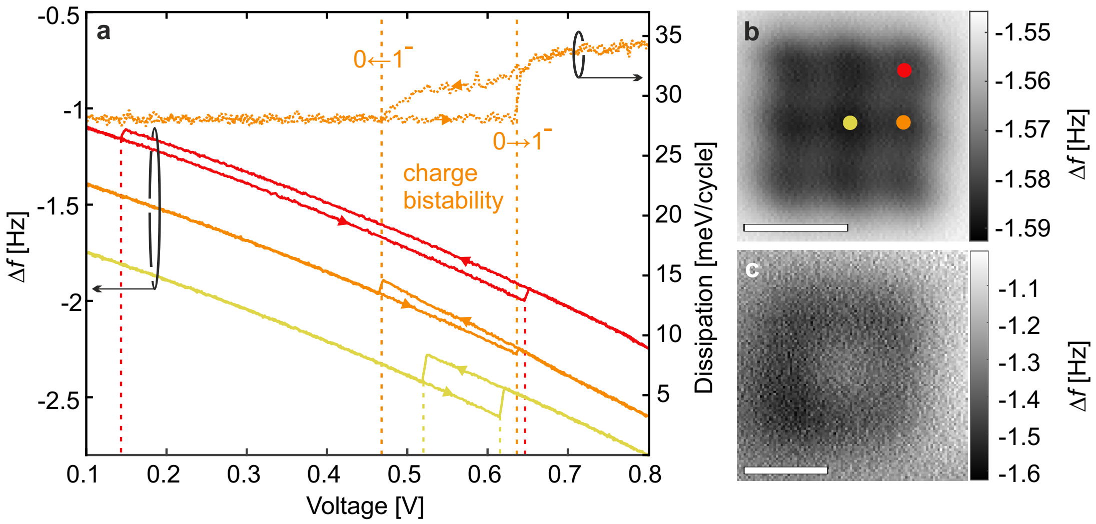

Figure 6.5: **a** $\Delta f(V)$-spectra of the charging with one excess electron at different spatial positions. The $\Delta f(V)$-spectra are vertically shifted for clarity (z-offset: 7.0 Å). The vertical dashed lines highlight the charge-state transitions in all spectra. **b** AFM image of the 3-by-3 island (z-offset: 3.4Å). Colored dots indicate the position of the spectra shown in **a**. **c** AFM image of the same island being singly negatively charged recorded with at very large tip-sample separation ($V = 0.6$ V, z-offset: 12Å). (setpoint: Δf = -1.6 Hz at V = 0 V, Amplitude: 2 Å).

center, edge, and corner sites. Those sites are different regarding their number of next neighbors. The center molecule has eight, edge molecules five and corner molecules three neighbors, respectively.

In those spectra, a sudden step in Δf indicates the injection of an electron and a drop in Δf the removal. For all spectra the charge state transition exhibits a clear hysteresis - the voltage for electron removal is lower than the voltage for electron injection - due to reorganization energy [14, 60].

Notably, the width of the hysteresis is quite different for the three different positions. The spectrum acquired above the center molecule reveals a small hysteresis around $V \approx 0.57\,\mathrm{V}$, having a width of $\approx 0.10\,\mathrm{V}$. The hysteresis becomes substantially wider for $\Delta f(V)$ spectra recorded above the edge and corner molecules. Compared to the center position, the voltage required for removing the electron is lowered by $\approx 0.1\,\mathrm{V}$ at the edge position, and further lowered by $\approx 0.3\,\mathrm{V}$ at the corner position.

The voltages for electron injection are similar but increase slightly from center to edge to corner. It is noteworthy that the voltage thresholds for charging and discharging are subject to stochastic fluctuations [60]. However, other spectra measured under comparable conditions are in line with these trends.

Figure 6.5c shows an AFM image of the same PTCDA island being singly negatively charged, recorded at much larger tip-sample distance to minimize the influence of the tip on the charged island. This image reveals a distinct contrast at the center of the island indicating that the excess charge is localized at the center molecule, which can be rationalized as follows: the center, edge, and corner PTCDA molecules differ by their number of neighboring molecules, which leads to a site-dependent charge screening – being largest at the center – and thereby causes small differences in electron affinities that favor the occupation of the central molecule with a single excess electron. Such polarization effects were reported for PTCDA clusters by Cochrane et al. [148]. Further, the preferential occupation of the central molecule is in line with dI/dV measurements of a self-assembled PTCDA island on a bilayer of NaCl shown in the next chapter (see chapter 7, Fig. 7.5).

Accordingly, the small difference for the electron injection can be explained by a reduced electron affinity from center to edge to corner due to a reduced screening. Once an electron is injected at any site, it tunnels to the most favorable center position. Therefore, an electron can be removed easiest at the center position in line with the small hysteresis width.

However, with the tip being positioned at an edge or corner site, a much smaller voltage is needed to remove the electron due to the larger distance to the tip, which agrees well with the significant shift of the discharging transitions to smaller bias voltages at edge and corner sites.

Notably, at some positions, the charging does not only induce a change in the $\Delta f(V)$ signal but is accompanied by a sudden increase in the AFM dissipation signal. This is the case in the spectrum at the edge position in Fig. 2a, for which additionally the voltage-dependent dissipation is plotted. From comparison to the corresponding Δf signal, it becomes clear that the dissipation starts to increase as soon as an electron is injected and only recovers once the island is neutralized.

In frequency-modulation AFM such an additional dissipation, for example, can arise from fluctuations of the charge state (causing fluctuations of the measured electrostatic force) coupled to the oscillatory motion of the cantilever [36, 42, 44, 46, 173, 174]. To significantly dissipate the cantilever, this charging and discharging has to occur with a time delay on the order of the cantilever oscillation period ($T \approx 34\mu$s), thereby causing a hysteresis in the force-distance dependence of the vertical cantilever motion. In the case of instantaneous charge transfer, there would be no hysteresis in the force-distance dependence of the cantilever motion. In contrast, if the tunneling occurred at much lower rates, the dissipation would also decrease due to a reduced probability of charge transfer events per oscillation cycle.

As mentioned at the beginning of this chapter, there are two possible charge transfer mechanisms, namely, intra-island (intermolecular) and tip-island charge transfer. The tip-island charge transfer occurs on the order of seconds and leads to discrete steps in the Δf channel. We estimate tip-island distance to be about 10 Å in our experiments [36]. Instead, the carbon atoms of adjacent PTCDA molecules, which are involved in the formation of the delocalized frontier orbitals, can be as close as 4 Å. Hence, intra-island charge transfer is expected to occur orders of magnitude faster due to a much larger tunnel coupling between adjacent molecules.

Accordingly, the discrete Δf steps are attributed to tip-island charge transfer and the dissipation to intra-island (intermolecular) charge transfer. This interpretation is supported by the fact that the excess dissipation only occurs after injection of an excess electron into the island.

With this reasoning, the multiple charging spectrum from Fig. 6.4 can be discussed in more detail. In total, eight steps due to charging can be recognized, but only seven steps due to discharging. Above ≈ 1.7 V there are four steps in the forward as well as the backward spectra. Further, the forward and backward Δf curves overlap below 0.5 V and between $V \approx 1.55...1.75$ V (attributed to $N = 0$ and $N = 4$ excess electrons, respectively), from which we infer that the hidden transition has to occur between 0.5 and 1.55 V.

Figure 6.6 shows a detailed analysis of this voltage range (spectrum 1) and for a subsequently recorded spectrum (spectrum 2). Additionally, parabolic curves are plotted to allow for assigning distinct regions of the curves to a specific charge state. Those two spectra experience good overlap, which highlights the reproducibility of the experiment. Apparently, the Δf signal deviates from the parabolic curve in the forward directions for $N = 1$. We attribute this to the simultaneous occurrence of dissipation due to intra-island charge transfer.

Further, it becomes clear that in both cases, the $3^- \rightarrow 2^-$, $2^- \rightarrow 1^-$, and $1^- \rightarrow 0$ almost fall together and the 3^- state can even be stable in a voltage range, where the island initially is neutral. This behavior can be rationalized as follows: due to repulsive Coulomb interactions, all electrons will be localized at edge or corner sites for $N > 1$ [14]. Hence, with the tip positioned at the center of the island, the discharging transitions will be shifted to significantly lower voltages due to the weaker

tunnel coupling of the tip to the edge and corner positions. The fact that the removal of the third and second excess charges fall together, can not be explained with this simple reasoning. It probably originates from an interplay of Coulomb repulsion and rearrangement of excess charges upon removal of the third excess electron.
However, the last electron will be relocated at the center, where it can easily be removed and hence its subsequent immediate removal is conceivable.

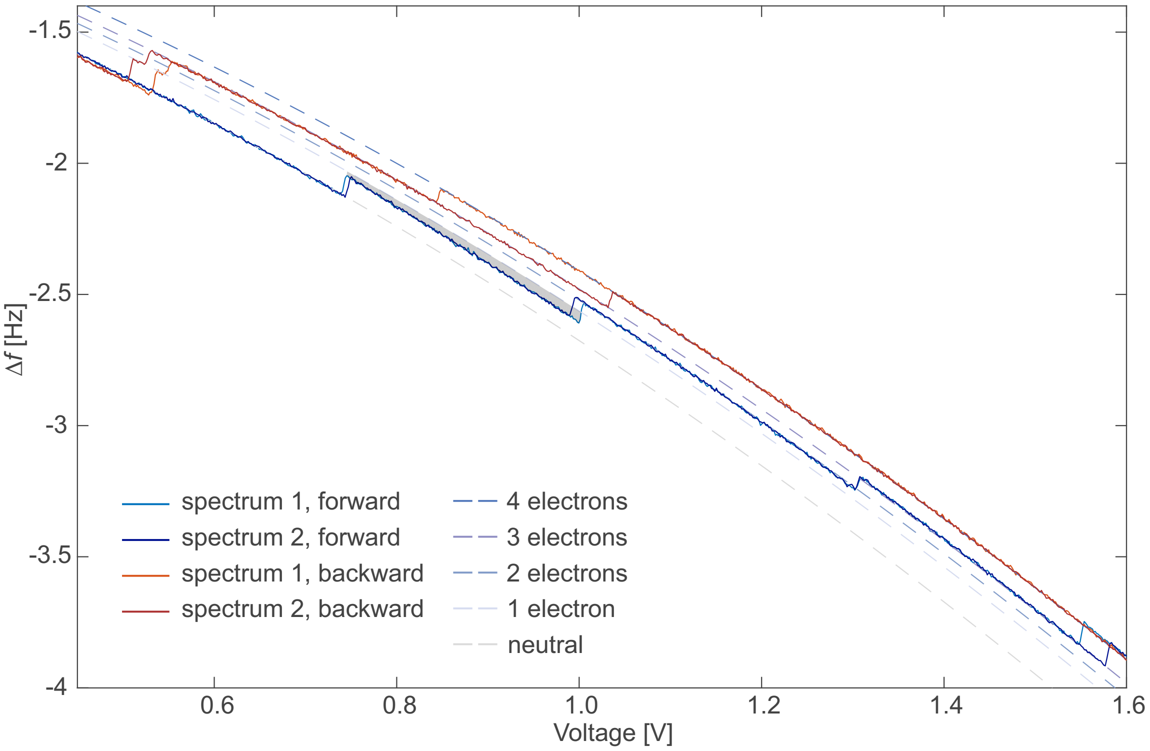

Figure 6.6: Two subsequently recorded $\Delta f(V)$-spectra at the center of the 3-by-3 PTCDA island. The dashed curves indicate Kelvin parabolas of distinct charge states. The curve of the neutral state was obtained from a parabolic curve fit of the neutral section of the Δf spectra. All other curves are horizontally offset with respect to the neutral curve. The gray area highlights the deviation of Δf spectra from the parabolic $N = 1$ curve. (setpoint: 1 mV, -1.6 Hz, z-offset: 7.5 Å, Amplitude: 2 Å)

6.7 AFM images at different bias voltages

To get a deeper insight into the spatial dependence of the dissipation and the role of the charge state, a set of Δf- and dissipation images of the 3-by-3 island at different bias voltages was acquired, which is shown in Fig. 6.7.
After each pair of Δf- and dissipation images, the bias voltage was increased by 50 mV in order to successively increase the number of excess electrons within the island. In total, five distinct contrast regimes can be observed, which are highlighted in the figure by different background colors. The voltages corresponding to the transitions between different contrast regimes roughly agree with the steps observed in the forward curve of the spectrum in Fig. 6.4. Hence, we conclude that those regimes are attributed to different charge states of the island.

For a more detailed discussion of the observed contrast features, selected images of the neutral, singly, doubly, and four times negatively charged island are shown in Fig. 6.8.
In the neutral state ($V = 0.45\,\mathrm{V}$), the Δf image shows an attractive homogeneous background, and the dissipation channel is completely featureless.
When being singly charged ($V = 0.65\,\mathrm{V}$), four circular features located at the positions of the edge molecules appear in both channels.
At $V = 1.05\,\mathrm{V}$, the island is doubly negatively charged and the Δf and dissipation image show two ribbon-like features at opposing corners of the island.
Obviously, the spatial dissipation features are not perfectly symmetric with respect to the shape of the island. For example, in the images of the singly-charged island, two of the circular features appear as disks, whereas the other two have a ring shape. Furthermore, in the case of two excess electrons, one ribbon appears more pronounced. As will become clear later, we attribute those asymmetries to an inhomogeneity of the island's environment or the tip shape. Further, those rings and disks appear to have a faint internal structure.
Notably, at $V = 1.50\,\mathrm{V}$, where the island is four-times negatively charged, no spatial dissipation features can be observed. From the distinct (less attractive) contrast at the corner molecules in the Δf image, we conclude that the four excess charges are stably localized at the corner molecules. In this configuration, the distance between excess charges is maximized, and hence the Coulomb interaction is minimized. This observation highlights the role of the total charge state in the distribution of excess electrons within the island.

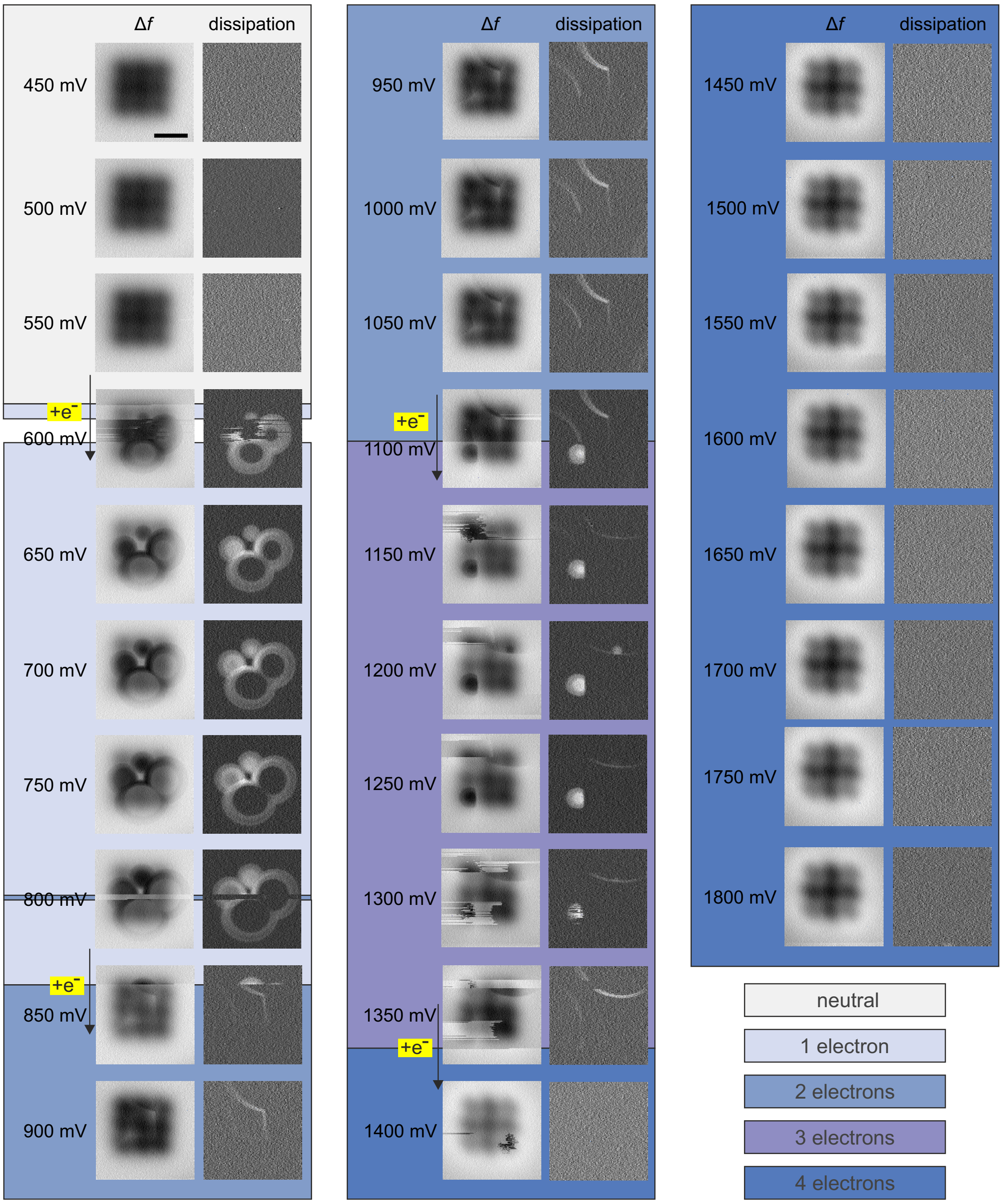

Figure 6.7: Set of constant-height AFM images of a 3-by-3 PTCDA island at different bias voltages (Δf- (left) and dissipation channel (right) in each column). Charge state transitions are marked with arrows and regimes of equal charge state have the same background color. Colorbars are omitted for clarity. The scale bar corresponds to 20 Å. (Set-point: Δf = -1.3 Hz at V = 0 V, Amplitude: 1 Å, z-offset: 3 Å.)

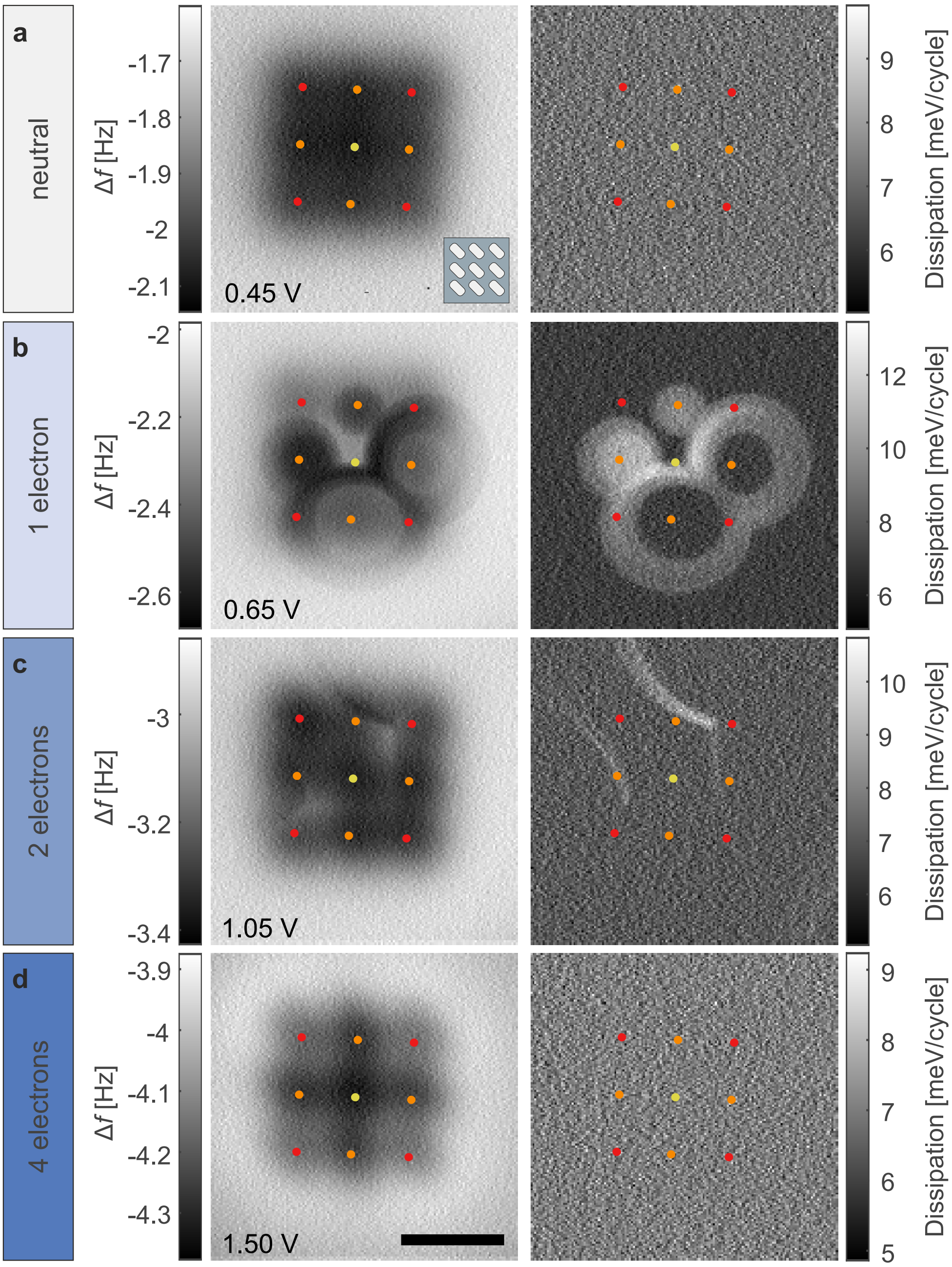

Figure 6.8: Constant-height AFM images (left column) and the corresponding dissipation signal (right column) of the 3-by-3 PTCDA island in different charge states. In all the images the positions of the individual molecules are marked with colored dots. Center (yellow), edge (orange) and corner molecules (red). **a** $V = 0.45\,\mathrm{V}$, **b** $V = 0.65\,\mathrm{V}$, **c** $V = 1.05\,\mathrm{V}$ and **d** $V = 1.50\,\mathrm{V}$. The scale bar corresponds to 20 Å. (Set-point: Δf = -1.3 Hz at $V = 0\,\mathrm{V}$, Amplitude: 1 Å, z-offset: 3 Å.)

6.8 Origin of the dissipation signatures

In the following, we will give an explanation for the observed dissipation based on the example of a single excess electron within the island, taking into account the tip. As discussed above, the excess electron should be localized at the center of the island due to screening effects [148]. Accordingly, the second-best configuration would correspond to an excess electron being localized at an edge molecule, whereas a localization at a corner molecule should be least favorable.

The observation of four circular features around the edge molecules can then be rationalized as follows: the presence of the tip locally influences the electron affinities of the molecules with respect to each other. For specific tip positions, this could favor the localization of an excess electron at another molecule. Since these tip-induced energy shifts also depend on the tip-molecule distance, the cantilever oscillation periodically changes this energy balance, such that the electron hopping becomes synchronized with the cantilever motion.

This is visualized in Fig. 6.9 for the tip positioned above an edge molecule. At small tip heights (close to the lower turnaround point), the excess charge is transferred from the center to an energetically more favorable edge site. At larger tip heights (close to the upper turnaround point), the tip influence is too weak, which causes a transfer of the excess electron back to the center molecule. Hence, the level alignment is inverted twice during a cantilever oscillation cycle and thereby causes an electron to tunnel between the center and an edge molecule, synchronized with the cantilever motion.

In order to obtain significant dissipation from such an intermolecular charge transfer, tunneling forth and back has to occur at different tip heights, causing a hysteresis in the force-distance relation. Such a retarded force variation can arise from the finite tunneling rate of the intra-island tunneling process, on the order of the cantilever oscillation frequency [42, 44–46, 173, 174]. Additionally, the tunneling rates might be

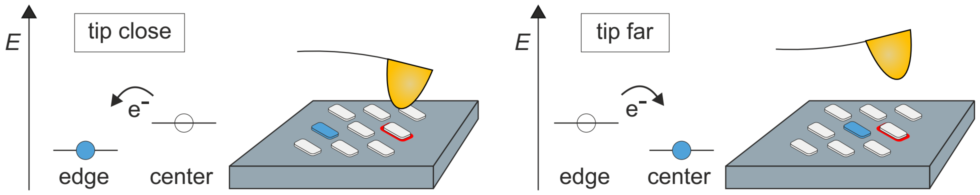

Figure 6.9: Schematic picture of tip-induced level alignment and the corresponding charge configurations for the tip positioned above an edge molecule. **a** For large tip-molecule distances the tip-induced level shift is only weak and the excess electron is localized at the center molecule. **b** For small tip heights the tip influence changes the relative level alignment such that the excess charge is preferentially occupying the edge molecule away from the tip. The molecule, above which the tip is positioned, is highlighted in red.

significantly lowered by polaronic-shifts resulting from structural relaxations upon charge transfer [14, 60, 116].
In experiments, one would expect that the symmetry of the island is also reflected in the dissipation pattern, which is obviously not the case. As will be shown later, such an asymmetry could originate from a tilt in the potential background of the island due to other close-by islands or step edges in the NaCl, for example.

6.9 Possible mechanisms for tip-induced energy level shifts

As discussed above, the dissipation patterns suggest that the tip can induce lateral hopping of electrons within an island by locally shifting the energy levels of the molecules with respect to each other. There are three different possible mechanisms that could cause such tip-induced level shifts.
The voltage drop in the NaCl layer can cause significant level shifts, being in the range of 30 % of the applied bias voltage [14, 60]. However, from the schematic picture in Fig. 6.9, it becomes evident that only the relative level alignment of different molecules is important for the lateral charge transfer, whereas a constant shift would not lead to intra-island electron hopping. Assuming a tip radius being on the order of 100 Å [60, 112], this voltage drop is expected to be rather non-local, thereby shifting all the levels in a similar way.
Additionally, two other effects could locally affect the relative level alignment within the island, namely the screening from the tip or the local electric field of the tip. For example, the presence of a local dipole at the tip apex due to the Smoluchowski effect [175–179] with the dipole vector pointing towards the surface could lead to a lowering of a molecular state beneath the tip, with strong lateral confinement.

To clarify whether the dominating tip influence is attractive or repulsive, we analyzed

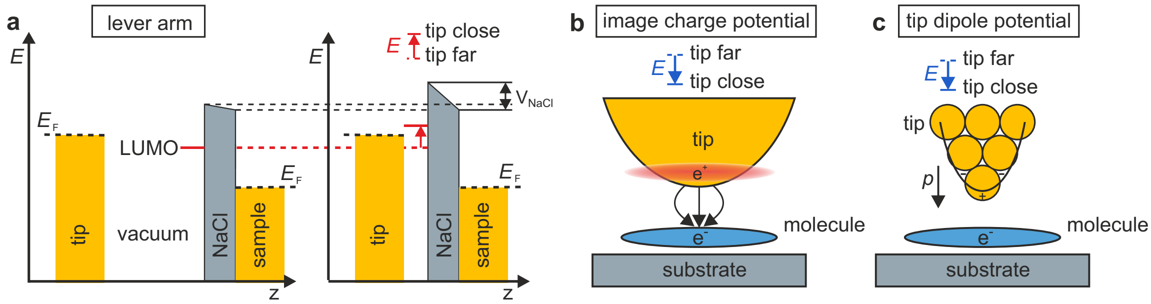

Figure 6.10: **a** Tip-height dependent voltage drop over the NaCl layer V_{NaCl}, depending on the ratio of the vacuum gap z_{vac} and the thickness of the NaCl layer [60]. **b** Image charge potential for an image charge in the tip. **c** Local dipole at the tip apex. Panel **c** was adapted from [175].

the image contrast for one and two excess electrons in more detail. To this end, the Δf signal attributed to lateral charge transfer was canceled out by subtracting the excess dissipation signal, which was converted into units of Hz according to reference [42](see Fig. 6.11). In general, the injection of an electron into the island causes an increase in the measured Δf signal at a given bias voltage, which is recognized as an upward step in charging spectra. Consequently, in these images, a stable localization of the electron beneath the tip should lead to a brighter Δf contrast. The image of the singly charged island reveals that the ground-state charge configuration corresponds to an electron localized at the center of the island in presence of the tip. In fact, this can also be seen in the Δf image in Fig. 6.8b. In all image regions that are connected to the outside of the island without crossing any sections in which dissipation occurs, the charge configuration should not be affected by the tip. Since the contrast is brighter at the center than at the top left corner, the charge can be localized at the center of the island.

Further, it becomes clear that the charge is rather pushed away by the tip than being attracted. Otherwise, one would expect an increased Δf signal inside the right and bottom rings in Fig. 6.11a.

The image of the doubly charged island (Fig. 6.11b) reveals that the charges are located at two corner sites in the ground state. Also, here, the observed contrast rather suggests a repulsive influence of the tip.

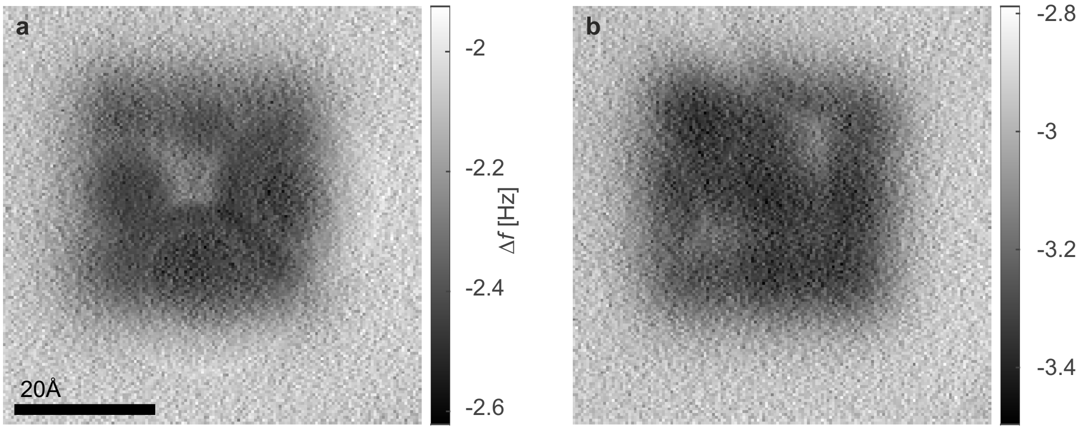

Figure 6.11: AFM images of the 3-by-3 island, hosting one **a** and two **b** excess electrons. To minimize the Δf signal due to lateral charge transfer the additional dissipation in units of Hz (see section 6.12) was multiplied by a scaling factor $s = 0.12$ and subtracted from the Δf image.

6.10 Electrostatic model of the energy level alignment

To verify the above interpretation of the dissipation, originating from tip-induced intra-island tunneling, the electron distribution in the island was modeled as a function of bias voltage (defining the chemical potential of the tip) [180] and position of the tip. Considering every molecule being either neutral or occupied with one excess electron gives rise to $2^9 = 512$ possible configurations. The energy of each configuration is calculated as $E = \sum_i n_i \epsilon_i + \sum_{i,j} n_i n_j V_{ij}$, where i, j are the indexes of the sites, n_i is the occupation operator, and ϵ_i are the LUMO energies with respect to tip's chemical potential, taking the relative voltage drop inside the NaCl film into account. The latter we estimate to be in the range of 30% [14, 60].

The unperturbed LUMO energy is extracted from the neutral to singly-negative charge-state transition of single-molecule experiments (Fig. 6.3). This energy is reduced by 152, 120, and 100 meV for center, edge, and corner molecules, respectively, due to screening effects. These site-dependent relative energetic differences were estimated from the observed increased voltage threshold for electron injection at edge and corner molecules compared to the center molecule and were fine-tuned such that the ground state of $N = 2$ corresponds to two electrons being localized at opposite corner sites, in agreement with the experiment. Further details on how the site-dependent energy difference had to be set will be given at the end of this section.

The pair-wise Coulomb repulsion between excess electrons at distance d_{ij} within the molecular island is given by $V_{ij} = 1/(4\pi\epsilon\epsilon_0 d_{ij})$. Here, the effective dielectric constant ϵ accounts for the screening due to the environment (substrate, NaCl film, tip and molecules). The value ϵ was derived based on the following consideration: The pair-wise Coulomb interaction from the mutual repulsion of the electrons dominates the energy separation of the sequential charging steps. On the scale of this energy spacing ($\approx 0.2\,\text{eV}$), the energy difference between the different sites, center, edge, and corner are minor. Therefore, the effective dielectric constant ϵ that accounts for the screening due to the environment can be reliably fit from this spacing such that the voltage difference between the $0 \rightarrow 1^-$ and the $3^- \rightarrow 4^-$ transitions matches the value of the experiment of $\approx 0.75\,\text{V}$. Taking the relative voltage drop inside the NaCl film of $\approx 30\,\%$ into account sets ϵ to 4.

With the fixed value of $\epsilon = 4$, the differences in electron affinities were chosen such that the energy gain of 46 meV from Coulomb repulsion favors the ground state configuration for $N = 2$ with two excess electrons in two opposing corners of the island compared to another configuration, in which the two electrons are located in two opposing edge molecules. This energy difference must be more than twice the difference in energies between edge and corner sites and thereby provides an upper bound for the latter. Conversely, the difference in threshold voltages for the injection of one excess electron at the center, edge and corner molecules (see Fig. 6.5a) shows that this energy difference should not be much smaller than 20 meV. Therefore, the energy difference between center and edge molecules was set to 32 meV and the one between edge and corner molecules to 20 meV in the simulation. These are the most important fit parameters and are set with a relative confidence interval of about 30 % based on the above considerations.

With these parameters, the energy levels in Fig. 6.12a were simulated. For the energy level diagram in Fig. 6.12b we additionally included the potential of the tip to locally shift the LUMO energies of the molecules with respect to each other. To this end, tip potential was modeled as a combination of an electric monopole and dipole located at the tip position. The tip height was assumed to be 10 Å above the molecular plane [36]. To fit the experimentally observed patterns, it had to be assumed that the tip's dipole field acting on the molecules directly, indirectly also affects all nearest neighbors. Hence, any energetic shift arising from the tip's dipole calculated for a certain molecule was assumed to also shift all neighbors of that molecule with a certain scaling factor. This may be rationalized by the interaction of neighboring molecules via the intermolecular O···H bridges. For the simulated spatial dependence of electron distributions in presence of the tip in Fig. 6.13, we further included a potential tilt of 3.5 mV/nm and an energy offset to lift the degeneracy of the four corners and to account for the asymmetries observed in experimental images.

The energies of possible electron distributions (or charge configurations) in a 3-by-3 PTCDA island for different numbers of excess electrons without local tip influence, which were obtained from the model, are shown in Figure 6.12a for a bias voltage of 0.0 V (black) and 0.8 V (blue). In this energy diagram, every line corresponds to a specific charge configuration (electron distribution) within the island. Multiple lines at equal energy indicate degenerate charge configurations. For example, the first excited state for $N = 1$ is four-fold degenerate and corresponds to the excess electron localized at an edge molecule. For $V = 0\,\mathrm{V}$, the neutral state is most favorable, followed by the $N = 1$ configurations being shifted by the LUMO energy.

An applied bias voltage changes the tip's chemical potential and thereby shifts the configurations with different numbers of excess electrons N against each other. Hence, configurations with larger N become energetically favorable with increasing bias voltage, as shown here for 0.8 V, where $N = 1$ is favored.

Notably, the model reveals that the magnitude of the energetic spacing between ground state and excited states can be quite different depending on the number of excess electrons N. Whereas for $N = 1$, the energetic spacing is only determined by the different electron affinities of the distinct sites, from $N = 2$ the energetic spacing depends on the interplay of electron affinities and repulsive electrostatic interactions of the excess electrons. For example, the similar energies of ground states and excited states for $N = 2$ can be explained as follows: The less favorable edge sites have to be occupied already in the ground state, due to mutual electrostatic interactions. This edge occupation lifts the ground state energy and thereby reduces the energy gap to the first excited state. For the case of three excess electrons, ground-state and first-excited-state configurations are almost degenerate, whereas in the second excited charge configuration two electrons are located at adjacent edge molecules, which leads to a considerable increase in energy.

Notably, for $N = 4$, the energetic spacing between the ground state and the first

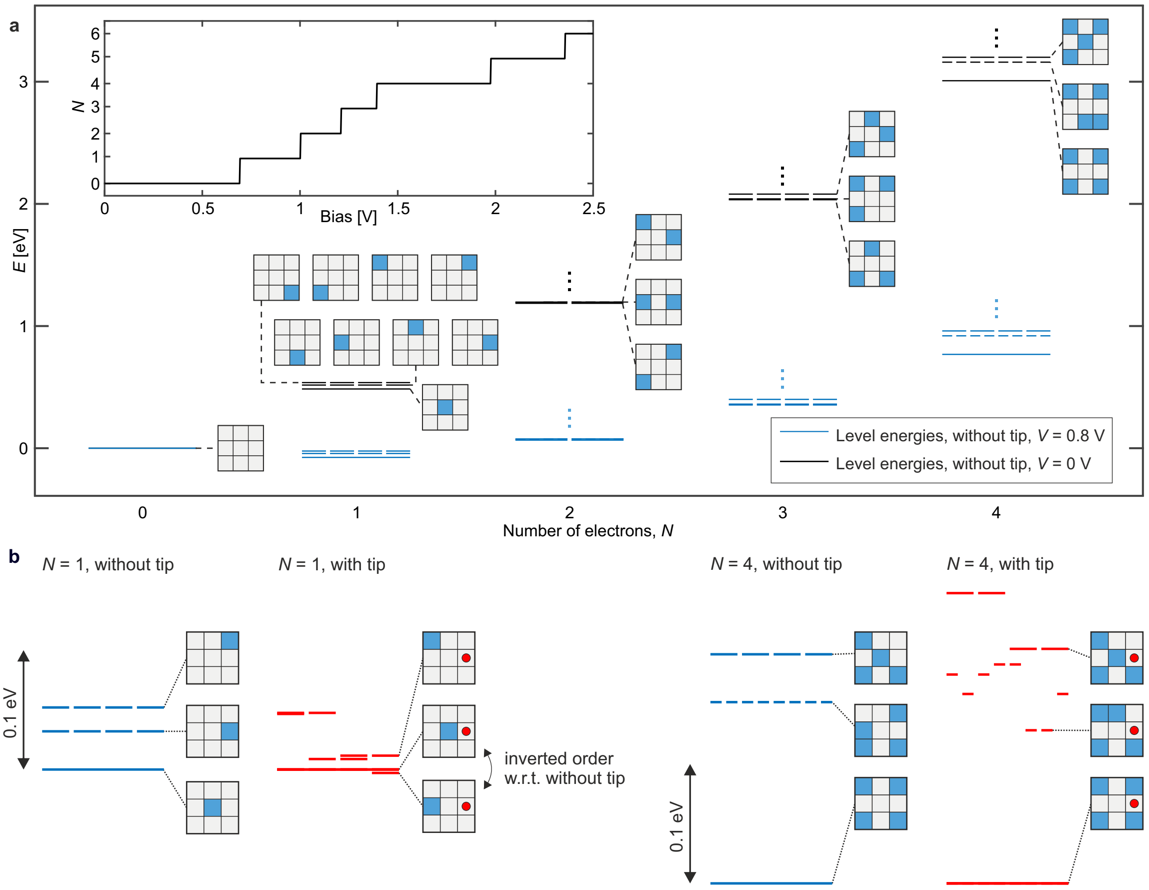

Figure 6.12: **a** Simulated energy diagram of a 3-by-3 PTCDA island without local tip influence for different numbers of excess electrons N obtained from the model, shown for two different bias voltages $V = 0\,\mathrm{V}$ (black) and $V = 0.8\,\mathrm{V}$ (blue). Each line represents one charge configuration, and the number of lines at equal energy indicates the degree of degeneracy. For example, the first excited state for one excess electron ($N = 1$), in which the electron is in one of the four edge molecules, is four-fold degenerate. Likewise, there are four degenerate configurations for the electron in one of the corner molecules. For clarity, only one out of each set of degenerate configurations is shown for $N > 1$ and three vertical dots indicate further possible configurations at higher energies, which are not shown. Inset: number of excess electrons as a function of bias voltage. **b** Dependence of level alignment and electron configurations on the lateral tip position for $N = 1$ and $N = 4$. The tip position was chosen to be above the rightmost edge molecule in the simulations and is indicated by a red dot in each schematic representation of the configurations.

excited state becomes significantly larger. Here, the second-best charge configuration corresponds to two electrons at closest-neighbor molecules, which rationalizes the large energetic separation.

Figure 6.12b shows a comparison of the relative level alignment for $N = 1$ and $N = 4$, with the local tip potential taken into account (red) in comparison to the level alignment without tip (blue). The tip position was set to be above the right edge molecule in both cases. For $N = 1$, the tip influence is strong enough to cause relative level shifts exceeding the 32 meV difference between LUMO energies of center and edge sites. Consequently, with the tip above an edge molecule, the excess electron can be localized at an edge molecule away from the tip. In contrast, for $N = 4$, the level spacing between the ground state and the first excited state is much larger ($\approx$ 150 meV). Thus, the tip influence is not sufficient to favor any charge configuration other than the ground state. In this case, no intra-island charge transfer is expected, and only the configuration with the four electrons in corner molecules is possible, which is in line with the absence of additional dissipation in the experiment and the reduced contrast at the corners in the Δf image (see Fig. 6.8d).

6.11 Simulated spatial dependence of the electron distribution

With that model, we tried to reproduce the observed dissipation contrast by spatially mapping the favored charge configuration in the presence of the tip for the case of one, two, and three excess electrons, which is shown in Fig. 6.13.

To account for inhomogeneities of the environment (defects, step edges, other islands), we included a potential tilt of 3.5 mV/nm from top left to bottom right and an energy offset to lift the degeneracy of the four corner molecules. For the case of one excess charge, the tip influence gives rise to five different charge configurations (see Fig. 6.13a). Whereas the electron is localized at the center molecule for most of the image, the excess charge can be relocated from the center to an edge molecule away from the tip if the tip is in vicinity to an edge position.

For example, if the tip is positioned in the red area (right edge molecule), the charge is preferentially located at the left edge molecule. At the transitions between areas of different colors, the respective charge configurations are close to degeneracy. Hence, the vertical oscillation of the tip can periodically invert the energetic order of the charge configurations and thereby cause dissipation due to periodic charge transfer between edge and center site. However, the energetic difference might be too large to be reverted far inside the circular area, which rationalizes the appearance of two ring-like features in experimental images of the singly charged island.

For $N = 2$ (Fig. 6.13b), the simulation suggests eleven different charge configurations that could be accessed due to the presence of the tip. This large number of charge configurations seems to contradict the experiments, where only two ribbons are visible. However, some of the transitions require a simultaneous charge transfer of two electrons. This could lead to significantly lower tunneling rates, and hence some transitions might not be visible in experiments. In fact, the contour of the pink area inside the island has some resemblance to the experimental image from Fig. 6.8c. All transitions between pink and yellow, black, blue, and brown involve a charge transfer from only one electron to a direct neighbor molecule and hence should be visible in experiments.

Similarly, for $N = 3$, not all transitions, which were suggested by the simulation, can be observed in the experimental images (compare images at 1.25 V in Fig. 6.7). However, some of the transitions, such as black-green and yellow-red, yield good agreement with the experiment. Further, the green-blue and red-blue transitions roughly match the streaks that truncate the circular features at the corners.

In contrast, for $N = 4$ (not shown), the configuration with the excess electrons localized at the corner sites is favored at all tip positions. In this case, the influence of the tip is not sufficient to drive lateral charge transfer in agreement with the absence of additional dissipation in the experiment. This can be rationalized by the significantly larger energetic spacing between the ground-state configuration and the second-best charge configuration for $N = 4$.

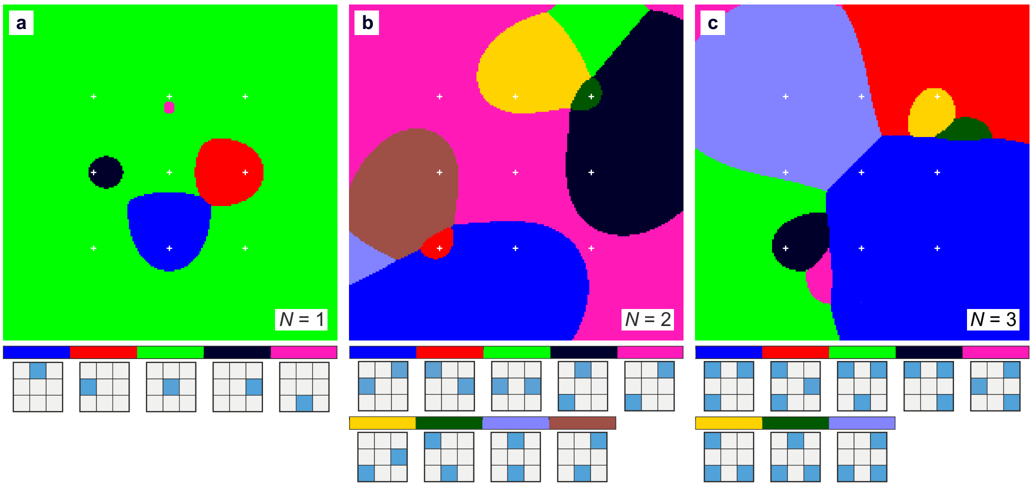

Figure 6.13: Simulated spatial dependence of electron distributions (charge configurations) and lateral tip position for **a** one, **b** two, and **c** three excess electrons. To reproduce the image contrast of the experimental data an additional potential tilt of 3.5 mV/nm and non-degenerate corner sites were included in the simulations. The locally most-favorable charge configurations are plotted in distinct colors, and the corresponding charge configurations are assigned in the legends below the images. Crosses indicate positions of the molecules. ($V = 0.8\,\mathrm{V}$ **a**, $V = 1.05\,\mathrm{V}$ **b**, $V = 1.3\,\mathrm{V}$ **c**)

6.12 Estimation of tunneling rates

Finally, we extracted the tunneling rates that are associated with this intra-island charge transfer. According to Miyahara et al. [44], the tunneling rate Γ can be derived from the ratio of the additional frequency shift Δf_{add} attributed to the charge transfer, divided by the additional dissipation $\Delta\gamma$, as $\Gamma = -8\pi^2 f_0 \Delta f_{add}/\Delta\gamma$, where f_0 denotes the unperturbed cantilever resonance frequency.

Figure 6.14 shows the voltage-dependent Δf_{add} and $\Delta\gamma$ values corresponding to the singly-charging spectrum at the edge molecule from Fig. 6.5a (only the backward curve of the spectrum, where the island is singly-negatively charged). To obtain Δf_{add}, a parabolic background was subtracted [35] and $\Delta\gamma$ was extracted by subtracting the intrinsic dissipation rate according to reference [42]. Obviously, there is a linear scaling between $-\Delta f$ and $\Delta\gamma$, which yields an intra-island tunneling rate $\Gamma \approx 2 \cdot 10^5$ Hz.

Even though our findings support an intermolecular charge transfer as the origin of the observed dissipation, also a charge transfer between tip and island could result in additional dissipation. For the latter, one would expect a tunneling rate that depends exponentially on the tip height, simply due to the exponential dependence of tunneling probability on the tunneling barrier width.

Another spectrum recorded at the same lateral position, with the tip retracted 1 Å further, yields a similar tunneling rate. If the origin of dissipation was tip-island charge transfer, one would expect a reduction of the tunneling rate by one order of magnitude instead, which rules out tip-island tunneling as a source of the additional dissipation.

Independently of that, we extracted the tunneling rate from the image displayed in Fig. 6.8b, recorded with half of the cantilever oscillation amplitude as used for the spectra. From figure 6.14b, it becomes apparent that this gives similar tunneling rates in the range of $2 \cdot 10^5$ Hz. The fact that the tunneling rates depend only weakly on the tip height and oscillation amplitude gives further confidence that the observed dissipation is indeed originating from intermolecular charge transfer. Even though the intra-island tunneling rate should not depend on the tip height, the magnitude of the tip-induced level shift does change with tip height. This could lead to a reduced probability of intra-island tunneling per oscillation cycle and hence reduce the tunneling rate for larger tip heights or lateral displacement of the tip. This might explain the fact that the tunneling rate is not constant within the circular features in the image.

We stress that the determined tunneling rate of $\approx 2 \cdot 10^5$ Hz is very small considering intermolecular distances as small as 4 Å. In fact, we infer that the observed tunneling rate results from the product of tunnel coupling and reorganization energy. The latter, we expect to be in the range of several 100 meV [7, 60], which results in small Franck-Condon factors for the zero-phonon to zero-phonon transition ($\nu = 0 \rightarrow \nu^{'} = 0$) and thereby can explain the low observed rates.

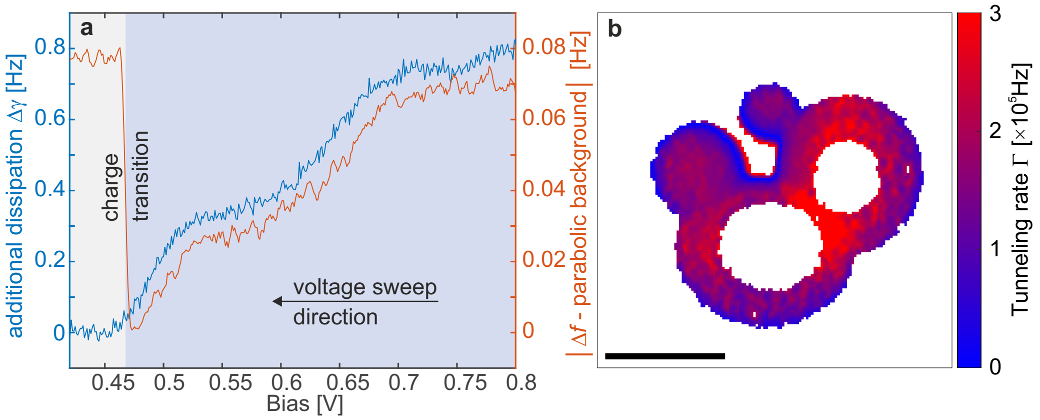

Figure 6.14: **a** Relation between frequency change and dissipation rate due to intra-island tunneling extracted from a single-electron charging spectrum at the edge site (Fig. 6.5a). **b** Tunneling rate extracted from the Δf- and dissipation images in Fig. 6.8. To eliminate the background of the island in the Δf channel an AFM image of the neutral island and an additional constant value were subtracted.

6.13 Contrast changes induced by a defect in proximity to the island

Figure 6.15 shows the same 3-by-3 island being singly-negatively charged at different tip heights after defect formation in close vicinity to the island. This defect was created by contact formation of the tip with the NaCl surface and appears as a faint circular depression in the Δf images (see Fig. 6.15). This defect could be either a Cl^- vacancy or a metal atom that was dropped from the tip. However, the defect can not clearly be assigned to one of those two possibilities at this stage.

At large tip height, the Δf image shows a less attractive (more bright) contrast at the top-edge molecule being closest to the defect (Fig. 6.15a). The dissipation channel is completely featureless, indicating that the electron is stably localized there. Due to the fact that the excess charge was preferentially localized at the center site before defect formation, we infer that the defect acts as an additional tilt on the electron affinities, with molecules being closer to the defect becoming energetically more favorable.

When the tip is brought 1 Å vertically closer towards the sample, a circular feature emerges in Δf and dissipation channel, located between the top-edge and top-right corner molecule.

In Fig. 6.15c, where the tip is even 1 Å closer, another circular feature arises between the top-edge and top-left corner molecules. The observed dissipation pattern suggests that in this case, lateral charge transfer occurs between the top-edge molecule and adjacent corner molecules.

Furthermore, those images reveal that the circular feature appears disk-like at larger

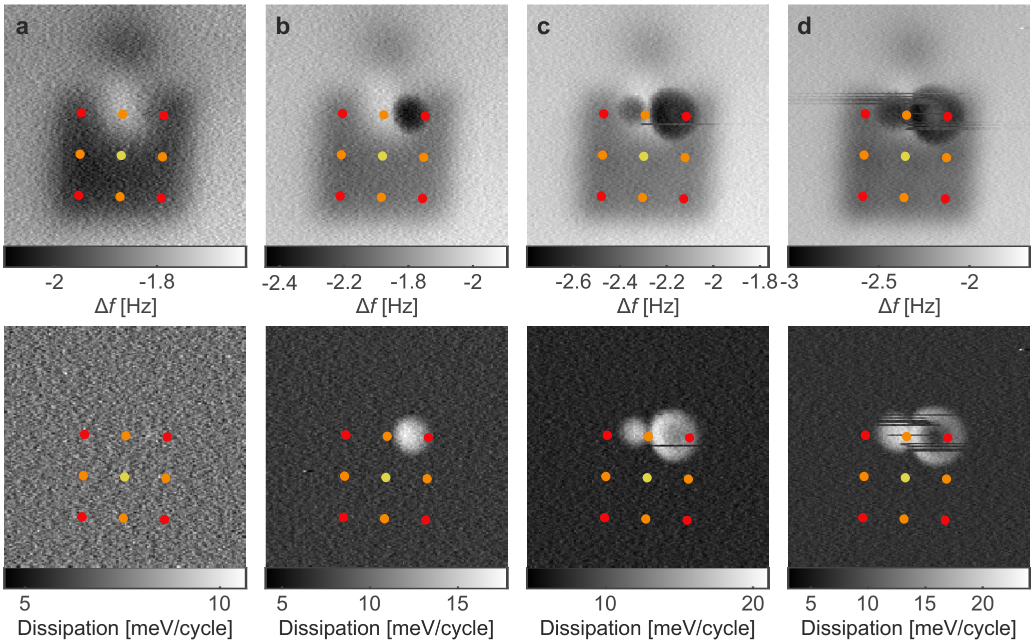

Figure 6.15: **a** Constant-height Δf- (left column) and dissipation image (right column) of a singly charged 3-by-3 PTCDA island at different z-offsets with closeby defect. z-offsets: **a** 5.0 Å, **b** 4.0 Å, **c** 3.0 Å, and **d** 2.5 Å(setpoint: 1 mV, -1.3 Hz, Amplitude: 1 Å, $V = 0.7\,\mathrm{V}$).

tip heights and transforms into a ring at very small tip heights. This implies that the different appearance of the circular dissipation features arises from the relative magnitude of the tip-induced level shifts (depends on the tip height) and the site-dependent differences in electron affinities.

Further, the 3-by-3 island was imaged at different bias voltages similarly as before defect creation, which is shown in Fig. 6.16. In the neutral state (Fig. 6.16a), the Δf contrast is completely homogeneous and no spatial contrast is observed in the dissipation channel.
For one excess electron within the island, two circular features can be observed located between the top-edge and top-corner sites (Fig. 6.16b). In contrast to Fig. 6.15, those features appear more symmetric. From a comparison of the relative position of the defect with respect to the island in constant-Δf images before and after recording the dataset from Fig.6.16, a lateral motion of the defect seems unlikely.
The doubly-negatively charged island (Fig. 6.16c) shows two truncated circular features at the two top corners in the Δf image, but increased dissipation can only be observed at the top-left corner site.
Figure 6.16d shows the island being occupied with three excess electrons. Here, two electrons are stably localized at the top-corner sites, as becomes clear from the less negative Δf (more bright) contrast. Also, additional dissipation occurs in vicinity to the bottom-left corner. The contrast in the bottom-right corner is identical to the

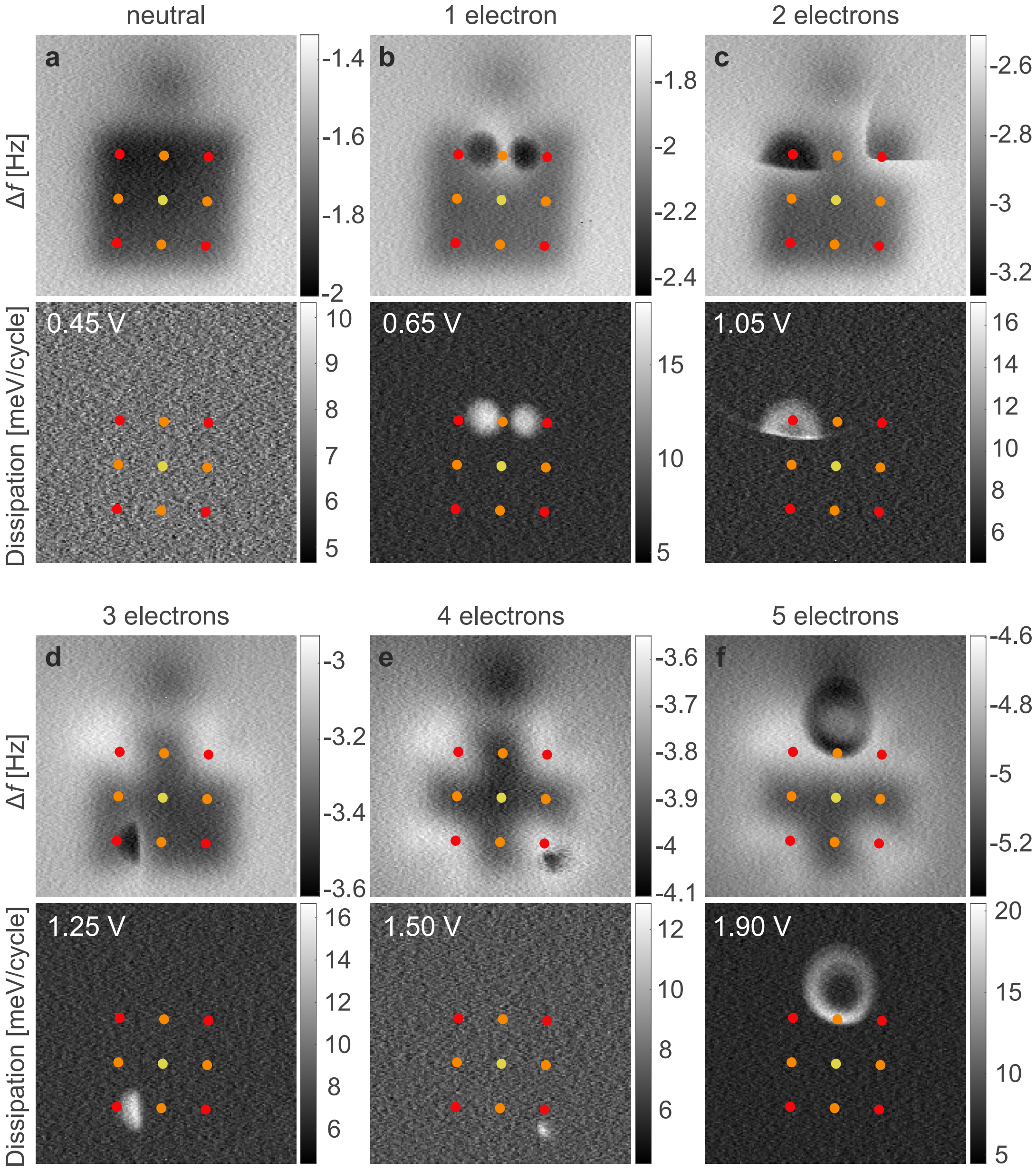

Figure 6.16: Constant-height AFM images and the corresponding dissipation signal of a 3-by-3 PTCDA island in different charge states with defect in close vicinity. In all the images the positions of the individual molecules are marked with coloured dots. Centre (yellow), edge (orange) and corner molecules (red). **a** $V = 0.45\,\mathrm{V}$, **b** $V = 0.65\,\mathrm{V}$, **c** $V = 1.05\,\mathrm{V}$ and **d** $V = 1.50\,\mathrm{V}$. The scale bar corresponds to 20 Å. (Set-point: Δf = -1.3 Hz at $V = 0\,\mathrm{V}$, Amplitude: 1 Å, z-offset: 3 Å.)

neutral island, which suggests that no charge is localized there.
When being four times negatively charged, the four electrons are localized at the corners, only for a small area at the bottom right corner spatial dissipation signatures are observed (see Fig. 6.16e). For five excess charges, a circular feature appears at the upper part of the island, which probably originates from an excess charge being pushed away from the top-edge molecules due to the tip potential. The fact that the island is filled with excess electrons from top to bottom can be rationalized with a defect-induced potential tilt.
With this different tip, the observed dissipation features are also rather in line with a repulsive influence of the tip. This becomes especially clear from the case of two excess electrons (Fig.6.16c). In the lower part of the AFM image, the more bright contrast indicates a localization of the two electrons at the top corner sites, whereas dissipation suddenly sets in, directly above the top-corner site. Similar observations can be made for the case of three excess electrons.
Finally, we deduce the type of defect based on the above observations. To favor an occupation of the molecules in the upper part of the island, their electron affinities need to be increased. Such a shift in the molecules' energy levels would be in line with a positive charge at the surface due to a Cl^- vacancy. In turn, the creation of a Cl^- vacancy could lead to a Cl^--functionalized tip, being accompanied by a distinct contrast from electrostatic force contributions [178]. Indeed, the image contrast in constant-Δf images appeared to be increased after defect formation. Interestingly, the contrast between neutral and charged molecules seems to be larger compared to the metallic tip. This calls for further experiments with different tip functionalizations.

6.14 Probing the electron distribution in a 2-by-2 and 2-by-4 island

The results for the 3-by-3 island revealed that the contrast formation - besides the number of charges and their mutual repulsion - depends on the relative energetic difference of specific sites but also on the background potential of the environment. Further, it became clear that the geometry of an island crucially influences, which sites are most favorable and hence influences where intra-island charge transfer can occur. For this reason, we also investigated a 2-by-2 (Fig. 6.17) and a 2-by-4 island (Fig. 6.18). Unlike the 3-by-3 island, based on symmetry arguments, the 2-by-2 and 2-by-4 islands should have more than one possible ground state configuration, which makes them interesting cases to study.

First, we discuss the contrast of the 2-by-2 island imaged at different bias voltages, which is shown in Fig. 6.17. The schematic inset in Figure 6.17a indicates the arrangement of molecules within the island. Further, molecules that have a different environment are marked with red and orange dots, respectively. The neutral island appears as a homogeneous square feature in the Δf image (Fig. 6.17a). A similar faint square-like feature is present in the corresponding dissipation image, which is attributed to the background of the island due to the similar appearance. The bias voltage of $V = 0.2\,\mathrm{V}$ is far below the necessary voltage threshold for injection of the first excess charge, for which reason charging can be excluded as the origin of this background dissipation. Probably, this background dissipation originates from an unstable tip causing additional dissipation due to the interaction with PTCDA islands.

At $V = 0.65\,\mathrm{V}$, the island is singly negatively charged and two diagonal stripe features appear in Δf and dissipation roughly located at the red dots. This pattern has some resemblance to the stripe pattern of the twice negatively charged 3-by-3 island (Fig. 6.8). At a bias voltage of $V = 0.95\,\mathrm{V}$, but still in the same charge state, the dissipation pattern changes, and a circular feature at the bottom-right molecule appears.

At $V = 1.10\,\mathrm{V}$ (Fig. 6.17d), the island is twice negatively charged, which becomes clear from comparison to the Δf image of the neutral island. This contrast difference implies that the two excess electrons are localized at the corners marked with

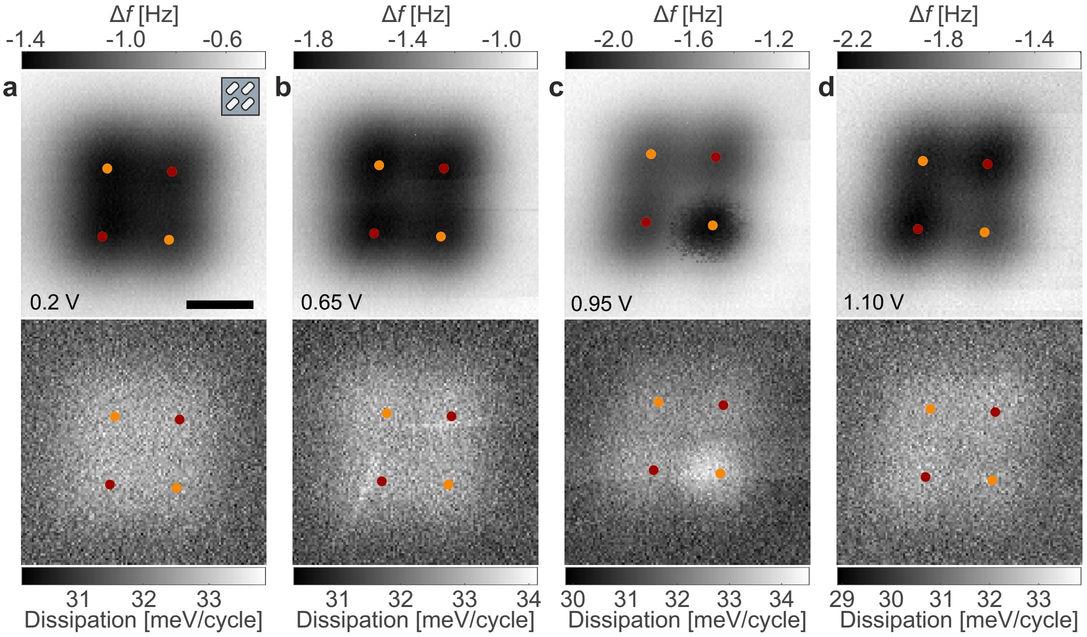

Figure 6.17: Constant-height AFM images (top) and the corresponding dissipation images (bottom) of a 2-by-2 PTCDA island in different charge states. In all the images the positions of the individual molecules are marked with colored dots. Different types of corner molecules are marked with red and orange dots, respectively. **a** $V = 0.2\,\mathrm{V}$, inset: orientation of the molecules within the island, **b** $V = 0.65\,\mathrm{V}$, **c** $V = 0.95\,\mathrm{V}$ and **d** $V = 1.1\,\mathrm{V}$. The scale bar corresponds to 20 Å. (setpoint: $V = 1\,\mathrm{mV}$, $\Delta f =$ -1.1 Hz, z-offset: 3.0 Å, amplitude: 1 Å)

orange dots. The preferential occupation of this specific corner types can have two reasons. First, the specific environment makes two of the four sites more favorable. Another explanation could be that there are two non-equal types of corner sites with different electron affinities due to a different screening. A comparison to the ground state of two excess electrons in the 3-by-3 island reveals that the same type of corner molecules are preferentially occupied, which supports the presence of non-equivalent corner sites. For the specific arrangement of PTCDA molecules within the islands, the two-fold symmetry of PTCDA gives rise to two different types of corner molecules, which rationalizes a non-degeneracy of the four corners. Further, the charging thresholds for one and two excess electrons are comparable to the values that were obtained for the 3-by-3 island.

Figure 6.18 shows Δf and dissipation images of the 2-by-4 PTCDA island at different bias voltages. In those images, edge and corner sites are marked with orange and red dots, respectively. The inset in Fig.6.18a suggests that all edge molecules should be equivalent, whereas there are two different types of corner sites. All images of the 2-by-4 island reveal a faint background dissipation similar to the images of 2-by-2 island. Apart from that background dissipation, the images of the neutral island are completely featureless (see Fig. 6.18a).
After an electron is injected, a dissipation pattern emerges, which is approximately symmetric with respect to a vertical axis through the center of the image (Fig. 6.18b). The following images show more qualitative changes in image contrast than expected charge state transitions. In these measurements, mechanical noise problems led to discrete signal changes during AFM measurements. Hence, we can not clearly assign charge states to the Figures 6.18c-e. However, from Fig. 6.18c on, one site appears more bright, indicating a charge stabilization while at other positions, lateral charge transfer can be driven.
In Fig. 6.18f, the charge configuration is stable, and based on $\Delta f(V)$ spectra, we assume that the island is four-times negatively charged. The subtle contrast differences in the Δf image indicate that three excess electrons are located at corner molecules (the two left and the top-right corner sites), whereas the fourth excess electron is located at the bottom-right edge molecule. This charge configuration might appear to be uncommon. However, an occupation of the four corners would lead to two pairs of direct neighbors with a strong repulsion, all being located at the unfavorable corner sites, for example. In a zig-zag configuration, all charges would have direct diagonal neighbors, which could lead to a larger mutual electrostatic repulsion.
Even though all three island geometries are rather simple and have a high symmetry, the experiments show that the dissipation patterns are complicated to interpret in many cases. We conclude that the observed dissipation crucially depends not only on the interplay of tip-induced level shifts, mutual electrostatic interactions, but is also influenced by the site-dependent relative energetic alignment of molecular levels. The latter are predefined by the geometry of the islands, but can additionally be modified by the environment of the island.

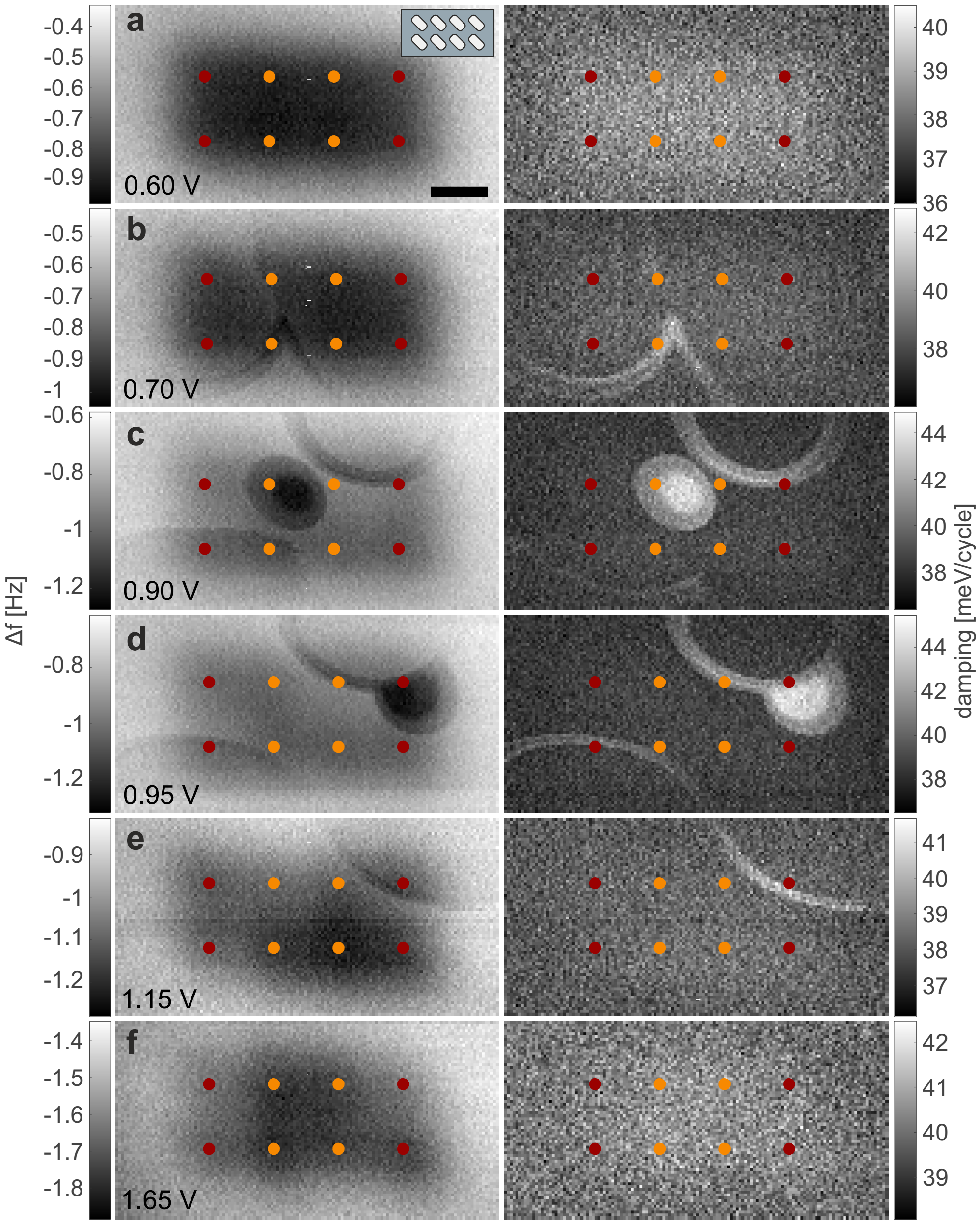

Figure 6.18: Constant-height AFM images (left column) and the corresponding dissipation signal (right column) of a 2-by-4 PTCDA island in different charge states. In all the images the positions of the individual molecules are marked with colored dots. Center (yellow), edge (orange) and corner molecules (red). **a** $V = 0.45\,\mathrm{V}$, **b** $V = 0.65\,\mathrm{V}$, **c** $V = 1.05\,\mathrm{V}$ and **d** $V = 1.50\,\mathrm{V}$. The scale bar corresponds to 20 Å.) (setpoint: $V = 1\,\mathrm{mV}$, $\Delta f =$ -1.1 Hz, z-offset: 3.0 Å, Amplitude: 1 Å)

6.15 Conclusion

In this chapter, we investigated electrically-isolated self-assembled islands and found that the charge state of those structures can be read and manipulated with single-electron control. Depending on the charge state of the islands, we either observed stable distributions of excess electrons or spatial Δf and dissipation signatures, which we assign to an intermolecular charge transfer driven by the local influence of the tip.

An electrostatic model was used to simulate the electron distribution within an island depending on the position of the tip. This model showed that the energetic difference between different charge configurations depends on the alignment of on-site energies, the magnitude of tip-induced level shifts, and mutual electrostatic repulsion of excess electrons. Further, we found indications for an additional influence of the environment's potential landscape on the electron distribution.

Finally, we also extracted the tunneling rates from the experimental data. We found rates in the range of $2 \cdot 10^5$ Hz relatively independent of the tip height, which supports the suggested mechanism of intra-island tunneling. The measured tunneling rate is not only determined by the tunneling probability but additionally modified by the reorganization energy resulting from the geometric reaction of the molecule and the substrate on the excess charge.

Those results call for further experiments, for example, a close-by molecular island could be deliberately charged to clarify the influence on the charge distribution and dissipation contrast in the investigated island.

Alternatively, metal atoms could be co-deposited and exploited to manipulate the charge configurations within islands [99, 100]. By manipulating the charge state of a close-by atom [7], the external perturbation on charge configurations within an island could be even switched on and off. On the one hand this approach would be more demanding to realize, but on the other hand it would be a simpler system compared to charging close-by islands. In a specific voltage range, one could probably even realize positive and negative charge states with metal adatoms [31, 51].

Furthermore, the role of tip functionalizations [79] on the sign and magnitude of tip-induced level shifts could be explored more systematically.

It would also be interesting to study such charge transfer processes in one-dimensional molecular structures. To this end, molecular self-assembly experiments have been carried out with several different molecules, but we did not yet find a system that grows as isolated, ordered one-dimensional chains on an insulator surface.

Ultimately, one could think of such charged islands (e.g. doubly charged 2-by-2 islands) as building blocks for quantum cellular automata (QCA) [168, 169]. However, one would have to find an efficient possibility to create repetitive arrangements of such structures on an insulating surface.

7 Stabilizing a confined out-of-equilibrium state by polaronic shifts

The results presented in this chapter have been acquired and interpreted in collaboration with Laerte Patera and Jascha Repp. This chapter provides a tentative interpretation of experimental observations.

It was found that individual PTCDA molecules and PTCDA molecules within self-assembled islands, on a few monolayers thin NaCl layer, can be switched by applying voltage pulses. We characterize the changes in the electronic structure and geometric relaxations that occur upon charging. Based on our experimental findings, we assume that the switching is related to the charging of a molecule. These results indicate that the additional electron does not occupy the LUMO, but suggest that it is localized at a functional group of the molecule. We propose a tentative mechanism for the observed charge stabilization, based on a strong polaronic interaction with the ionic substrate, due to spatial confinement of the excess electron at a molecule's functional oxygen.

This chapter comprises two complementary experiments. In the first part, we investigate the effects of switching on PTCDA molecules within self-assembled PTCDA islands, which were grown on a few monolayers thin NaCl film. In the second part, we study the effects of switching on the electronic structure of individual PTCDA molecules and relate them to the geometric relaxations due to switching.

7.1 Introduction

In 2004 Repp and colleagues found that individual Au atoms, adsorbed on ultrathin NaCl films exhibit charge bistability and showed that the charge state of individual Au atoms can be manipulated by applying voltage pulses [7]. A few years later, Olsson et al. showed that Ag atoms exhibit a charge tristability under similar conditions [51].

Wu et al. found that molecules can be controllably switched between their neutral and anionic state, in a similar way [48, 49].

Due to the strong tunnel coupling to the supporting conductive substrate, an adsorbate on thin insulating films can only be stabilized in different charge states under certain conditions [7, 8, 31, 51]. One requirement is that the adsorbate's state is close enough to the Fermi level of the substrate. Further, the energetic shift due to reorganization energy upon injecting/removing an electron into/from the adsorbate has to be large enough to shift the state across the Fermi level. Accordingly, the stable coexistence of different charge states is usually restricted to a specific bias voltage range, defined by the interplay of tunneling probability and reorganization energy [7, 8, 31, 51].

Recently, controlled charge state manipulation was also reported for single CuPc molecules [8]. In this case, however, the observed bistable window was much narrower ($\approx 0.3\,\mathrm{V}$) compared to charging of atoms ($> 1\,\mathrm{V}$) [7, 31, 51]. Due to the additional electron being distributed over the entire molecule [8], this reduced width of the bistable window might be related to a smaller reorganization energy [59]. Leoni et al. reported on charge bistability of bis-dibenzoyl-methanato-copper molecules [50]. In their case, the bistable window was exceptionally large ($\approx 4\,\mathrm{V}$). However, the investigated molecules experience a conformational change upon charging from a planar to a tetrahedral geometry [50], for which reason these results cannot be directly compared. Also, in the experiments by Wu and colleagues, the bistable window was rather large, however, they used aluminum oxide as decoupling layer [48, 49], whereas all the above experiments were performed for adsorbates on NaCl films [7, 8, 31, 50, 51].

In all those studies, the additional electron is stabilized in the formerly lowest unoccupied state [7, 8, 31, 48–51].

Here, we investigate individual perylenetetracarboxylic dianhydride (PTCDA) molecules and self-assembled PTCDA islands, on thin insulating films on a supporting Au(110) substrate. We find that PTCDA molecules can be switched by applying voltage pulses.

High-resolution AFM images with CO-functionalized tips [9], revealed local geometric relaxations within a PTCDA molecule upon switching. Further, we used STM to resolve the changes in the electronic structure of PTCDA upon switching.

Based on our experimental findings, we tentatively assign the switching to the charging of a molecule.

In contrast to previous studies, our observations suggest that the additional electron does not occupy the LUMO, but is localized at an anhydride group of PTCDA. Finally, we suggest a tentative model to explain this charge stabilization, based on extraordinary large polaronic level shifts due to strong spatial charge confinement of the excess electron at a functional anhydride group's oxygen atom.

7.2 Sample preparation

For the experiments presented throughout this chapter, a clean Au(110) surface was prepared, followed by the growth of a few monolayers thin (<5ML) NaCl film according to the procedure described in chapter 3. The self-assembly was performed analogous to the procedure described in the previous chapter. All experiments on individual PTCDA molecules and AFM measurements on self-assembled PTCDA molecules were carried out on a two monolayers thin NaCl film. The STM- and KPFS measurements of self-assembled PTCDA islands were conducted on a sample with an average NaCl coverage of ≈ 3.5 ML. In this case, it was not possible to clearly determine the actual layer thickness at each spot, on which the measured PTCDA islands were adsorbed. Additional STM experiments of self-assembled PTCDA islands on a bilayer, however, show the same behavior. Thus, the layer thickness (for less than 5ML) is not expected to play a crucial role.

7.3 Geometric structure of self-assembled PTCDA islands

Figure 7.1a shows an STM image of a 4-by-4 PTCDA island after the self-assembly, which reveals a characteristic stripe pattern. The latter is attributed to a superposition of dumbbell-shape orbitals corresponding to the LUMOs of individual mole-

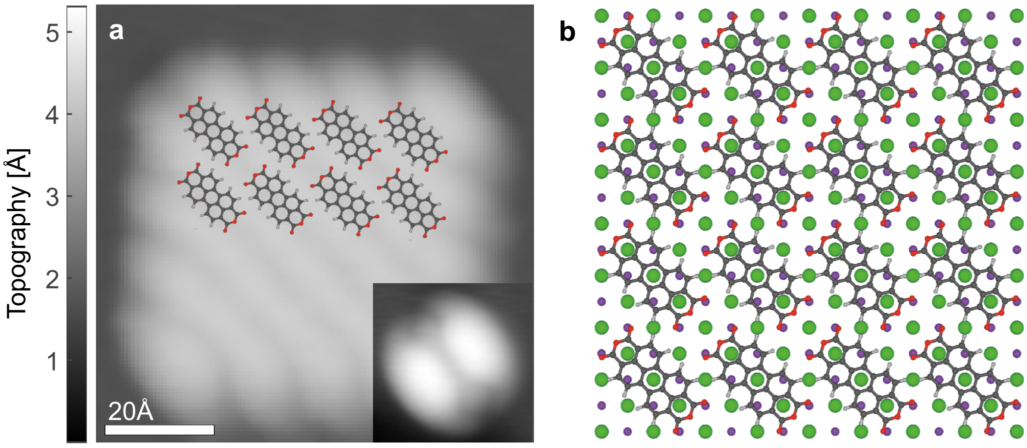

Figure 7.1: **a** Constant-current STM image of a 4-by-4 PTCDA island, where partially molecular structure models were superimposed (setpoint: 2.6 pA, 2 V). Inset: STM image resembling the LUMO of an individual PTCDA molecule (setpoint: 1.8 pA, 0.93 V). **c** Adsorption geometry model of self-assembled PTCDA on NaCl. C (gray), O (red), H (white), Na$^+$ (purple), Cl$^-$ (green).

cules, with a nodal plane along the long molecular axis (see inset image of individual PTCDA for comparison) [148, 158, 159]. In part, molecular structure models of PTDCA molecules were superimposed to visualize the adsorption geometry. As discussed in the previous chapters, PTCDA molecules assemble in a brick-wall c(4 × 4) superstructure on NaCl [160], with PTCDA centered above Cl^- [148, 159, 160]. This adsorption geometry is visualized in Fig. 7.1b. Furthermore, the outer oxygens of the PTCDA anhydride groups are well aligned with the position of the Na^+ ions of the topmost NaCl layer. For more details on the self-assembly and growth characterization, it is referred to chapter 5.

7.4 Switching of PTCDA molecules within self-assembled PTCDA islands

7.4.1 Switching PTCDA molecules

Figure 7.2a shows an STM image of a 4-by-4 PTCDA island recorded at constant height. An $I(V)$-spectrum, acquired at the position of the red dot, experiences two subsequent, sharp steps in tunneling current at ≈ 2.8 V (Fig. 7.2b). The subsequent STM image reveals two bright features, symmetrically around the center of the island, indicating that two molecules possibly have switched. As will be shown in the following, this switching results in an energetic shift of the molecular states and structural relaxations in vicinity to an anhydride group. Further, we found that sometimes two switching events can be induced per molecule, accompanied by a further energetic shift of the molecular states and geometrical relaxations at the second anhydride group. According to these changed properties, we will refer to pristine, singly, and doubly switched molecules as, *P*-, *S*-, and *D*-type(-state) molecules, respectively, throughout this chapter. Here, the occurrence of two steps in the tunneling current

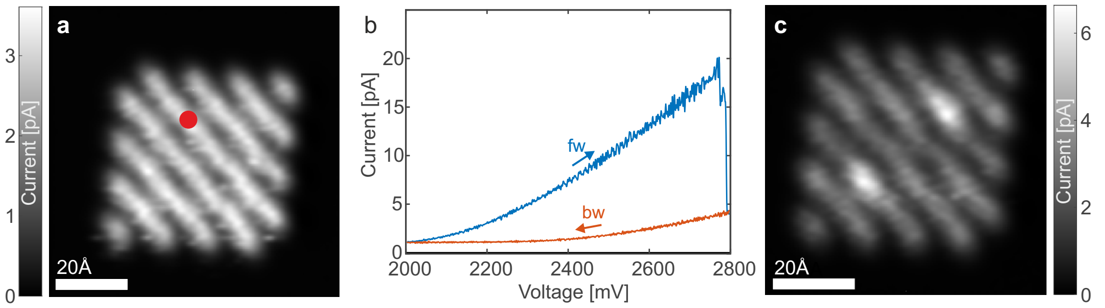

Figure 7.2: **a** Constant-height STM image of a 4-by-4 PTCDA island. **b** *I(V)*-spectrum acquired at the position of the red dot in **a**. **c** Constant-height STM image of the same PTCDA island after the spectrum. (Setpoint: 2.6 pA, 2.0 V , z-offset: 5.6 Å)

is ascribed to the switching of two molecules from the *P*-state to the *S*-state. Further, we assume the pristine molecules to be neutral (see section 7.5.1).

Figure 7.3 shows a comparison of constant-height STM images, recorded at different bias voltages, before and after switching. Whereas the contrast is homogeneous all over the island before switching (top-row images), the *S*-type molecules have a distinct contrast at all bias voltages (bottom-row images). This distinct contrast of *S*-type molecules originates from an energetic shift of the LUMO resonance upon switching, leading to a different current intensity at fixed bias voltage. From these images, it becomes clear that the *S*-type molecules can be characterized easiest at $V = 1.6\,\mathrm{V}$ in constant-height images. Further, the images, recorded at $V = 1.6\,\mathrm{V}$, reveal that only one of the lobes of each *S*-type molecule appears brighter. In general, this distinct current contrast allows us to distinguish between *P*-, *S*-, and *D*-type molecules in STM images.

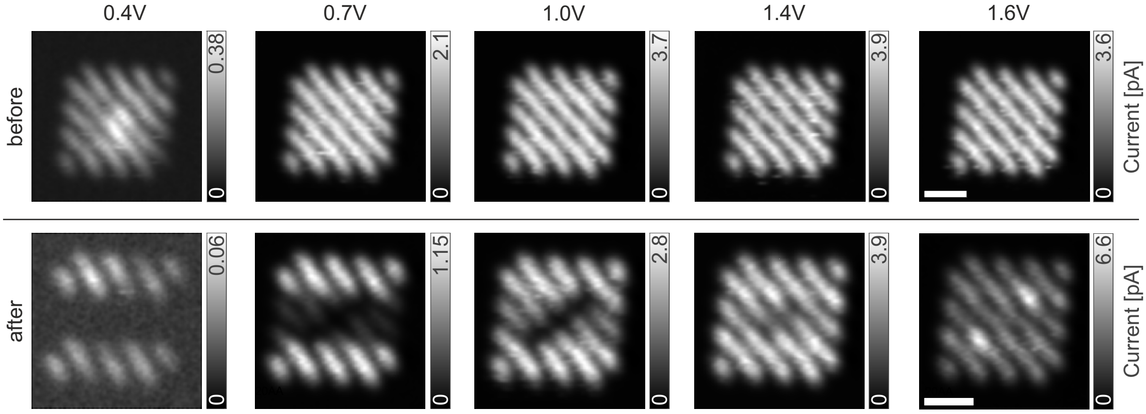

Figure 7.3: Constant-height STM images of a 4-by-4 PTCDA island at different bias voltages before (top) and after (bottom) switching two molecules. The corresponding voltages are given above each column. The scalebars correspond 20 Å. (Setpoint: 2.6 pA, 2.0 V, z-offset: 5.6 Å,)

To clarify whether this switching is reversible, *I(V)* spectra at reverse bias were recorded. For negative voltages up to V= -4 V, no reverse switching was observed.
However, if positioning the tip above the island, away from the *S*-type molecules, and sweeping sample voltage to $V <$ -2 V, it was found that other molecules within the island, which are closer to the tip, could be switched to S-type while the originally S-type molecule returned to the *P*-state (see Fig. 7.4). Whereas the spectra in Figs. 7.4a-c were acquired with the tip directly above the island, the tip was positioned laterally offset with respect to the island in Fig. 7.4d. All four shown spectra resulted in a change of the configuration within the PTCDA island, but only if the tip is positioned directly above a molecule within the island, successful manipulation can be recognized in the spectra as a sudden drop in tunneling current. In total, four different arrangements of the *S*-type molecules (island configurations) were achieved for this specific 4-by-4 PTCDA island, of which corresponding STM

images are shown as insets. In contrast, different island configurations were observed for another equivalent 4-by-4 island. Therefore, we assume that there might be favorable configurations but additional influence from the environment of the island or the specific shape of the tip. The fact that only certain arrangements of S-type molecules were achieved within the islands (in total 16 molecules) implies that there could be a mutual interaction between switched molecules. From those mutual interactions and the observation that S-type features could be shifted towards the tip at negative voltages, at this stage, we imply that the switching is possibly associated with the charging of a PTCDA molecule.

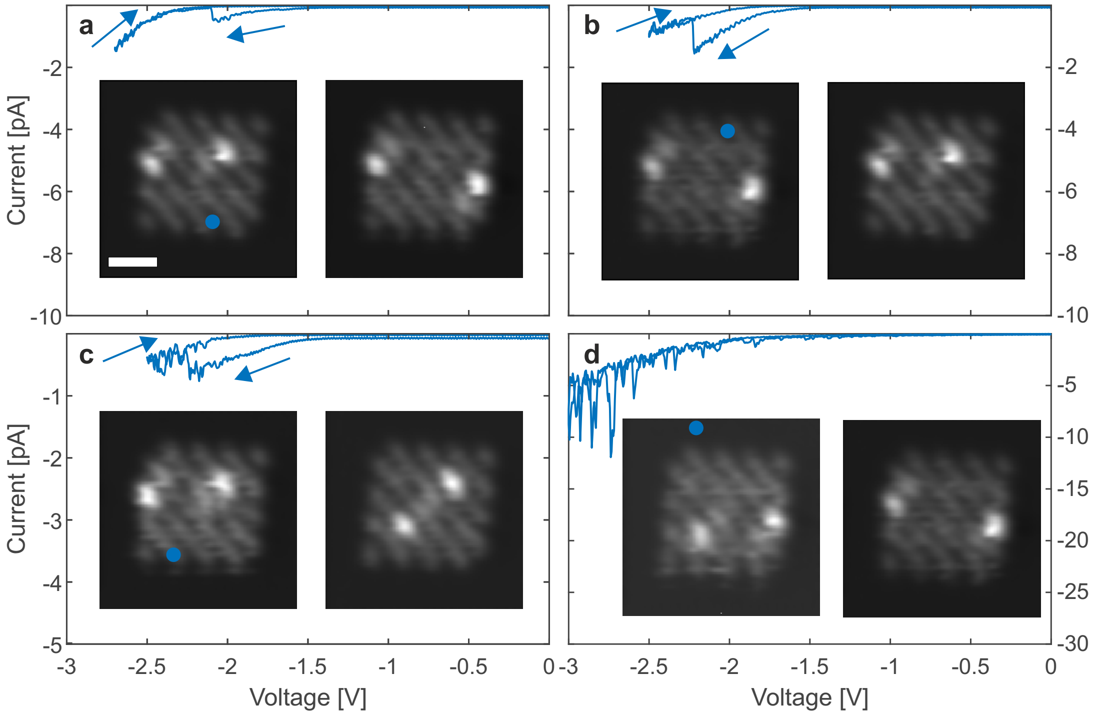

Figure 7.4: Switching between different configurations in a 4-by-4 PTCDA island with two S-type molecules. **a-d** Spectra that caused a successful manipulation of the island configuration. The left (right) inset images are constant height STM images before (after) the manipulation spectra. The dots indicate the position of the corresponding spectra. The scalebar is 20 Å. (Setpoint: 2 V, 2.6 pA, V = 1.6 V, z-offset: 6.3 Å for images and 0 Å for spectra.)

7.4.2 Switching single PTCDA molecules within an island: STS-measurements

To gain further insight into the underlying mechanism of the switching, we acquired sets of dI/dV spectra at different spatial positions of the 4-by-4 island before and after switching. Figures 7.5a-d show constant-height STM images of the PTCDA island in different states, namely pristine (Figs. 7.5a,b are identical but with different colorbar range) and with two S-type molecules at two different positions within the island (Figs. 7.5c,d). Here, the superimposed dots mark the position of single spectra, and the dot color indicates the voltages V_p corresponding to the maxima of the dI/dV spectra. The spectra positions were chosen such that they coincide with the spatial positions of lobes of the individual molecules. The dumbbell-shaped LUMOs corresponding to three PTCDA molecules are schematically indicated in Figs. 7.5a,b, respectively. The spectra range was limited to positive bias voltages to avoid switching between different island configurations during data acquisition. Further, dI/dV spectra on a PTCDA island were featureless at negative sample voltages in a comparable voltage range.

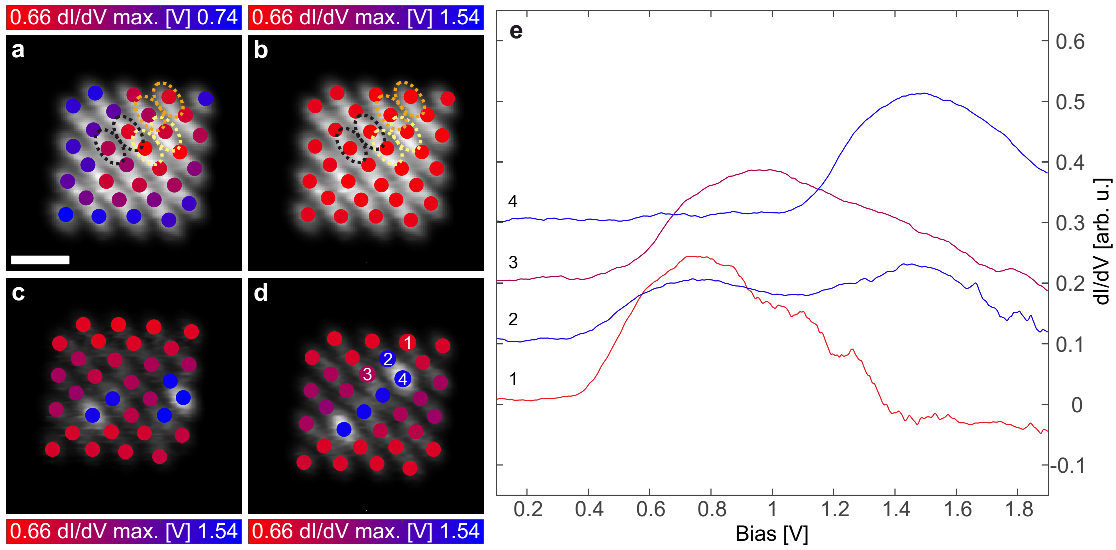

Figure 7.5: Spatial dependence of dI/dV peak voltages of **a,b** the pristine and **c,d** the island with two S-type molecules at different positions within the island. The colorscale in **a** is chosen for maximum contrast and colorscale for **b,c,d** is identical for better comparison of pristine and switched configurations. **e** Selected dI/dV spectra, whose positions are indicated by corresponding numbers in **d**. The shown spectra are smoothened and are vertically offest, for clarity. The dI/dV-peak maxima in **a-d** were determined from polynomial curve fitting. The scalebar corresponds to 20 Å (Setpoint: 2 V, 2.6 pA, z-offset: 6.3 Å for images and 0 Å for spectra, modulation voltage $V_{pp} = 20\,\text{mV}$, modulation frequency $f = 185\,\text{Hz}$).

For the pristine island, the *dI/dV* peaks range from $V_p = 0.66\,\mathrm{eV}$ - $0.74\,\mathrm{eV}$, with values decreasing towards the center of the island (Fig. 7.5a). Similar energy level shifts were observed for clusters of PTCDA/NaCl(2ML)/Ag(111) and were related to a different charge screening for molecules at the center and the periphery of the island due to their different environment [148]. After switching two molecules within the island to S-type, local *dI/dV* peak shifts up to $V_p \approx 1.5\,\mathrm{V}$ are observed at the positions of the S-type molecules (see Figs. 7.5c,d). Notably, the dI/dV peaks of neighboring molecules are also shifted considerably towards higher voltages.

For a more detailed insight, we compare individual spectra at different characteristic positions in Fig. 7.5e, which represent the qualitatively different types of spectra that have been observed. The numbers 1-4 assign the spectra to the corresponding positions in Fig. 7.5d. Spectrum 1, which was taken at a P-type molecule, shows one peak at $V_p \approx 0.75\,\mathrm{V}$ and spectrum 4, which was taken at a S-type molecule, exhibits a peak at $V_p \approx 1.5\,\mathrm{V}$. Spectrum 2 was taken at the lobe of a P-type molecule in direct neighborhood to a S-type molecule and exhibits two maxima of similar intensity, whose values V_p coincide with those of spectrum 1 and spectrum 4. Therefore, the presence of two distinct peaks in a spectrum is attributed to a spatial overlap of orbital density of neighboring P- and S-type molecules, and we consider such spectra to show a superposition of signals from two distinct orbitals.

In contrast, spectrum 3 shows a peak that does neither match the energy of a pristine nor of a switched molecule. This can also be seen in the spectroscopic grids, where dot colors do not only correspond to minima (red) and maxima (blue) of the color scale, but also intermediate values (purple) are observed. Such peak values can not be explained by a superposition of two peaks at $V_p \approx 0.7\,\mathrm{V}$ and $V_p \approx 1.5\,\mathrm{V}$, here. However, it is known that the presence of local charges can cause energetic level shifts [99, 100, 170], which would be an indication for a charge transfer upon switching.

Due to the spatial overlap, a hybridization of states in neighboring molecules is conceivable, to some extent. However, no signatures of a state, being delocalized over the entire island, were observed. This is not surprising since the intermolecular coupling in such a hydrogen-bonded network should be rather weak, compared to covalently-bond networks.

7.4.3 The effect of switching on the local contact potential difference

KPFS allows to detect subtle variations of charge distributions at a surface based on their influence on the local work function [11, 35]. For example, charge state detection of single atoms [11] and even charge distributions within single molecules [37, 38] could be detected by means of KPFS. Hence, it provides a useful method to clarify whether the observed switching is related to charging.

For this reason, we recorded a set of KPFS spectra at different spatial positions of a

5-by-5 PTCDA island, after switching one molecule to S-state. Figure 7.6a shows two such KPFS spectra, where one was recorded above a P-type molecule (red) and the other was recorded roughly at the anhydride group of the S-type PTCDA molecule (blue). The voltages V_{CPD}, corresponding to the Δf maxima, were obtained by parabolic curve fitting. In Figure 7.6b colored dots indicate the position and V_{CPD} values of all spectra in an STM image of the island. This map reveals that the LCPD is rather constant all over the island, only in vicinity of the switched molecule, the LCPD is increased by $\approx 30\,\mathrm{mV}$. This slight shift towards smaller absolute but negative values indicates that the work function of the sample has locally increased and the direction of the shift is in line with an additional negative charge at the surface [11].
Figure 7.6c shows the same spectroscopic map, superimposed to a CO-tip AFM image, revealing that the LCPD changes most in proximity to the anhydride group.

In summary, the KPFS measurements indicate an accumulation of electron density at a PTCDA's anhydride group upon switching. It must be noted that a vertical relaxation of the molecule upon switching to S-type, could also lead to a measurable change in the LCPD and hence this result alone should not be considered as a clear evidence for charging. However, the aforementioned gating of the LUMO resonance in the dI/dV spectra, the mutual interactions, and the attractive influence of the tip at negative sample voltages support a charge transfer.

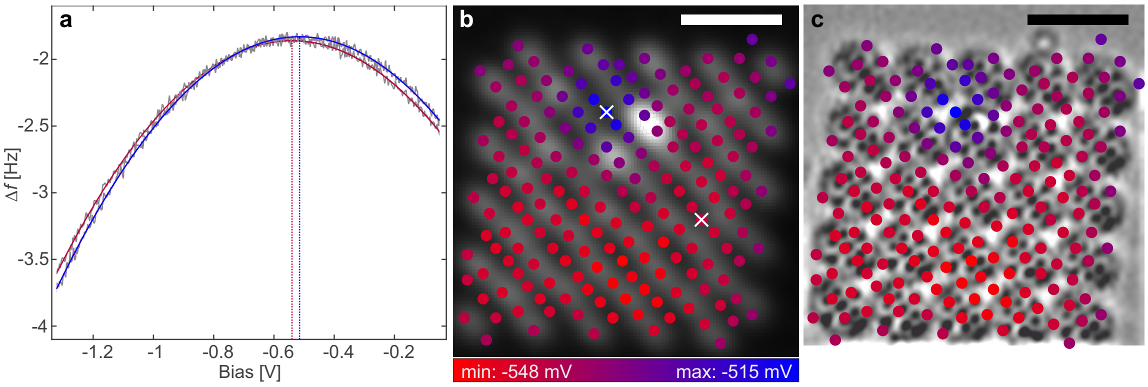

Figure 7.6: **a** Two KPFS parabola recorded at different spatial positions of a 5-by-5 PTCDA island, of which one molecule has been switched. Smoothened Δf data (grey) and parabolic fits (colored). **b** Spatial dependence of the LCPD within the island, superimposed on a constant-height STM image. Each circle represents the position of a Δf(V)-spectrum and the color indicates the corresponding LCPD value. White crosses indicate the positions, at which the spectra from **a** were acquired. **c** Laplace-filtered CO-tip AFM image of the same island, with superimposed LCPD map. All data were acquired at constant height. The scalebars correspond to 20 Å. (set-point: 1.8 V, 1.3 pA, z-offset: 5.5 Å for the spectra, for images **b** 7.0 Å, **c** 4.5 Å, amplitude: 0.5 Å.)

7.4.4 Structural changes upon switching

In order to further elucidate the switching mechanism, AFM measurements with CO-tips [9] were acquired for a PTCDA island before and after switching, providing detailed information about changes in the geometric structure at the atomic scale.

To this end, several voltage pulses were applied above an island to initiate switching of single molecules and, subsequently, an STM and AFM image of the island in the same configuration were recorded in order to relate STM- and AFM-contrast features of switched molecules. Figure 7.7 shows an STM and AFM image after switching several molecules, where all different types of switched molecules can be observed. Before discussing the specific types, we will describe some general findings.
S-type molecules show a dark halo at one anhydride group, and for D-type molecules, such a dark halo can be observed at both anhydride groups. Furthermore, the AFM image reveals that all switched molecules undergo vertical relaxations. Those relaxations can be qualitatively quite different for the case of S-type molecules, but all S-type molecules have in common that the perylene unit inhomogeneously relaxes upwards, with the largest vertical relaxation close to an anhydride group. The relaxations within S-type molecules can be further classified by their symmetry with respect to the long molecular axis of PTCDA.

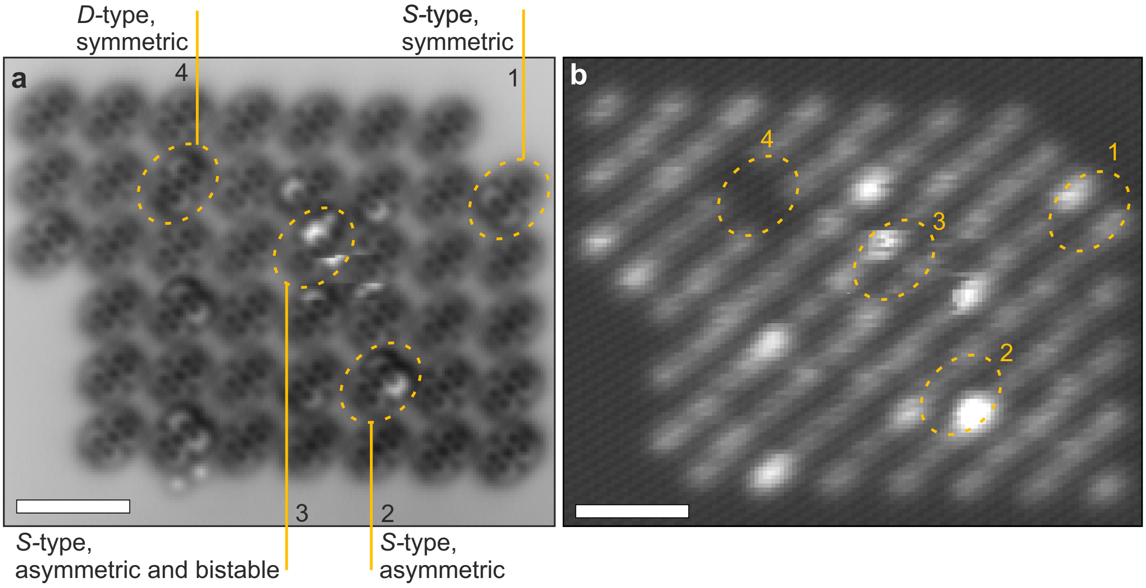

Figure 7.7: Comparison of AFM (**a**) and STM (**b**) images of a PTCDA island, with several switched molecules. Both images were acquired at constant height. All molecules are in the same configuration in both images. The scale bars correspond to 20 Å (set-point: 2.8 pA, 35 mV, z-offset: 2.2 Å, amplitude 0.5 Å (**a**), set-point: 2.8 pA, 1570 mV, z-offset: 5.5 Å, bias = 1.6 V (**b**).

In order to describe these relaxations in more detail, different types of switched molecules were assigned to numbers in both images.

Molecule 1 represents an S-type molecule where the perylene unit is relaxed symmetrically away from the surface, with respect to the long molecular axis (i.e. the rings close to one anhydride group appear brighter - see Fig. 7.7a). The STM image (Fig. 7.7b) reveals a moderate intensity difference of the corresponding LUMO lobes. Molecule 2 is also S-type, but shows a strong asymmetry with respect to the long molecular axis, accompanied by a strong intensity difference of its lobes in the STM image. From this, we conclude that different lobe intensities of a molecule might simply be related to structural relaxations of a molecule. Since STM and AFM contrast have a different z-dependence, small structural relaxations could appear in the STM channel while being invisible in AFM contrast, as observed for molecule 1.

In case of adjacent S-type molecules, instabilities can occur, as becomes evident from molecule 3. In the upper half of the image, one ring of the perylene unit is strongly relaxed away from the surface and an additional spherical feature, probably originating from an anhydride's oxygen, can be observed. After imaging approximately half of the molecule, it switched to a configuration where the other ring close to the same anhydride unit strongly relaxes upwards.

In general, there seems to be a smooth transition between almost symmetrical to strongly asymmetrical relaxations in singly-switched molecules and the degree of asymmetry seems to be influenced by the specific environment of a molecule.

Molecule 4 represents a D-type molecule. The vertical relaxations of the D-type molecule seem to be smaller than the relaxations of S-type molecules since it appears less bright in the AFM images. Further, there is a darker halo close to both anhydride groups. In the STM image, the D-type molecule can be identified by the absence of tunneling current at the given imaging conditions (imaging in constant-height mode at 1.6 V), due to a larger energetic shift of its LUMO resonance (see section 7.5.2).

In order to give more insight into the role of environmental influences in the relaxations and the mutual interaction between adjacent molecules, a set of AFM images is shown in Fig. 7.8, where select molecules had been switched after each image. In Fig. 7.8a, there are four S-type molecules. Whereas the two S-type molecules, located top and bottom of the island (symmetric environment) relax symmetrically, the two adjacent S-type molecules (asymmetric environment) undergo asymmetric relaxations with respect to the long molecular axis.

After switching a close-by molecule (see dashed square in Fig. 7.8b), one PTCDA molecule relaxes differently, and another molecule toggles between different geometries during imaging. After switching a further molecule (Fig. 7.8c), two S-type molecules rapidly toggle between two different geometries. The fact that the symmetry of relaxations within a S-type molecule and the occurrence of toggling depend on the environment, both implies a mutual interaction of switched molecules. Such a mutual interaction could, for example, originate from repulsive interactions of excess electrons, which affect the stability of certain configurations in presence of the tip.

To clarify whether there is an upper limit for the number of switched molecules, the same island was imaged at V = 4.2 V to efficiently switch as many molecules as possible. Subsequently, the island was also imaged at V = -3.5 V to find out whether molecules can be switched back to P-state, which did not change the number of switched molecules but only caused switching of other molecules instead. Fig. 7.8d shows an AFM image after this procedure. A comparison to the corresponding STM image (not shown) suggests that the molecules within the central part of the island (along the red trace) appear to be P-type, whereas the majority of molecules in the periphery are S-type or D-type. This implies that the presence of switched molecules

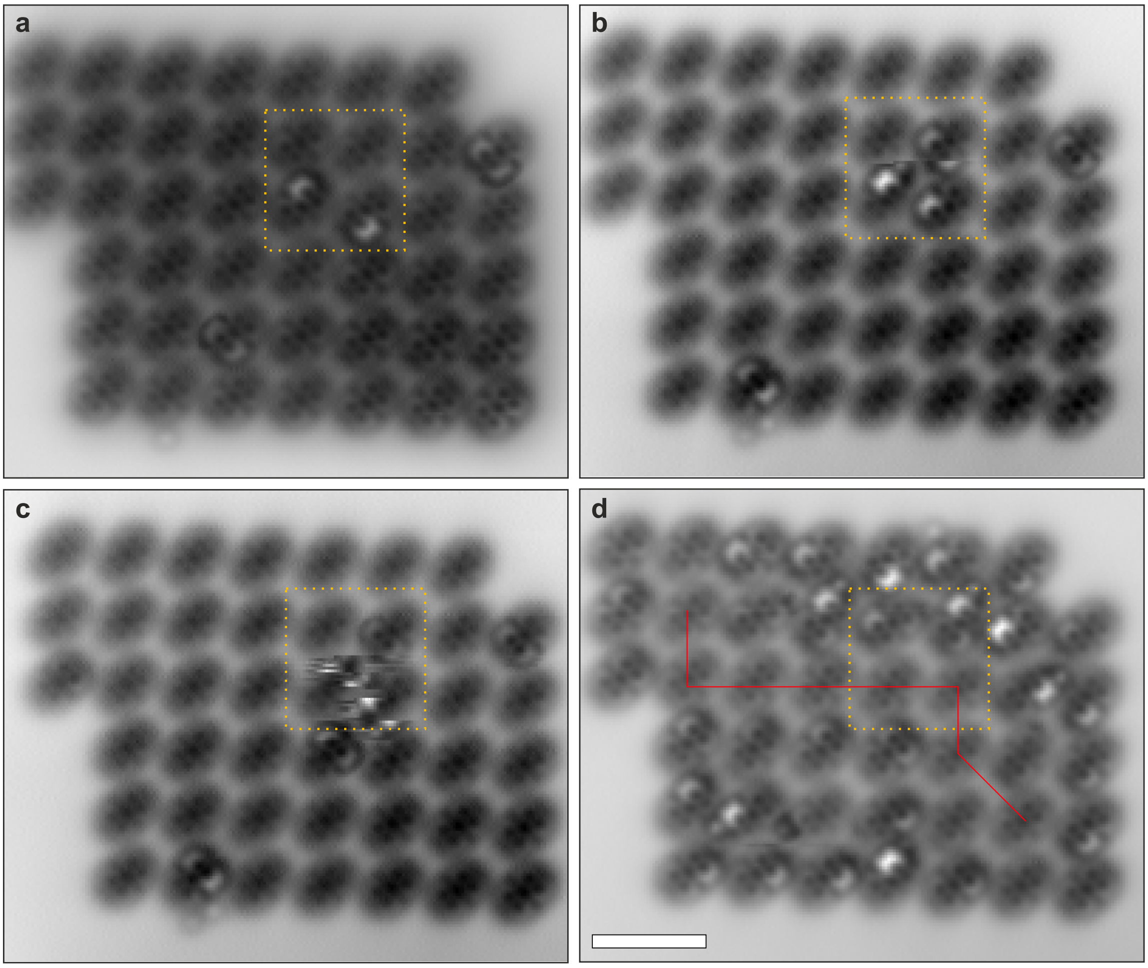

Figure 7.8: Series of AFM images of a PTCDA island where further molecules have been switched in between each image. All the images were acquired with CO tips. The scale bar corresponds to 20 Å. Grayscales are omitted for clarity. The dashed yellow square highlights four specific molecules in each image. The red trace in **d** highlights molecules, which appear to be P-type. All images were acquired at constant height with z-offset with respect to the setpoint. (setpoint: 2.8 pA, 50 mV **a,b**, 35 mV **c**, 80 mV **d**; zoffset: 1.5 Å(**a**), 2.75 Å(**b**), 1.85 Å(**c**), 2.3 Å(**d**.), amplitude 0.5 Å)

within an island impedes switching of further molecules and hence it might not be possible to switch all molecules within and island.
At this stage, our observations indicate that the switching could be attributed to the localization of an excess electron at one of the outer oxygens of an anhydride group, which results in a relaxation of the perylene core.

7.4.5 Further observations

Finally, some additional observations that were made during the experiments are summarized.
Typically, switching was not observed for bias voltages below $V \approx 2.7\,\mathrm{V}$, and in most cases, the molecule directly beneath the tip could be switched. Even at sufficiently large voltages, the switching sometimes occurred for pulse durations in the order of tens of seconds at currents of $I \approx 10\,\mathrm{pA}$. Furthermore, it seemed that the threshold bias voltage for switching increased in the presence of already switched molecules.
In most cases, the targeted molecule could be switched, however sometimes also a neighboring molecule switched instead.
In order to better understand how the switching efficiency depends on the current or the field in the junction, a statistical analysis of the switching is required, for example by measuring the switching rate with respect to the tip-sample distance [7, 181].
However, the non-reversibility makes a statistical analysis complicated because of the different environment and size of individual islands. Such an analysis would be further impeded by adjacent switched molecules, as they seem to influence the threshold voltage for switching.

In summary, switching of PTCDA molecules was investigated with various SPM techniques. STS-measurements have shown that the LUMO resonance of PTCDA shifts to significantly larger voltages upon switching. KPFS measurements indicated a local change in LCPD close to an anhydride group of an S-type molecule, in line with an additional negative charge at the surface. Further, we found that the switching is accompanied by structural relaxations within molecules. Also, mutual interactions of adjacent molecules could be observed. All those results could indicate that the observed switching is related to charging of a molecule, probably due to stabilization of an excess electron at an oxygen of the anhydride group.

7.5 Switching of individual PTCDA molecules

The previous experiments on switching PTCDA molecules within islands, mainly, allowed to gain valuable information on the structural relaxations within PTCDA molecules upon switching. For a deeper understanding of the switching mechanism, also the electronic properties have to be investigated in more detail. Further, it is not a priori clear whether individual molecules can also be switched or whether the switching relies on an interaction between molecules within self-assembled islands.
To this end, similar STM and AFM measurements were conducted for individual PTCDA molecules on NaCl(2ML)/Au(110). Specifically, the electronic structure of individual PTCDA molecules before and after switching will be discussed. Further, the accompanying geometrical changes upon switching are analyzed. Finally, a mechanism for the origin of the switching is proposed that accounts for both, the switching of single molecules and molecules within PTCDA islands.

7.5.1 Determination of the charge state

Figure 7.9a shows an STM image of a pristine PTCDA molecule. The corresponding dI/dV spectrum recorded at the position of the orange dot shows two peaks, one at positive sample voltage $V \approx 0.64\,\mathrm{V}$ and one at negative sample voltage $V \approx -2.03\,\mathrm{V}$ (see Fig. 7.9b). dI/dV images recorded at the two resonances (Figs. 7.9c,d) show similar contrast and are attributed to the LUMO of PTDCA [148, 158, 159]. For comparison, another dI/dV spectrum is shown in blue in Fig. 7.9, which was acquired for a different PTCDA molecule under comparable conditions. This shows that the positions of the dI/dV peaks at positive sample voltage differ by $\approx 100\,\mathrm{mV}$. Notably, the peaks at negative polarity are shifted by $\approx 0.9\,\mathrm{V}$ with respect to each other.

The observation of the same orbital at positive and negative sample voltage often indicates that a given molecule is singly negatively charged, with the two resonances corresponding to the singly occupied- and singly unoccupied molecular orbitals (SOMO, SUMO) of PTCDA, separated by the Coulomb charging energy [49, 157, 159]. It is known that peak positions can slightly shift for different tips or due to environmental effects. However, the position of the dI/dV peak at negative sample voltages seems to be much more affected by the experimental conditions (i.e. tip shape, environmental effects, and tip-sample distance). This large difference in peak positions, at negative sample voltage, for different molecules suggests that the peak, observed at negative sample voltage, might be attributed to bipolar tunneling [24, 159]. In this case, both peaks would correspond to tunneling through the same state, which is pulled below the Fermi level of the substrate upon applying a negative sample voltage.
The principle of bipolar tunneling is visualized in Fig. 7.10a,b. In a double-barrier tunneling junction, a part of the applied bias voltage drops across the insulating NaCl barrier. At positive sample voltage (Fig. 7.10a), tunneling through the LUMO primarily depends on the alignment of the chemical potential of the tip to the LUMO

(the voltage drop in the NaCl layer causes only a minor energetic level shift). However, to tunnel through the LUMO at negative sample voltage, the voltage drop in the NaCl is required to pull the LUMO below the chemical potential of the sample. This leads to a peak in tunneling conductance from the same orbital at both polarities.

To clarify whether the peak at negative bias voltage originates from bipolar tunneling, the peak positions from 23 spectra, recorded for six different molecules, were extracted and are shown as a correlation plot in Fig. 7.10a. This reveals a linear dependence with a slope of ≈ -8 in qualitative agreement with Wu et al. [24]. This means that the peak at negative sample voltage shifts eight times stronger than the peak at positive sample voltage, being a strong indication for bipolar tunneling. If the peaks corresponded two distinct states, instead, the energetic shifts would be similar (i.e. slope 1). Furthermore, this slope allows estimating the ratio of voltage drop in the vacuum gap and the NaCl layer V_{NaCl}/V_{vac} to be ≈ 0.1. From dI/dV measurements of Cl^- vacancies, the voltage drop in bilayer NaCl was reported to be a few percent [25], for comparison.

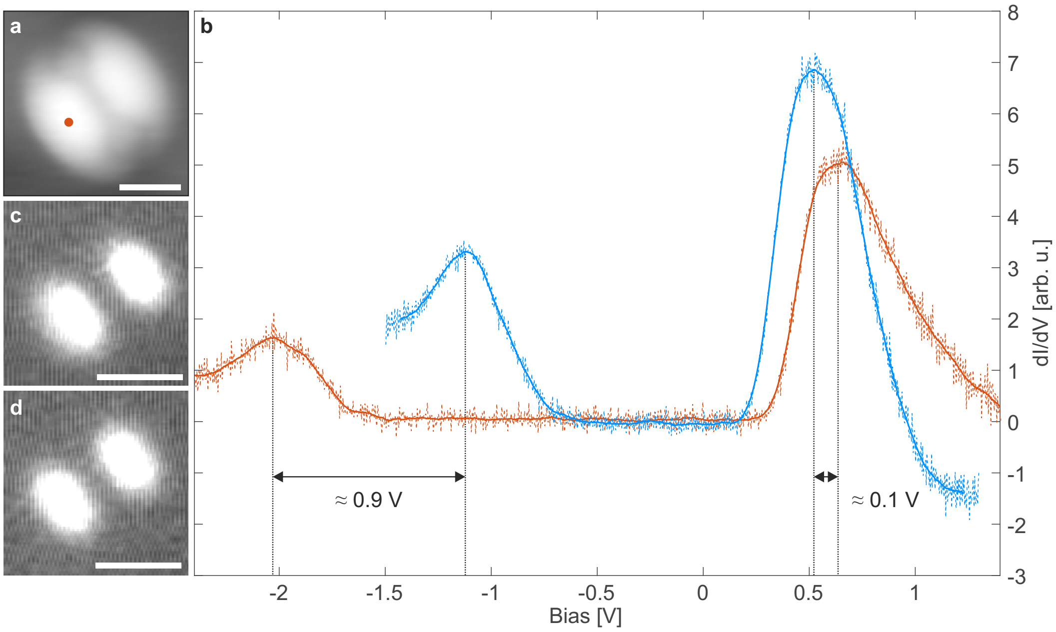

Figure 7.9: **a** Constant-current STM image of an individual pristine PTCDA molecule. **b** dI/dV spectra of the molecule in **a** (orange) and of another pristine PTCDA molecule (blue). Raw data are plotted dashed and smoothened data shown as solid lines. The dotted vertical lines mark the positions of the dI/dV maxima. **c, d** dI/dV images of the molecule shown in **a** at the two resonances (V = -2.10 V in **c** and V = 0.60 V in **d**, setpoint: $I = 1.8\,\text{pA}$, $V = 0.93\,\text{V}$, modulation voltage $V_{pp} = 30\,\text{mV}$, modulation frequency $f = 185\,\text{Hz}$).

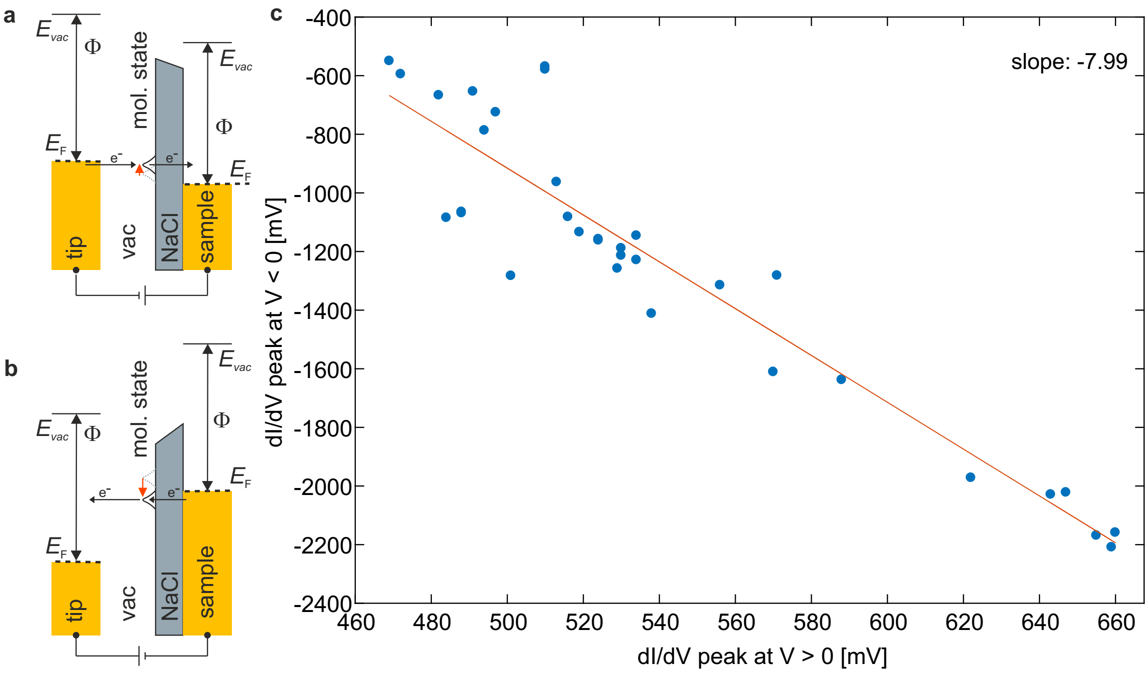

Figure 7.10: Schematic picture of conventional resonant tunneling through an unoccupied state **a** and bipolar tunneling **b**: for sufficiently large negative sample voltage the formerly unoccupied state is shifted below the Fermi level of the substrate by the fraction of voltage that drops in the NaCl film (or lever arm [182]). The initial level position at $V = 0\,\mathrm{V}$ is shown in dashed grey. The red vertical arrows indicate the level shift by the lever arm. **c** Correlation of the dI/dV resonance at positive and negative sample voltage. Each data point corresponds to an individual measurement.

Due to the low relative voltage drop of $\approx 10\,\%$ in the NaCl film it becomes apparent that the LUMO has to be close to the Fermi level of the substrate in order to enable bipolar tunneling. If PTCDA was singly negatively charged here, one would expect an additional peak at negative bias voltage, which corresponds to the SOMO. Furthermore, for Cu(111) as supporting conductive substrate, which has a significantly smaller work function than Au(110) ($\Phi_{Cu(111)} = 4.94\,\mathrm{eV}$, $\Phi_{Au(110)} = 5.37\,\mathrm{eV}$ [154]) PTCDA was reported to be singly negatively charged [159], whereas for Au(111) ($\Phi_{Au(111)} = 5.31\,\mathrm{eV}$ [154]) PTCDA was reported to be neutral [158].[1] Hence, we infer PTCDA, adsorbed on NaCl/Au(110), to be neutral and attribute the peak at negative sample voltage to bipolar tunneling.

---

[1] One would expect that the work function is largest for the closest packed surface, which does not seem to be the case for Au. This might come from the fact that both surfaces reconstruct [151, 183].

7.5.2 Changes in the electronic structure of PTCDA upon switching

Figure 7.11a shows an STM image of two individual PTCDA molecules taken in constant current mode. After the tip was positioned above the left molecule, the feedback loop was switched off and a voltage of $V = 3.1\,\mathrm{V}$ was applied until a sharp drop in tunneling current occurred, indicating a possible switching event of the molecule (Fig. 7.11b). A subsequent STM image of the same molecules (Fig. 7.11c) confirms that the left molecule has been switched from P-state to the S-state. The S-type molecule appears fuzzy and has lower apparent height than the P-type molecule.[2] Furthermore, a depression-like feature can be observed at the position of the anhydride group, at which the switching event was induced.

A further voltage pulse ($V = 3.1\,\mathrm{V}$) above the S-type molecule (red dot in Fig. 7.11d) demonstrates that a second switching event (from S- to D-state) can be induced in a single PTCDA molecule, in agreement with the occasionally observed doubly switching of molecules within PTCDA islands. Upon switching a second time, both anhydride groups appear as depressions. Also, the molecule changed its adsorption

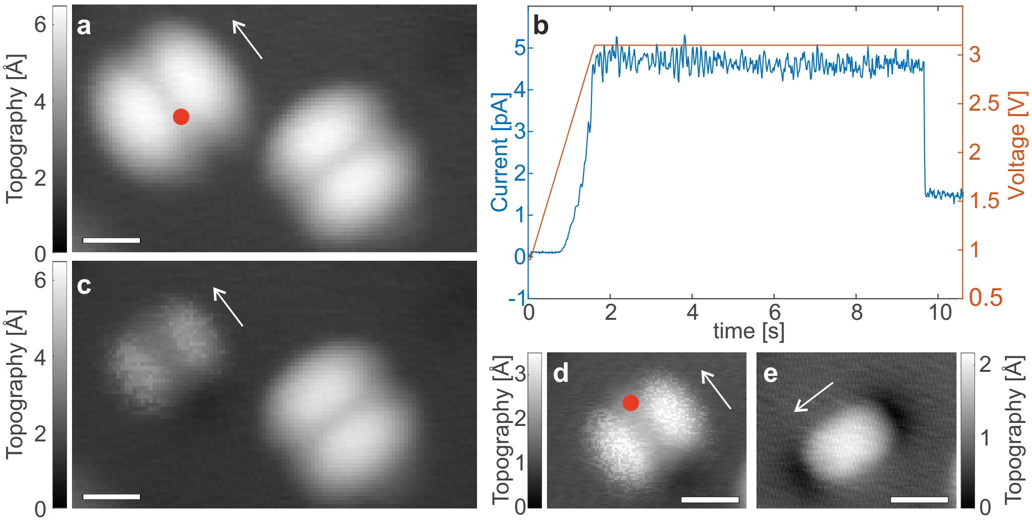

Figure 7.11: **a** STM image of two individual PTCDA molecules. **b** $I(t)$-trace above the left molecule (position indicated by the red dot in **a**), where the voltage is increased to 3.1 V. After ≈ 10 s a sharp drop in tunnel current occurs. **c** STM image of the same molecules after switching. STM images before **d** and after **e** switching the left molecule a second time. White arrows indicate the direction of the long molecular axis for the left molecule (Setpoint: I = 1.2 pA, V = 0.93 V, z-offset = 1.7 Å in **b**.)

---

[2] Note that the constant-current images of individual molecules were acquired at a smaller bias voltage ($V = 0.93\,\mathrm{V}$) than the previously shown constant-height images of the islands, to better distinguish between, P- and S-type molecules in constant-current images. In consequence, a molecule appears less bright after switching.

position and rotated by 90°. In general, molecules became less stable and sometimes moved on the surface during imaging. In most cases, the S-type molecules appeared asymmetric, with a brighter contrast on one of the two lobes, as was also observed for S-type molecules in PTCDA islands. Further, it was observed that a molecule can directly switch twice (from P- to D- state).

To gain further insight into the switching mechanism, dI/dV measurements were acquired for the same molecule before and after switching, which are shown in Fig. 7.12. The pristine molecule shows two dI/dV peaks, a sharp one at $\approx$ 0.5 V and a broad one around $\approx$ -1.2 V, due to bipolar tunneling [24] (Figs. 7.12a,b). dI/dV images at corresponding voltages reveal an identical dumbbell-shape orbital for both reso-

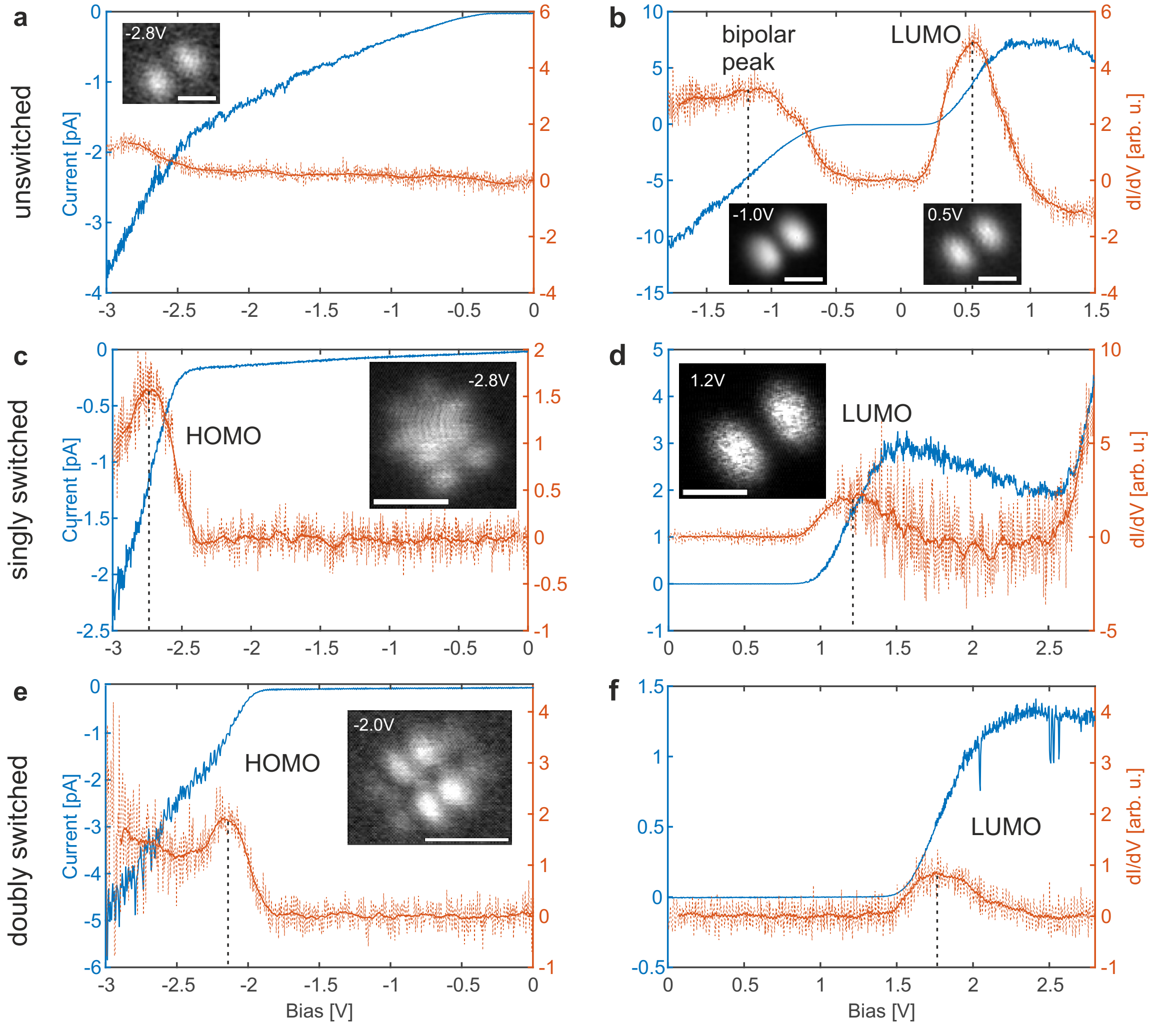

Figure 7.12: dI/dV- (orange) and $I(V)$-measurements (blue) of a single PTCDA molecule in P-sate (a,b), S-sate (c,d), and D-sate (e,f). The insets show dI/dV-images at the corresponding peaks. All scale bars correspond to 10 Å.

nances, which is attributed to the LUMO. The faint *dI*/*dV* peak at ≈-2.8 V could also be observed in the background spectra and hence is attributed to a tip state. The fact that the *dI*/*dV* image at -2.8 V has a faint LUMO-like appearance, gives further confidence that this peak does not correspond to a different occupied state. Figure 7.12c,d show *dI*/*dV* spectra of the molecule in the *S* state. A sharp resonance emerged at -2.8 V, and the corresponding *dI*/*dV* image has some resemblance to the HOMO of PTCDA (see also chapter 6, Fig. 6.3) [158]. For different molecules, we observed relative intensity variations of the eight HOMO lobes. As will be shown in the following, individual PTCDA also undergoes vertical relaxations upon switching, and hence different lobe intensities might simply be attributed to different vertical relaxations of PTCDA. The dI/dV image corresponding to the peak at positive voltage (≈ 1.2 V) has the same dumbbell shape as observed for pristine molecules and is therefore attributed to the LUMO. Notably, the spectra indicate an energetic shift of the LUMO by ≈ 0.6 eV.

After switching twice (Figs. 7.12e,f), both the HOMO and LUMO resonance shift towards higher bias voltages but apart from the different lobe intensities, the observations remain similar. The relative peak shifts (≈ 0.6 V) seem to be comparable with the shift upon singly switching. For this specific molecule, we could not obtain a *dI/dV* image in the *D*-state, because it frequently moved at resonant tunneling conditions. However, *dI/dV* images of another *D*-type molecule confirm that this resonance can be attributed to the LUMO of PTCDA. Before switching the left molecule from *S*- to *D*-state, the tip was functionalized with a CO molecule. Apart from an increased contrast, dI/dV spectra and images of the singly-switched molecule yielded the same results with both tips. Those findings agree with measurements of other individual PTCDA molecules.

7.5.3 Structural changes of individual PTCDA upon switching

Figure 7.13 shows a sequence of STM and AFM images of two close-by PTCDA molecules in different states, recorded with a CO-functionalized tip. The STM images allow us to determine the state of a molecule, and thereby enable us to relate and compare AFM contrast of molecules in different states. Importantly, all images show the same two molecules. The different distances between the two molecules are attributed to, either, a molecule changing its adsorption position upon switching, a movement during data acquisition, or a controlled lateral manipulation of a molecule.

Figure 7.13a shows an STM image of two molecules, being in *S*- and *P*-state, respectively. The corresponding AFM image reveals that the molecule in the *S*-state appears brighter than the one in the *P*-state, indicating a relaxation of the molecule away from the surface upon switching (see Figs. 7.13a,b). Further, the *S*-type molecule appears brighter at the bottom-left part of the perylene unit, indicating a slightly asymmetric relaxation. The fact that the *P*-type molecule does not show an asymmetry rules out asymmetric imaging properties related to the tip or an incorrect plane subtraction.

The *D*-type PTCDA molecule appears to relax even more away from the substrate, as can be concluded from a comparison of the *D*-type- to the *P*-type molecule (Figs. 7.13c,d) and the *S*-type molecule (Figs. 7.13e,f). Whereas the AFM contrast of the *P*-type molecule's perylene unit is almost homogeneous - the four outer rings are fully visible at a moderate contrast of the central ring - there seems to be a faint difference for the switched molecules (most clearly for the *D*-type molecule in Fig. 7.13j, where only the peripheral part of the four outer rings is visible). Furthermore, those

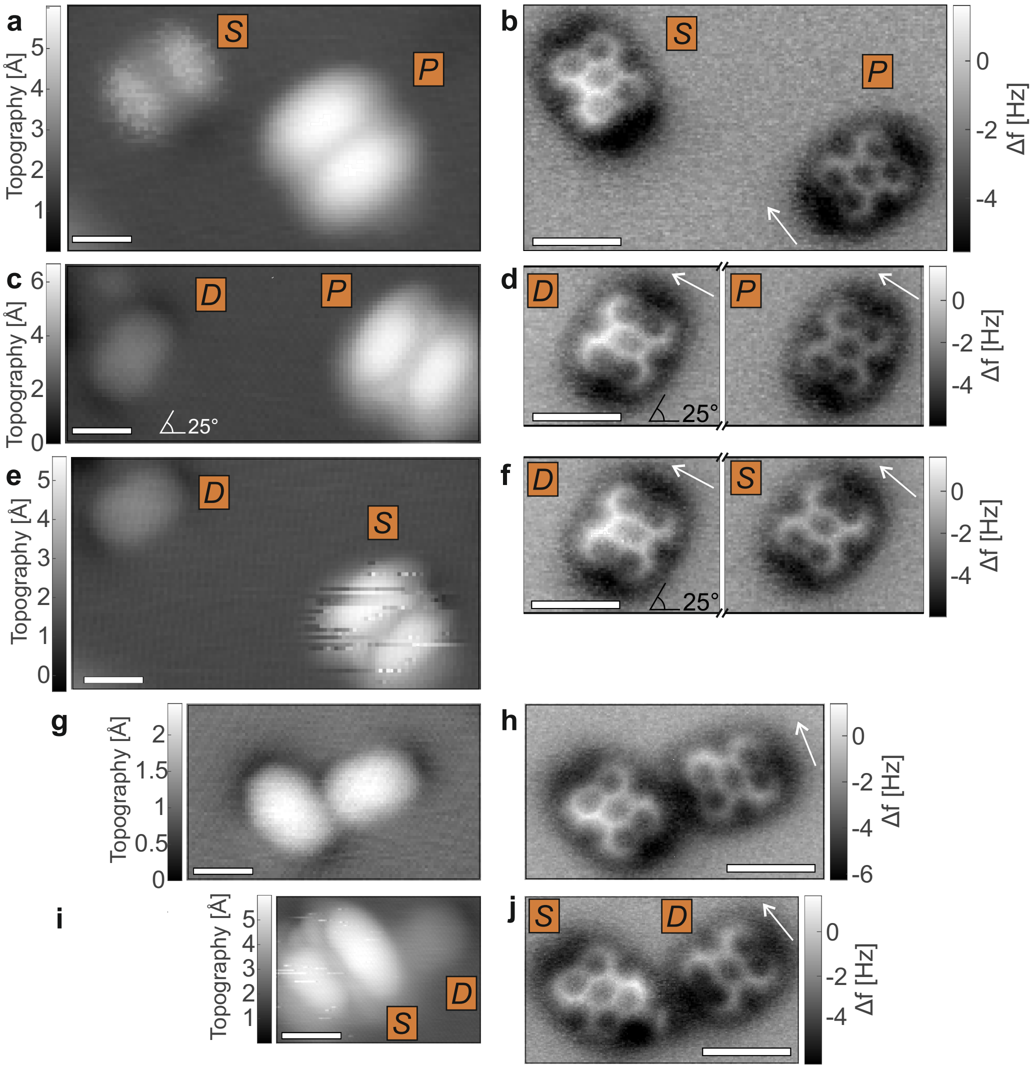

Figure 7.13: Comparison of STM **a,c,e,g,i** and AFM images **b,d,f,h,j** of two individual PTCDA molecules in different switching states. *P, S*, and *D* indicate that a molecule is in *P*-, *S*-, or *D*-state, respectively. The scan plane was rotated counterclockwise by 25° in **c-f** to reduce AFM data acquisition time. The white arrows indicate the direction of the short molecular axis.

images indicate that, for switched molecules, the central ring of the perylene unit appears more distorted (i.e. elongated) in direction of the short molecular axis.
It was found that especially *D*-type molecules are very mobile, which has been utilized to laterally manipulate the left molecule close towards the right one (see Figs. 7.13g,h) [184]. To this end, the tip was placed at the edge of the molecule, opposite to the side the molecule was intended to move, and the voltage was ramped up with open feedback loop until a sharp step in the current was observed. Even though both molecules appear in-gap like in the STM image, indicating that both molecules had become *D*-type after the manipulation, subsequent images indicate that the left molecule is *S*-type, and the right one *D*-type, instead (Figs. 7.13i,j). So far, reverse switching of a single molecule (from *D*- to *S*-state or *S*- to *P*-state) could not be achieved, but experiments on PTCDA islands demonstrated that switching other molecules instead, is possible. Hence, it is likely that Figs. 7.13g,h shows one molecule being in *S*-state, the other being in *D*-state. The fact that both molecules have an in-gap appearance is inferred to be caused by gating. Such gating effects were observed for the case of local charges in close vicinity [99, 100, 170], suggesting that the switching involves a charging of PTCDA.
Further, those images reveal that the angular alignment with respect to the NaCl substrate can change upon switching. Such differences in the adsorption geometry might affect the vertical relaxations of a molecule, additionally.

7.6 Proposed mechanism for the switching of PTCDA

In this section, a tentative model for the physical mechanism behind the observed switching of PTCDA is proposed. The suggested mechanism is based on the observations in STM and AFM data of single molecules and molecular islands, presented in this chapter. Before introducing the model, the key observations of those experiments are briefly summarized:

In molecular islands...

- Switched molecules undergo structural relaxations. Depending on their environment, these relaxations appear either symmetric or asymmetric with respect to the long molecular axis.
- Other close-by switched molecules can cause strong asymmetric relaxations, where probably corner oxygens of anhydride groups become visible in the AFM contrast.
- Neighboring switched molecules can cause a switched molecule to toggle between two geometric configurations.
- In *S*-type molecules, one of the anhydride groups within a molecule appears darker in AFM contrast. For *D*-type molecules, both anhydride groups appear darker.

- Typically, switching does not occur below $V \approx 2.7\,\mathrm{V}$.
- Switching causes energy level shifts of PTCDA $> 0.5\,\mathrm{eV}$. Also, the states of neighboring molecules can be shifted, possibly due to gating.
- The switching seems to be irreversible, but molecules can be restored at the cost of switching other molecules within an island.
- Switching a molecule causes a shift in the LCPD, in line with an additional negative charge at the molecule.

For individual molecules...

- Whereas the HOMO is inaccessible for pristine PTCDA, it can be accessed for switched molecules. In general, molecular levels shift upward in energy upon switching.
- AFM images indicate that the perylene core is relaxed upward in *S*-type molecules and further upward more in *D*-type molecules.
- Asymmetries in the relaxations can observed but are more difficult to interpret compared to molecules within islands.
- Molecules in *S*-state and *D*-state are more mobile than in *P*-state, especially *D*-type molecules frequently move during measurements. Molecules often change their adsorption position upon switching from *S*- to *D*-state.
- Gating [99, 100, 170] can be observed if other switched molecules are in close vicinity, which could be a hint for the presence of a local charge.

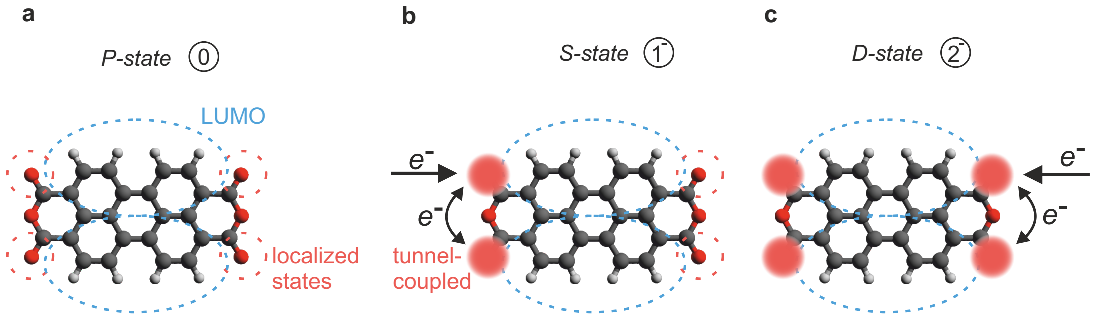

Figure 7.14: Proposed model for the switching mechanism of PTCDA on NaCl/Au(110). **a** Pristine molecule (*P*-state) . **b** PTCDA in *S*-state: an electron is localized at an oxygen of on anhydride group and hence PTCDA is singly negatively charged **c** PTCDA in *D*-state: a further electron is localized at an oxygen of the other anhydride group. PTCDA is now doubly negatively charged. The corresponding charge states are given by the numbers in circles. Occupied states (filled) and unoccupied states (dashed).

Figure 7.14 shows the suggested mechanism behind the switching for an individual PTCDA molecule, based on the above observations. Pristine PTCDA is neutral for this substrate system and its LUMO is indicated as dashed blue dumbbell shape in Fig. 7.14a.

Upon switching once (from *P*- to *S*-state), an electron gets localized at one of the oxygens of one anhydride group, indicated as filled red circles in Fig. 7.14b. Experimental support for the possibility such of a localized charge in PTCDA is provided by a study by Wagner et al. [185]. There they showed that a PTCDA molecule, which was bonded to the tip with one of its corner oxygen atoms, acts as a chargeable atomic-scale quantum dot. This was justified by the fact that the PTCDA frontier orbitals have a low density at the corner oxygens, and hence, the frontier orbitals can be considered as isolated from the tip [185]. In reverse this could also rationalize a charge localization at an oxygen of PTCDA due to the strong interaction with the ionic surface. For symmetry arguments, the two corner oxygens of an anhydride group should have degenerate states for PTCDA adsorbed on a surface.

Furthermore, the low relative distance of the oxygens of $\approx 4\,\text{Å}$ could imply a strong tunnel coupling [116, 170], which could rationalize the fuzzy appearance of switched PTCDA molecules in experiments. Such a model could also explain the asymmetric relaxations of some switched PTCDA molecules in an inhomogeneous environment. For example, another close-by switched (and thus charged) molecule can break the symmetry of the environment, thereby lifting the degeneracy of the two oxygen states. In such a case, the tunnel coupling can be reduced or suppressed, causing less fuzzy imaging and a more asymmetric appearance of molecules in STM and AFM.

In order to stabilize an excess charge in a molecule on a thin insulating substrate, the state has to shift below the Fermi level of the substrate upon occupation. Otherwise, the excess electron would simply escape into the substrate. The fact that switching occurs only at large bias voltages ($\geq 2.7\,\text{V}$) requires a similarly large energetic shift of the localized state due to reorganization energy (polaronic shifts).

For example, the hole reorganization energy for an individual naphthalocyanine molecule on NaCl was determined experimentally and theoretically in the range of 1 eV [60]. A theoretical study by Manke et al. predicts that the more localized a charge is, the larger the reorganization energy is [59]. Considering the strong spatial confinement of an excess electron on an anhydride group's oxygen, compared to being delocalized over the entire molecule, makes a large energetic shift conceivable.

The fact that the degree of spatial charge confinement influences the magnitude of the reorganization energy can qualitatively be also derived from comparison of hysteresis widths in charging experiments of single Au atoms (very local: large hysteresis width of $\approx 1\,\text{V}$ [7, 11, 31]) to CuPc molecules (delocalized over the entire molecule: small hysteresis width of $\approx 0.3\,\text{V}$ [8, 71]). However, it must be noted that the hysteresis width also depends on the tip-sample distance. In fact, the tunneling current, which predominantly determines the data acquisition height, is on the order of few pA in all those charging experiments and hence the experimental conditions should be comparable.

When switching a second time (from *S*- to *D*-state), an oxygen at the other anhydride group also hosts an electron, and the molecule becomes two times negatively charged (Fig. 7.14c). STS of doubly-switched PTCDA reveals a further level shift in line with an additional negative charge. This switching mechanism is considered to be fully analogous for PTCDA within islands. The presence of two excess electrons at one anhydride group seems unlikely because the presence of one electron is expected to raise the energy for adding another charge (i.e. due to Coulomb repulsion) in close vicinity.

Even though the picture of charge stabilization due to polaronic shifts seems to agree with our experimental observations, we can not fully exclude other possible origins for the switching: For example a chemical bond breaking could be induced by the voltage pulses that were used for switching [186–189].
It is conceivable that such a bond breaking could also lead to a change of the charge state. However, the frontier orbitals do not change their occupation upon switching, which makes a charging due to bond breaking improbable.

Further, the question arises, how the vertical relaxations of the perylene unit away from the substrate can be related to a relaxation of oxygen towards the substrate. This could be rationalized as follows: An additional electron at a corner oxygen could possibly change the bond character of the carbon-oxide bond and cause a more sp^3-like (non-planar) bond character of the adjacent carbon. Hence, as the oxygen moves towards the surface, the perylene unit is bent away from the surface.
Further, if the switching is related to charging, one would intuitively expect that the charges in close-by molecules are located as far as possible from each other. Based on the observed molecular relaxations within islands in Fig. 7.8a, this would indicate that the charge is located at the side, where the perylene united relaxes most away from the surface. In contrast, in molecules that relax strongly asymmetric, it appears as if the corner oxygen becomes visible in AFM images, which seems to contradict the above argument of a change in bond character. However, mutual interactions between molecules and the accompanied relaxations might be more complex. Therefore, no clear answer can be given on where the charge is located and how this relates to the observed relaxations.

7.7 Conclusion

In this chapter, we investigated the switching of PTCDA on thin films of NaCl on Au(110) by means of STM and AFM.

The observed changes in the electronic structure, as well as the structural relaxations and local variations of the work function upon switching, suggest that the switching is the result of a charge transfer. Also, we observed mutual interactions between switched molecules, which could support the interpretation of the switching as charging.

A novel mechanism was proposed, namely the stabilization of an excess charge in a strongly confined state by coupling to substrate phonon modes (polaron formation). Those results could shed new light on the role and strength of polaronic shifts at the atomic scale. To test our hypothetical interpretation, density functional theory (DFT) calculations would be required, to quantify the reorganization energy and to elucidate the detailed intermolecular structural relaxations, for example.

8 Summary

In this thesis, various experiments on charging individual molecules and molecules within molecular islands have been presented. Those experiments allowed us to gain valuable insights into changes in the electronic structure and the geometric structure upon charging. Also, those results shed light on the role of reorganization energy in electron transfer rates and the stability of specific charge states.

In chapter 4, AFM experiments on charging individual copper(II)-phthalocyanine molecules, adsorbed on a thin NaCl film on Cu(100), were presented.
Making use of their charge bistability on this substrate system, CuPc molecules were imaged in distinct charge states. We found that the contrast of CuPc in AFM images changes upon charging with a single electron. We highlighted this contrast differences by subtracting AFM images of molecules in the neutral state from AFM images of the same molecules, being singly negatively charged. The observed contrast differences indicated an inhomogeneous vertical relaxation of the molecule upon charging.
To gain more insight into the detailed relaxations, AFM images were simulated based on DFT-calculated geometries of the charged and neutral molecule. A comparison of experimental difference images to simulated difference images in different height regimes showed a good agreement.
The calculated geometries corresponding to the neutral and anionic state confirmed that the molecule undergoes an inhomogeneous vertical relaxation upon charging, where the central unit relaxes towards the surface and the Cu ligand relaxes away from the surface. The relaxations af the periphery of the molecule were negligible.
Interestingly, we found that the contrast change in AFM images originates primarily from the geometrical relaxation of the molecule, caused by the interaction of the charged molecules with the polar surface, whereas the electrostatic contribution itself to the AFM contrast seems to have only a minor influence on the image contrast.
Further, those experiments demonstrated that AFM is capable of resolving structural relaxations of a single molecule at the pm scale.

In chapter 6, our results on the investigation of self-assembled PTCDA islands in different charge states, by means of AFM, were presented. Those self-assembled islands were grown on a $> 20\,\mathrm{ML}$ thick NaCl layer in order to prevent charge transfer to the supporting conductive substrate.
We characterized the spatial dependent charging and discharging of a molecular island. We observed that the injection of an electron gives rise to spatial signatures in the dissipation of the AFM cantilever. We found that this dissipation originates from a intermolecular charge transfer, which is coupled to the oscillatory motion of

the tip. This occurrence of dissipation provided experimental access to study the charge transfer in electrically isolated well-defined atomic-scale structures.

To this end, we imaged islands in distinct charge states. These images revealed that tip-driven intermolecular charge transfer occurs in most of the charge states, but in specific charge states the electron distributions within the island can be stable. A model allowed us to calculate the energies of the possible electron distributions for different charge states of a specific island, with and without the influence of the tip. Based on this model, we simulated the electron distributions within the island, in the presence of the tip. The results, obtained from the model, confirmed our interpretation of the increased dissipation due to tip-induced intra-island charge transfer, and the simulations could rationalize the observed dissipation patterns.

Moreover, the fit parameters in the model provide us with values for the screening of charges at the atomic scale.

Finally, we derived the approximate tunneling rate of this intermolecular charge transfer. The tunneling rates were found to be on the order of $2 \cdot 10^5\,\mathrm{Hz}$, which is very low, considering the small intermolecular distances within the self-assembled islands. The small rate was interpreted as the large tunnel coupling being modified by polaronic effects. This finding highlights the role of reorganization energy on the conductance in organic materials.

Notably, those results also provided insight into the distribution of excess electrons in self-assembled islands in different charge states, and how the interplay of relative molecular level alignment and mutual charge interactions affect the stability of electron distributions within an island.

In future experiments, one could exploit the charge multistability of metal atoms on an insulating surface [31, 51] and use them as switchable external gates [99, 100]. This opens up the possibility to systematically study the role of external influences on the distribution of excess electrons within a charged island.

Furthermore, such molecular structures could be used as building blocks for quantum cellular automata [168].

In chapter 7, STM and AFM experiments on individual PTCDA molecules and self-assembled islands of PTCDA on ultrathin NaCl films were presented. For both cases, we found that molecules can be switched by applying voltage pulses and that a molecule can be switched up to two times.

We observed that this switching leads to changes in the electronic properties and geometric rearrangements of a molecule. It was found that the dI/dV peaks of molecules shift by $> 0.5\,V$ to larger voltages per induced switching event, and that switched molecules might gate the levels of neighboring molecules.

Further, we observed that the molecules undergo structural relaxations upon switching. The observed contrast changes in AFM images indicate that the relaxations can be quite inhomogeneous and depend on the environment of a molecule.

Also, we observed mutual interactions between switched molecules, which appeared to influence the geometric relaxations of molecules, and could lead to the toggling of a molecule between two relaxation configurations.

Based on these observed changes in the electronic properties, the molecular geometry, and mutual interactions between molecules, we suggest that the molecules can be charged upon applying voltage pulses, and the switching is the signature of the charge state transition.

In contrast to other studies of charging single molecules [8, 48–50], our results indicate that the charge does not occupy the delocalized LUMO but seems to be localized at an anhydride group. We suggest that the charge can be stabilized there, due to a large polaronic shift, arising from the strong spatial confinement of the excess charge.

Bibliography

[1] G. Binnig, H. Rohrer, C. Gerber, and E. Weibel. *Surface Studies by Scanning Tunneling Microscopy.* Physical Review Letters **49**, 57–61 (1982).

[2] G. Binnig, C. F. Quate, and C. Gerber. *Atomic Force Microscope.* Physical Review Letters **56**, 930–933 (1986).

[3] D. M. Eigler and E. K. Schweizer. *Positioning single atoms with a scanning tunnelling microscope.* Nature **344**, 524–526 (1990).

[4] B. C. Stipe, M. A. Rezaei, and W. Ho. *Single-Molecule Vibrational Spectroscopy and Microscopy.* Science **280**, 1732–1735 (1998).

[5] S. Li, A. Yu, F. Toledo, Z. Han, H. Wang, H. Y. He, R. Wu, and W. Ho. *Rotational and Vibrational Excitations of a Hydrogen Molecule Trapped within a Nanocavity of Tunable Dimension.* Physical Review Letters **111**, 146102 (2013).

[6] J. Repp, G. Meyer, S. M. Stojković, A. Gourdon, and C. Joachim. *Molecules on Insulating Films: Scanning-Tunneling Microscopy Imaging of Individual Molecular Orbitals.* Physical Review Letters **94**, 026803 (2005).

[7] J. Repp, G. Meyer, F. E. Olsson, and M. Persson. *Controlling the charge state of individual gold adatoms.* Science **305**, 493–495 (2004).

[8] I. Swart, T. Sonnleitner, and J. Repp. *Charge State Control of Molecules Reveals Modification of the Tunneling Barrier with Intramolecular Contrast.* Nano Letters **11**, 1580–1584 (2011).

[9] L. Gross, F. Mohn, N. Moll, P. Liljeroth, and G. Meyer. *The Chemical Structure of a Molecule Resolved by Atomic Force Microscopy.* Science **325**, 1110–1114 (2009).

[10] L. Gross, F. Mohn, N. Moll, B. Schuler, A. Criado, E. Guitián, D. Peña, A. Gourdon, and G. Meyer. *Bond-Order Discrimination by Atomic Force Microscopy.* Science **337**, 1326–1329 (2012).

[11] L. Gross, F. Mohn, P. Liljeroth, J. Repp, F. J. Giessibl, and G. Meyer. *Measuring the Charge State of an Adatom with Noncontact Atomic Force Microscopy.* Science **324**, 1428–1431 (2009).

[12] S. Fatayer, F. Albrecht, Y. Zhang, D. Urbonas, D. Peña, N. Moll, and L. Gross.

Molecular structure elucidation with charge-state control. Science **365**, 142–145 (2019).

[13] J. V. Barth, G. Costantini, and K. Kern. *Engineering atomic and molecular nanostructures at surfaces.* Nature **437**, 671–679 (2005).

[14] W. Steurer, S. Fatayer, L. Gross, and G. Meyer. *Probe-based measurement of lateral single-electron transfer between individual molecules.* Nature Communications **6**, 8353 (2015).

[15] P. Rahe, R. P. Steele, and C. C. Williams. *Consecutive Charging of a Molecule-on-Insulator Ensemble Using Single Electron Tunnelling Methods.* Nano Letters **16**, 911–916 (2016).

[16] G. Binnig, H. Rohrer, C. Gerber, and E. Weibel. *Tunneling through a controllable vacuum gap.* Applied Physics Letters **40**, 178–180 (1982).

[17] G. Binnig and H. Rohrer. *Scanning tunneling microscopy.* Surface Science **126**, 236–244 (1983).

[18] F. Schwabl. *Quantenmechanik.* Springer-Verlag Berlin Heidelberg, 7. edition (2007).

[19] G. Münnich. *Cross-Sectional Scanning Probe Microscopy on GaAs: Tip-Induced Band Bending, Buried Acceptors and Adsorbed Molecules.* Ph.D. thesis, Universität Regensburg (2014).

[20] C. J. Chen. *Introduction to Scanning Tunneling Microscopy.* Oxford University Press, New York, 2. edition (2008).

[21] J. Bardeen. *Tunnelling from a Many-Particle Point of View.* Physical Review Letters **6**, 57–59 (1961).

[22] J. Tersoff and D. R. Hamann. *Theory and Application for the Scanning Tunneling Microscope.* Physical Review Letters **50**, 1998–2001 (1983).

[23] J. Tersoff and D. R. Hamann. *Theory of the scanning tunneling microscope.* Physical Review B **31**, 805–813 (1985).

[24] S. W. Wu, G. V. Nazin, X. Chen, X. H. Qiu, and W. Ho. *Control of Relative Tunneling Rates in Single Molecule Bipolar Electron Transport.* Physical Review Letters **93**, 236802 (2004).

[25] J. Repp, G. Meyer, S. Paavilainen, F. E. Olsson, and M. Persson. *Scanning Tunneling Spectroscopy of Cl Vacancies in NaCl Films: Strong Electron-Phonon Coupling in Double-Barrier Tunneling Junctions.* Physical Review Letters **95**, 225503 (2005).

[26] F. J. Giessibl. *The qPlus sensor, a powerful core for the atomic force microscope.* Review of Scientific Instruments **90**, 011101 (2019).

[27] F. J. Giessibl. *Forces and frequency shifts in atomic-resolution dynamic-force microscopy.* Physical Review B **56**, 16010–16015 (1997).

[28] F. J. Giessibl. *Advances in atomic force microscopy.* Review of Modern Physics **75**, 949–983 (2003).

[29] T. R. Albrecht, P. Grütter, D. Horne, and D. Rugar. *Frequency modulation detection using high-Q cantilevers for enhanced force microscope sensitivity.* Journal of Applied Physics **69**, 668–673 (1991).

[30] N. Moll, L. Gross, F. Mohn, A. Curioni, and G. Meyer. *The mechanisms underlying the enhanced resolution of atomic force microscopy with functionalized tips.* New Journal of Physics **12**, 125020 (2010).

[31] W. Steurer, J. Repp, L. Gross, I. Scivetti, M. Persson, and G. Meyer. *Manipulation of the Charge State of Single Au Atoms on Insulating Multilayer Films.* Physical Review Letters **114**, 036801 (2015).

[32] Lord Kelvin. *Contact electricity of metals.* The London, Edinburgh, and Dublin Philosophical Magazine and Journal of Science **46**, 82–120 (1898). Series 5.

[33] S. Sadewasser and T. Glatzel (editors). *Kelvin Probe Force Microscopy*, volume 48, 11–13. Springer Verlag (2011).

[34] P. Samori (editor). *Scanning Probe Microscopies Beyond Imaging.* Wiley-VCH Verlag (2006).

[35] M. Nonnenmacher, M. P. O'Boyle, and H. K. Wickramasinghe. *Kelvin probe force microscopy.* Applied Physics Letters **58**, 2921–2923 (1991).

[36] L. L. Patera, F. Queck, P. Scheuerer, and J. Repp. *Mapping orbital changes upon electron transfer with tunnelling microscopy on insulators.* Nature **566**, 245–248 (2019).

[37] F. Albrecht, J. Repp, M. Fleischmann, M. Scheer, M. Ondráček, and P. Jelínek. *Probing Charges on the Atomic Scale by Means of Atomic Force Microscopy.* Physical Review Letters **115**, 076101 (2015).

[38] F. Mohn, L. Gross, N. Moll, and G. Meyer. *Imaging the charge distribution within a single molecule.* Nature Nanotechnology **7**, 227 (2012).

[39] P. Grutter. *Seeing the charge within.* Nature Nanotechnology **7**, 210 (2012).

[40] H. Hölscher, B. Gotsmann, W. Allers, U. D. Schwarz, H. Fuchs, and R. Wiesendanger. *Measurement of conservative and dissipative tip-sample interaction forces with a dynamic force microscope using the frequency modulation technique.* Physical Review B **64**, 075402 (2001).

[41] C. Lotze, M. Corso, K. J. Franke, F. von Oppen, and J. I. Pascual. *Driving a Macroscopic Oscillator with the Stochastic Motion of a Hydrogen Molecule.* Science **338**, 779–782 (2012).

[42] L. Cockins, Y. Miyahara, S. D. Bennett, A. A. Clerk, S. Studenikin, P. Poole, A. Sachrajda, and P. Grutter. *Energy levels of few-electron quantum dots imaged and characterized by atomic force microscopy.* Proceedings of the National Academy of Sciences **107**, 9496–9501 (2010).

[43] L. Cockins, Y. Miyahara, S. D. Bennett, A. A. Clerk, and P. Grutter. *Excited-State Spectroscopy on an Individual Quantum Dot Using Atomic Force Microscopy.* Nano Letters **12**, 709–713 (2012).

[44] Y. Miyahara, A. Roy-Gobeil, and P. Grutter. *Quantum state readout of individual quantum dots by electrostatic force detection.* Nanotechnology **28**, 064001 (2017).

[45] M. Ondráček, P. Hapala, and P. Jelínek. *Charge-state dynamics in electrostatic force spectroscopy.* Nanotechnology **27**, 274005 (2016).

[46] W. Steurer, J. Repp, L. Gross, and G. Meyer. *Damping by sequentially tunneling electrons.* Surface Science **678**, 112–117 (2018).

[47] R. A. Marcus. *Electron transfer reactions in chemistry. Theory and experiment.* Review of Modern Physics **65**, 599–610 (1993).

[48] S. W. Wu, N. Ogawa, and W. Ho. *Atomic-Scale Coupling of Photons to Single-Molecule Junctions.* Science **312**, 1362–1365 (2006).

[49] S. W. Wu, N. Ogawa, G. V. Nazin, and W. Ho. *Conductance Hysteresis and Switching in a Single-Molecule Junction.* The Journal of Physical Chemistry C **112**, 5241–5244 (2008).

[50] T. Leoni, O. Guillermet, H. Walch, V. Langlais, A. Scheuermann, J. Bonvoisin, and S. Gauthier. *Controlling the Charge State of a Single Redox Molecular Switch.* Physical Review Letters **106**, 216103 (2011).

[51] F. E. Olsson, S. Paavilainen, M. Persson, J. Repp, and G. Meyer. *Multiple Charge States of Ag Atoms on Ultrathin NaCl Films.* Physical Review Letters **98**, 176803 (2007).

[52] C. Schönenberger and S. F. Alvarado. *Observation of single charge carriers by force microscopy.* Physical Review Letters **65**, 3162–3164 (1990).

[53] L. J. Klein and C. C. Williams. *Single electron tunneling detected by electrostatic force.* Applied Physics Letters **79**, 1828–1830 (2001).

[54] R. Stomp, Y. Miyahara, S. Schaer, Q. Sun, H. Guo, P. Grutter, S. Studenikin, P. Poole, and A. Sachrajda. *Detection of Single-Electron Charging in an Individual InAs Quantum Dot by Noncontact Atomic-Force Microscopy.* Physical Review Letters **94**, 056802 (2005).

[55] J. Zhu, M. Brink, and P. L. McEuen. *Frequency shift imaging of quantum dots with single-electron resolution.* Applied Physics Letters **87**, 242102 (2005).

[56] E. Bussmann and C. C. Williams. *Single-electron tunneling force spectroscopy of an individual electronic state in a nonconducting surface.* Applied Physics Letters **88**, 263108 (2006).

[57] B. S. Brunschwig, S. Ehrenson, and N. Sutin. *Solvent reorganization in optical and thermal electron-transfer processes.* The Journal of Physical Chemistry **90**, 3657–3668 (1986).

[58] V. Vaissier, P. Barnes, J. Kirkpatrick, and J. Nelson. *Influence of polar medium on the reorganization energy of charge transfer between dyes in a dye sensitized film.* Physical Chemistry Chemical Physics **15**, 4804–4814 (2013).

[59] F. Manke, J. M. Frost, V. Vaissier, J. Nelson, and P. R. F. Barnes. *Influence of a nearby substrate on the reorganization energy of hole exchange between dye molecules.* Physical Chemistry Chemical Physics **17**, 7345–7354 (2015).

[60] S. Fatayer, B. Schuler, W. Steurer, I. Scivetti, J. Repp, L. Gross, M. Persson, and G. Meyer. *Reorganization energy upon charging a single molecule on an insulator measured by atomic force microscopy.* Nature Nanotechnology **13**, 376–380 (2018).

[61] P. W. Atkins and R. Friedman. *Molecular Quantum Mechanics.* Oxford University Press, New York, 5. edition (2010).

[62] L. L. Patera, F. Queck, P. Scheuerer, N. Moll, and J. Repp. *Accessing a Charged Intermediate State Involved in the Excitation of Single Molecules.* Physical Review Letters **123**, 016001 (2019).

[63] P. Scheuerer, F. Queck, L. L. Patera, and J. Repp. *Bilder von Molekülorbitalen in unterschiedlichen Ladungszuständen.* Physik in unserer Zeit **50**, 110–111 (2019).

[64] F. Queck. *Implementierung der Rastertunnelmikroskopie auf Isolatoren.* Ph.D. thesis, Universität Regensburg (2018).

[65] F. Albrecht, M. Neu, C. Quest, I. Swart, and J. Repp. *Formation and Characterization of a Molecule-Metal-Molecule Bridge in Real Space.* Journal of the American Chemical Society **135**, 9200–9203 (2013).

[66] D. G. de Oteyza, P. Gorman, Y.-C. Chen, S. Wickenburg, A. Riss, D. J. Mowbray, G. Etkin, Z. Pedramrazi, H.-Z. Tsai, A. Rubio, M. F. Crommie, and F. R. Fischer. *Direct Imaging of Covalent Bond Structure in Single-Molecule Chemical Reactions.* Science **340**, 1434–1437 (2013).

[67] F. Albrecht, N. Pavliĉek, C. Herranz-Lancho, M. Ruben, and J. Repp. *Characterization of a Surface Reaction by Means of Atomic Force Microscopy.* Journal of the American Chemical Society **137**, 7424–7428 (2015).

[68] N. Kocić, X. Liu, S. Chen, S. Decurtins, O. Krejčí, P. Jelínek, J. Repp, and S.-X. Liu. *Control of Reactivity and Regioselectivity for On-Surface Dehydrogenative*

Aryl-Aryl Bond Formation. Journal of the American Chemical Society **138**, 5585–5593 (2016).

[69] L. L. Patera, X. Liu, N. Mosso, S. Decurtins, S.-X. Liu, and J. Repp. *Crystallization of a Two-Dimensional Hydrogen-Bonded Molecular Assembly: Evolution of the Local Structure Resolved by Atomic Force Microscopy.* Angewandte Chemie International Edition **56**, 10786–10790 (2017).

[70] F. Queck, O. Krejčí, P. Scheuerer, F. Bolland, M. Otyepka, P. Jelínek, and J. Repp. *Bonding Motifs in Metal–Organic Compounds on Surfaces.* Journal of the American Chemical Society **140**, 12884–12889 (2018).

[71] P. Scheuerer, L. L. Patera, F. Simbürger, F. Queck, I. Swart, B. Schuler, L. Gross, N. Moll, and J. Repp. *Charge-Induced Structural Changes in a Single Molecule Investigated by Atomic Force Microscopy.* Physical Review Letters **123**, 066001 (2019).

[72] N. Pavliček, B. Fleury, M. Neu, J. Niedenführ, C. Herranz-Lancho, M. Ruben, and J. Repp. *Atomic Force Microscopy Reveals Bistable Configurations of Dibenzo[a,h]thianthrene and their Interconversion Pathway.* Physical Review Letters **108**, 086101 (2012).

[73] B. Schuler, W. Liu, A. Tkatchenko, N. Moll, G. Meyer, A. Mistry, D. Fox, and L. Gross. *Adsorption Geometry Determination of Single Molecules by Atomic Force Microscopy.* Physical Review Letters **111**, 106103 (2013).

[74] P. Hapala, G. Kichin, C. Wagner, F. S. Tautz, R. Temirov, and P. Jelínek. *Mechanism of high-resolution STM/AFM imaging with functionalized tips.* Physical Review B **90**, 085421 (2014).

[75] N. Pavliček, C. Herranz-Lancho, B. Fleury, M. Neu, J. Niedenführ, M. Ruben, and J. Repp. *High-resolution scanning tunneling and atomic force microscopy of stereochemically resolved dibenzo[a,h]thianthrene molecules.* physica status solidi (b) **250**, 2424–2430 (2013).

[76] S. K. Hämäläinen, N. van der Heijden, J. van der Lit, S. den Hartog, P. Liljeroth, and I. Swart. *Intermolecular Contrast in Atomic Force Microscopy Images without Intermolecular Bonds.* Physical Review Letters **113**, 186102 (2014).

[77] M. Neu, N. Moll, L. Gross, G. Meyer, F. J. Giessibl, and J. Repp. *Image correction for atomic force microscopy images with functionalized tips.* Physical Review B **89**, 205407 (2014).

[78] H. Mönig, D. R. Hermoso, O. Díaz Arado, M. Todorović, A. Timmer, S. Schüer, G. Langewisch, R. Pérez, and H. Fuchs. *Submolecular Imaging by Noncontact Atomic Force Microscopy with an Oxygen Atom Rigidly Connected to a Metallic Probe.* ACS Nano **10**, 1201–1209 (2016).

[79] F. Mohn, B. Schuler, L. Gross, and G. Meyer. *Different tips for high-resolution atomic force microscopy and scanning tunneling microscopy of single molecules.* Applied Physics Letters **102**, 073109 (2013).

[80] G. Meyer. *A simple low-temperature ultrahigh-vacuum scanning tunneling microscope capable of atomic manipulation.* Review of Scientific Instruments **67**, 2960–2965 (1996).

[81] K. Besocke. *An easily operable scanning tunneling microscope.* Surface Science **181**, 145–153 (1987).

[82] N. Pavliček. *Scanning Probe Methods Applied to Molecular Electronics.* Ph.D. thesis, Universität Regensburg (2013).

[83] F. J. Giessibl. *High-speed force sensor for force microscopy and profilometry utilizing a quartz tuning fork.* Applied Physics Letters **73**, 3956–3958 (1998).

[84] F. J. Giessibl. *Atomic resolution on Si(111)-(7×7) by noncontact atomic force microscopy with a force sensor based on a quartz tuning fork.* Applied Physics Letters **76**, 1470–1472 (2000).

[85] R. Bennewitz, M. Bammerlin, M. Guggisberg, C. Loppacher, A. Baratoff, E. Meyer, and H.-J. Güntherodt. *Aspects of dynamic force microscopy on NaCl/Cu(111): resolution, tip–sample interactions and cantilever oscillation characteristics.* Surface and Interface Analysis **27**, 462–466 (1999).

[86] F. Simbürger. *Atomic force microscopy of individual molecules in two different charge states.* Master's thesis, University of Regensburg (2017).

[87] N. S. Sariciftci, L. Smilowitz, A. J. Heeger, and F. Wudl. *Photoinduced Electron Transfer from a Conducting Polymer to Buckminsterfullerene.* Science **258**, 1474–1476 (1992).

[88] D. I. Gittins, D. Bethell, D. J. Schiffrin, and R. J. Nichols. *A nanometre-scale electronic switch consisting of a metal cluster and redox-addressable groups.* Nature **408**, 67–69 (2000).

[89] W. Haiss, H. van Zalinge, S. J. Higgins, D. Bethell, H. Höbenreich, D. J. Schiffrin, and R. J. Nichols. *Redox State Dependence of Single Molecule Conductivity.* Journal of the American Chemical Society **125**, 15294–15295 (2003).

[90] F. Chen, J. He, C. Nuckolls, T. Roberts, J. E. Klare, and S. Lindsay. *A Molecular Switch Based on Potential-Induced Changes of Oxidation State.* Nano Letters **5**, 503–506 (2005).

[91] K. Susumu, P. R. Frail, P. J. Angiolillo, and M. J. Therien. *Conjugated chromophore arrays with unusually large hole polaron delocalization lengths.* Journal of the American Chemical Society **128**, 8380–8381 (2006).

[92] G. R. Hutchison, M. A. Ratner, and T. J. Marks. *Hopping transport in con-*

ductive heterocyclic oligomers: reorganization energies and substituent effects. Journal of the American Chemical Society **127**, 2339–2350 (2005).

[93] S. Ho Choi, B. Kim, and C. D. Frisbie. *Electrical Resistance of Long Conjugated Molecular Wires.* Science **320**, 1482–1486 (2008).

[94] M. Sterrer, T. Risse, U. Martinez Pozzoni, L. Giordano, M. Heyde, H.-P. Rust, G. Pacchioni, and H.-J. Freund. *Control of the Charge State of Metal Atoms on Thin MgO Films.* Physical Review Letters **98**, 096107 (2007).

[95] Y.-S. Fu, T. Zhang, S.-H. Ji, X. Chen, X.-C. Ma, J.-F. Jia, and Q.-K. Xue. *Identifying Charge States of Molecules with Spin-Flip Spectroscopy.* Physical Review Letters **103**, 257202 (2009).

[96] J. Park, B. D. Yu, and H. Kim. *Charge and spin states of metal atoms adsorbed on ultrathin MgO/Fe(001) films.* Physical Review B **79**, 233407 (2009).

[97] S. J. van der Molen and P. Liljeroth. *Charge transport through molecular switches.* Journal of Physics: Condensed Matter **22**, 133001 (2010).

[98] B. Huang, H. Xiang, J. Yu, and S.-H. Wei. *Effective Control of the Charge and Magnetic States of Transition-Metal Atoms on Single-Layer Boron Nitride.* Physical Review Letters **108**, 206802 (2012).

[99] C. Uhlmann, I. Swart, and J. Repp. *Controlling the Orbital Sequence in Individual Cu-Phthalocyanine Molecules.* Nano Letters **13**, 777–780 (2013).

[100] J. Martínez-Blanco, C. Nacci, S. C. Erwin, K. Kanisawa, E. Locane, M. Thomas, F. von Oppen, P. W. Brouwer, and S. Fölsch. *Gating a single-molecule transistor with individual atoms.* Nature Physics **11**, 640–644 (2015).

[101] J. Repp, W. Steurer, I. Scivetti, M. Persson, L. Gross, and G. Meyer. *Charge-State-Dependent Diffusion of Individual Gold Adatoms on Ionic Thin NaCl Films.* Physical Review Letters **117**, 146102 (2016).

[102] A. Kumar, K. Banerjee, M. Dvorak, F. Schulz, A. Harju, P. Rinke, and P. Liljeroth. *Charge-Transfer-Driven Nonplanar Adsorption of F_4TCNQ Molecules on Epitaxial Graphene.* ACS Nano **11**, 4960–4968 (2017).

[103] C. Uhlmann. *Tieftemperatur-Rastertunnelmikroskopie an Phthalocyanin-Molekülen auf ultradünnen Isolatorfilmen: Ladungszustand, Jahn-Teller Effekt und ein molekularer Schalter.* Ph.D. thesis, Universität Regensburg (2013).

[104] V. Blum, R. Gehrke, F. Hanke, P. Havu, V. Havu, X. Ren, K. Reuter, and M. Scheffler. *Ab initio molecular simulations with numeric atom-centered orbitals.* Computer Physics Communications **180**, 2175–2196 (2009).

[105] J. Heyd, G. E. Scuseria, and M. Ernzerhof. *Hybrid functionals based on a screened Coulomb potential.* The Journal of Chemical Physics **118**, 8207–8215 (2003).

[106] A. Tkatchenko and M. Scheffler. *Accurate Molecular Van Der Waals Interactions from Ground-State Electron Density and Free-Atom Reference Data.* Physical Review Letters **102**, 073005 (2009).

[107] V. G. Ruiz, W. Liu, E. Zojer, M. Scheffler, and A. Tkatchenko. *Density-Functional Theory with Screened van der Waals Interactions for the Modeling of Hybrid Inorganic-Organic Systems.* Physical Review Letters **108**, 146103 (2012).

[108] S. Grimme. *Semiempirical GGA-type density functional constructed with a long-range dispersion correction.* Journal of Computational Chemistry **27**, 1787–1799 (2006).

[109] N. Moll, L. Gross, F. Mohn, A. Curioni, and G. Meyer. *A simple model of molecular imaging with noncontact atomic force microscopy.* New Journal of Physics **14**, 083023 (2012).

[110] C.-S. Guo, M. A. Van Hove, X. Ren, and Y. Zhao. *High-Resolution Model for Noncontact Atomic Force Microscopy with a Flexible Molecule on the Tip Apex.* The Journal of Physical Chemistry C **119**, 1483–1488 (2015).

[111] N. Moll, B. Schuler, S. Kawai, F. Xu, L. Peng, A. Orita, J. Otera, A. Curioni, M. Neu, J. Repp, G. Meyer, and L. Gross. *Image Distortions of a Partially Fluorinated Hydrocarbon Molecule in Atomic Force Microscopy with Carbon Monoxide Terminated Tips.* Nano Letters **14**, 6127–6131 (2014).

[112] M. P. Boneschanscher, S. K. Hämäläinen, P. Liljeroth, and I. Swart. *Sample corrugation affects the apparent bond lengths in atomic force microscopy.* ACS Nano **8**, 3006–3014 (2014).

[113] P. Hapala, M. Švec, O. Stetsovych, N. J. van der Heijden, M. Ondráček, J. van der Lit, P. Mutombo, I. Swart, and P. Jelínek. *Mapping the electrostatic force field of single molecules from high-resolution scanning probe images.* Nature Communications **7**, 11560 (2016).

[114] J. van der Lit, F. Di Cicco, P. Hapala, P. Jelinek, and I. Swart. *Submolecular Resolution Imaging of Molecules by Atomic Force Microscopy: The Influence of the Electrostatic Force.* Physical Review Letters **116**, 096102 (2016).

[115] M. T. Woodside and P. L. McEuen. *Scanned probe imaging of single-electron charge states in nanotube quantum dots.* Science **296**, 1098–1101 (2002).

[116] M. Rashidi, W. Vine, T. Dienel, L. Livadaru, J. Retallick, T. Huff, K. Walus, and R. A. Wolkow. *Initiating and Monitoring the Evolution of Single Electrons Within Atom-Defined Structures.* Physical Review Letters **121**, 166801 (2018).

[117] O. Krejčí, P. Hapala, M. Ondráček, and P. Jelínek. *Principles and simulations of high-resolution STM imaging with a flexible tip apex.* Physical Review B **95**, 045407 (2017).

[118] M. Corso, M. Ondráček, C. Lotze, P. Hapala, K. J. Franke, P. Jelínek, and J. I. Pascual. *Charge Redistribution and Transport in Molecular Contacts.* Physical Review Letters **115**, 136101 (2015).

[119] T. Trevethan and A. L. Shluger. *Modeling the Diffusive Motion of Large Organic Molecules on Insulating Surfaces.* The Journal of Physical Chemistry C **112**, 19577–19583 (2008).

[120] C. Barth, M. Gingras, A. S. Foster, A. Gulans, G. Félix, T. Hynninen, R. Peresutti, and C. R. Henry. *Two-Dimensional Nanostructured Growth of Nanoclusters and Molecules on Insulating Surfaces.* Advanced Materials **24**, 3228–3232 (2012).

[121] P. Rahe, M. Nimmrich, and A. Kühnle. *Substrate Templating upon Self-Assembly of Hydrogen-Bonded Molecular Networks on an Insulating Surface.* Small **8**, 2969–2977 (2012).

[122] C. M. Hauke, R. Bechstein, M. Kittelmann, C. Storz, A. F. M. Kilbinger, P. Rahe, and A. Kühnle. *Controlling Molecular Self-Assembly on an Insulating Surface by Rationally Designing an Efficient Anchor Functionality That Maintains Structural Flexibility.* ACS Nano **7**, 5491–5498 (2013).

[123] P. Rahe, M. Kittelmann, J. L. Neff, M. Nimmrich, M. Reichling, P. Maass, and A. Kühnle. *Tuning Molecular Self-Assembly on Bulk Insulator Surfaces by Anchoring of the Organic Building Blocks.* Advanced Materials **25**, 3948–3956 (2013).

[124] B. Hoff, M. Gingras, R. Peresutti, C. R. Henry, A. S. Foster, and C. Barth. *Mechanisms of the Adsorption and Self-Assembly of Molecules with Polarized Functional Groups on Insulating Surfaces.* The Journal of Physical Chemistry C **118**, 14569–14578 (2014).

[125] M.-S. Liao and S. Scheiner. *Electronic structure and bonding in metal phthalocyanines, Metal=Fe, Co, Ni, Cu, Zn, Mg.* The Journal of Chemical Physics **114**, 9780–9791 (2001).

[126] G. M. Whitesides, J. P. Mathias, and C. T. Seto. *Molecular self-assembly and nanochemistry: a chemical strategy for the synthesis of nanostructures.* Science **254**, 1312 (1991).

[127] M. Böhringer, K. Morgenstern, W.-D. Schneider, R. Berndt, F. Mauri, A. De Vita, and R. Car. *Two-Dimensional Self-Assembly of Supramolecular Clusters and Chains.* Physical Review Letters **83**, 324–327 (1999).

[128] J. V. Barth, J. Weckesser, C. Cai, P. Günter, L. Bürgi, O. Jeandupeux, and K. Kern. *Building supramolecular nanostructures at surfaces by hydrogen bonding.* Angewandte Chemie International Edition **39**, 1230–234 (2000).

[129] T. Yokoyama, S. Yokoyama, T. Kamikado, Y. Okuno, and S. Mashiko. *Selective*

assembly on a surface of supramolecular aggregates with controlled size and shape. Nature **413**, 619–621 (2001).

[130] J. V. Barth, J. Weckesser, N. Lin, A. Dmitriev, and K. Kern. *Supramolecular architectures and nanostructures at metal surfaces.* Applied Physics A **76**, 645–652 (2003).

[131] J. V. Barth. *Molecular Architectonic on Metal Surfaces.* Annual Review of Physical Chemistry **58**, 375–407 (2007).

[132] R. Temirov, S. Soubatch, A. Luican, and F. S. Tautz. *Free-electron-like dispersion in an organic monolayer film on a metal substrate.* Nature **444**, 350–353 (2006).

[133] C. Paris, A. Floris, S. Aeschlimann, M. Kittelmann, F. Kling, R. Bechstein, A. Kühnle, and L. Kantorovich. *Increasing the Templating Effect on a Bulk Insulator Surface: From a Kinetically Trapped to a Thermodynamically More Stable Structure.* The Journal of Physical Chemistry C **120**, 17546–17554 (2016).

[134] M. Kittelmann, P. Rahe, and A. Kühnle. *Molecular self-assembly on an insulating surface: interplay between substrate templating and intermolecular interactions.* Journal of Physics: Condensed Matter **24**, 354007 (2012).

[135] M. Kittelmann, P. Rahe, A. Gourdon, and A. Kühnle. *Direct Visualization of Molecule Deprotonation on an Insulating Surface.* ACS Nano **6**, 7406–7411 (2012).

[136] P. Rahe, R. Lindner, M. Kittelmann, M. Nimmrich, and A. Kühnle. *From dewetting to wetting molecular layers: C_{60} on CaCO3(10$\bar{1}$4) as a case study.* Physical Chemistry Chemical Physics **14**, 6544–6548 (2012).

[137] L. Nony, F. Bocquet, F. Para, F. Chérioux, E. Duverger, F. Palmino, V. Luzet, and C. Loppacher. *Dipole-driven self-organization of zwitterionic molecules on alkali halide surfaces.* Beilstein Journal of Nanotechnology **3**, 285–293 (2012).

[138] S. Kawai, A. Sadeghi, F. Xu, L. Peng, A. Orita, J. Otera, S. Goedecker, and E. Meyer. *Extended Halogen Bonding between Fully Fluorinated Aromatic Molecules.* ACS Nano **9**, 2574–2583 (2015).

[139] C. Bombis, N. Kalashnyk, W. Xu, E. Lægsgaard, F. Besenbacher, and T. R. Linderoth. *Hydrogen-Bonded Molecular Networks of Melamine and Cyanuric Acid on Thin Films of NaCl on Au(111).* Small **5**, 2177–2182 (2009).

[140] M. Fendrich and T. Kunstmann. *Organic molecular nanowires: N,N′-dimethylperylene-3,4,9,10-bis(dicarboximide) on KBr(001).* Applied Physics Letters **91**, 023101 (2007).

[141] S. A. Burke, W. Ji, J. M. Mativetsky, J. M. Topple, S. Fostner, H.-J. Gao, H. Guo, and P. Grütter. *Strain Induced Dewetting of a Molecular System: Bimodal Growth of PTCDA on NaCl.* Physical Review Letters **100**, 186104

(2008).

[142] C. Weiss, C. Wagner, R. Temirov, and F. S. Tautz. *Direct Imaging of Intermolecular Bonds in Scanning Tunneling Microscopy.* Journal of the American Chemical Society **132**, 11864–11865 (2010).

[143] E. Umbach, K. Glöckler, and M. Sokolowski. *Surface "architecture" with large organic molecules: interface order and epitaxy.* Surface Science **402-404**, 20 – 31 (1998).

[144] K. Glöckler, C. Seidel, A. Soukopp, M. Sokolowski, E. Umbach, M. Böhringer, R. Berndt, and W.-D. Schneider. *Highly ordered structures and submolecular scanning tunnelling microscopy contrast of PTCDA and DM-PBDCI monolayers on Ag(111) and Ag(110).* Surface Science **405**, 1–20 (1998).

[145] N. Kocić, D. Blank, P. Abufager, N. Lorente, S. Decurtins, S.-X. Liu, and J. Repp. *Implementing Functionality in Molecular Self-Assembled Monolayers.* Nano Letters **19**, 2750–2757 (2019).

[146] J. Schütte, R. Bechstein, M. Rohlfing, M. Reichling, and A. Kühnle. *Cooperative mechanism for anchoring highly polar molecules at an ionic surface.* Physical Review B **80**, 205421 (2009).

[147] B. Such, T. Trevethan, T. Glatzel, S. Kawai, L. Zimmerli, E. Meyer, A. L. Shluger, C. H. M. Amijs, P. de Mendoza, and A. M. Echavarren. *Functionalized Truxenes: Adsorption and Diffusion of Single Molecules on the KBr(001) Surface.* ACS Nano **4**, 3429–3439 (2010).

[148] K. A. Cochrane, A. Schiffrin, T. S. Roussy, M. Capsoni, and S. A. Burke. *Pronounced polarization-induced energy level shifts at boundaries of organic semiconductor nanostructures.* Nature Communications **6**, 8312 (2015).

[149] W. P. Davey. *Precision Measurements of the Lattice Constants of Twelve Common Metals.* Physical Review **25**, 753–761 (1925).

[150] C. Kittel. *Einführung in die Festkörperphysik.* Oldenburg Verlag München Wien, 14. edition (2006).

[151] W. Moritz and D. Wolf. *Structure determination of the reconstructed Au(110) surface.* Surface Science **88**, L29–L34 (1979).

[152] T. Gritsch, D. Coulman, R. J. Behm, and G. Ertl. *A scanning tunneling microscopy investigation of the structure of the Pt(110) and Au(110) surfaces.* Surface Science **257**, 297–306 (1991).

[153] T. L. Cocker, D. Peller, P. Yu, J. Repp, and R. Huber. *Tracking the ultrafast motion of a single molecule by femtosecond orbital imaging.* Nature **539**, 263 (2016).

[154] D. R. Lide (editor). *CRC Handbook of Chemistry and Physics.* CRC Press,

Boca Raton, Florida, 97. edition (2009).

[155] T. Dienel, C. Loppacher, S. C. B. Mannsfeld, R. Forker, and T. Fritz. *Growth-Mode-Induced Narrowing of Optical Spectra of an Organic Adlayer.* Advanced Materials **20**, 959–963 (2008).

[156] H. Karacuban, S. Koch, M. Fendrich, T. Wagner, and R. Möller. *PTCDA on Cu(111) partially covered with NaCl.* Nanotechnology **22**, 295305 (2011).

[157] J. Repp, G. Meyer, S. Paavilainen, F. E. Olsson, and M. Persson. *Imaging Bond Formation Between a Gold Atom and Pentacene on an Insulating Surface.* Science **312**, 1196–1199 (2006).

[158] K. Kimura, K. Miwa, H. Imada, M. Imai-Imada, S. Kawahara, J. Takeya, M. Kawai, M. Galperin, and Y. Kim. *Selective triplet exciton formation in a single molecule.* Nature **570**, 210–213 (2019).

[159] F. Mohn, J. Repp, L. Gross, G. Meyer, M. S. Dyer, and M. Persson. *Reversible Bond Formation in a Gold-Atom–Organic-Molecule Complex as a Molecular Switch.* Physical Review Letters **105**, 266102 (2010).

[160] H. Aldahhak, W. G. Schmidt, and E. Rauls. *Adsorption of PTCDA on NaCl(100) and KCl(100).* Surface Science **617**, 242–248 (2013).

[161] P. Scheuerer, L. L. Patera, and J. Repp. *Manipulating and Probing the Distribution of Excess Electrons in an Electrically Isolated Self-Assembled Molecular Structure.* Nano Letters **20**, 1839–1845 (2020).

[162] M. Koch, J. G. Keizer, P. Pakkiam, D. Keith, M. G. House, E. Peretz, and M. Y. Simmons. *Spin read-out in atomic qubits in an all-epitaxial three-dimensional transistor.* Nature Nanotechnology **14**, 137–140 (2019).

[163] E. C. P. Smits, S. G. J. Mathijssen, P. A. van Hal, S. Setayesh, T. C. T. Geuns, K. A. H. A. Mutsaers, E. Cantatore, H. J. Wondergem, O. Werzer, R. Resel, M. Kemerink, S. Kirchmeyer, A. M. Muzafarov, S. A. Ponomarenko, B. de Boer, P. W. M. Blom, and D. M. de Leeuw. *Bottom-up organic integrated circuits.* Nature **455**, 956–959 (2008).

[164] A. Bandyopadhyay, R. Pati, S. Sahu, F. Peper, and D. Fujita. *Massively parallel computing on an organic molecular layer.* Nature Physics **6**, 369–375 (2010).

[165] A. J. Heinrich, C. P. Lutz, J. A. Gupta, and D. M. Eigler. *Molecule Cascades.* Science **298**, 1381–1387 (2002).

[166] M. Fuechsle, J. A. Miwa, S. Mahapatra, H. Ryu, S. Lee, O. Warschkow, L. C. L. Hollenberg, G. Klimeck, and M. Y. Simmons. *A single-atom transistor.* Nature Nanotechnology **7**, 242–246 (2012).

[167] F. E. Kalff, M. P. Rebergen, E. Fahrenfort, J. Girovsky, R. Toskovic, J. L. Lado, J. Fernández-Rossier, and A. F. Otte. *A kilobyte rewritable atomic memory.*

Nature Nanotechnology **11**, 926 (2016).

[168] C. S. Lent, P. D. Tougaw, W. Porod, and G. H. Bernstein. *Quantum cellular automata.* Nanotechnology **4**, 49–57 (1993).

[169] C. S. Lent and P. D. Tougaw. *A device architecture for computing with quantum dots.* Proceedings of the IEEE **85**, 541–557 (1997).

[170] M. B. Haider, J. L. Pitters, G. A. DiLabio, L. Livadaru, J. Y. Mutus, and R. A. Wolkow. *Controlled Coupling and Occupation of Silicon Atomic Quantum Dots at Room Temperature.* Physical Review Letters **102**, 046805 (2009).

[171] T. Huff, H. Labidi, M. Rashidi, L. Livadaru, T. Dienel, R. Achal, W. Vine, J. Pitters, and R. A. Wolkow. *Binary atomic silicon logic.* Nature Electronics **1**, 636–643 (2018).

[172] T. Chassé, C.-I. Wu, I. G. Hill, and A. Kahn. *Band alignment at organic-inorganic semiconductor interfaces: α-NPD and CuPc on InP(110).* Journal of Applied Physics **85**, 6589–6592 (1999).

[173] S. D. Bennett, L. Cockins, Y. Miyahara, P. Grütter, and A. A. Clerk. *Strong Electromechanical Coupling of an Atomic Force Microscope Cantilever to a Quantum Dot.* Physical Review Letters **104**, 017203 (2010).

[174] M. Kisiel, O. O. Brovko, D. Yildiz, R. Pawlak, U. Gysin, E. Tosatti, and E. Meyer. *Mechanical dissipation from charge and spin transitions in oxygen-deficient $SrTiO_3$ surfaces.* Nature Communications **9**, 2946 (2018).

[175] M. Schneiderbauer, M. Emmrich, A. J. Weymouth, and F. J. Giessibl. *CO Tip Functionalization Inverts Atomic Force Microscopy Contrast via Short-Range Electrostatic Forces.* Physical Review Letters **112**, 166102 (2014).

[176] R. Smoluchowski. *Anisotropy of the Electronic Work Function of Metals.* Physical Review **60**, 661–674 (1941).

[177] G. Teobaldi, K. Lämmle, T. Trevethan, M. Watkins, A. Schwarz, R. Wiesendanger, and A. L. Shluger. *Chemical Resolution at Ionic Crystal Surfaces Using Dynamic Atomic Force Microscopy with Metallic Tips.* Physical Review Letters **106**, 216102 (2011).

[178] L. Gross, B. Schuler, F. Mohn, N. Moll, N. Pavliček, W. Steurer, I. Scivetti, K. Kotsis, M. Persson, and G. Meyer. *Investigating atomic contrast in atomic force microscopy and Kelvin probe force microscopy on ionic systems using functionalized tips.* Physical Review B **90**, 155455 (2014).

[179] D. Z. Gao, J. Grenz, M. B. Watkins, F. Federici Canova, A. Schwarz, R. Wiesendanger, and A. L. Shluger. *Using Metallic Noncontact Atomic Force Microscope Tips for Imaging Insulators and Polar Molecules: Tip Characterization and Imaging Mechanisms.* ACS Nano **8**, 5339–5351 (2014).

[180] P. Yu, N. Kocić, J. Repp, B. Siegert, and A. Donarini. *Apparent Reversal of Molecular Orbitals Reveals Entanglement.* Physical Review Letters **119**, 056801 (2017).

[181] M. Alemani, M. V. Peters, S. Hecht, K.-H. Rieder, F. Moresco, and L. Grill. *Electric Field-Induced Isomerization of Azobenzene by STM.* Journal of the American Chemical Society **128**, 14446–14447 (2006).

[182] N. Kocić, P. Weiderer, S. Keller, S. Decurtins, S.-X. Liu, and J. Repp. *Periodic Charging of Individual Molecules Coupled to the Motion of an Atomic Force Microscopy Tip.* Nano Letters **15**, 4406–4411 (2015).

[183] C. Wöll, S. Chiang, R. J. Wilson, and P. H. Lippel. *Determination of atom positions at stacking-fault dislocations on Au(111) by scanning tunneling microscopy.* Physical Review B **39**, 7988–7991 (1989).

[184] I. Swart, T. Sonnleitner, J. Niedenführ, and J. Repp. *Controlled Lateral Manipulation of Molecules on Insulating Films by STM.* Nano Letters **12**, 1070–1074 (2012).

[185] C. Wagner, M. F. B. Green, P. Leinen, T. Deilmann, P. Krüger, M. Rohlfing, R. Temirov, and F. S. Tautz. *Scanning Quantum Dot Microscopy.* Physical Review Letters **115**, 026101 (2015).

[186] B. C. Stipe, M. A. Rezaei, W. Ho, S. Gao, M. Persson, and B. I. Lundqvist. *Single-Molecule Dissociation by Tunneling Electrons.* Physical Review Letters **78**, 4410–4413 (1997).

[187] S.-W. Hla, L. Bartels, G. Meyer, and K.-H. Rieder. *Inducing All Steps of a Chemical Reaction with the Scanning Tunneling Microscope Tip: Towards Single Molecule Engineering.* Physical Review Letters **85**, 2777–2780 (2000).

[188] H.-J. Shin, J. Jung, K. Motobayashi, S. Yanagisawa, Y. Morikawa, Y. Kim, and M. Kawai. *State-selective dissociation of a single water molecule on an ultrathin mgo film.* Nature Materials **9**, 442–447 (2010).

[189] Y. Jiang, Q. Huan, L. Fabris, G. C. Bazan, and W. Ho. *Submolecular control, spectroscopy and imaging of bond-selective chemistry in single functionalized molecules.* Nature Chemistry **5**, 36–41 (2013).

List of Figures

Abbreviations

AC-STM	alternate-current scanning tunneling microscopy
AFM	atomic force microscope/microscopy
AM	amplitude modulation
CPD	contact potential difference
CuPc	copper(II)phthalocyanine
DFT	density functional theory
fcc	face centered cubic
FM	frequency modulation
FM-AFM	frequnecy-modulated atomic force microscopy
HOMO	highest occupied molecular orbital
KPFS	Kelvin probe force spectroscopy
LCPD	local contact potential difference
LDOS	local density of states
LUMO	lowest unoccupied molecular orbital
ML	monolayer(s)
PTCDA	perylene-3,4,9,10-tetracarboxylic dianhydride
QCA	quantum cellular automata
SOMO	singly occupied molecular orbital
SPM	scanning probe microscope/microscopy
STM	scanning tunneling microscope/microscopy
SUMO	singly unoccupied occupied molecular orbital
vdW	van der Waals

Acknowledgement

Finally, I want to express my gratitude to all persons who supported me during this work.

My special thanks goes to Prof. Dr. Jascha Repp for giving me the opportunity to do research in his group, and for the excellent supervision and education during the past years. He was always a patient mentor and always found time for enlightening discussions.

Further, I want to thank the other members of team AC-STM, Dr. Fabian Queck, and Dr. Laerte Patera. Working together in the lab was not only productive, I also enjoyed the time. Fabian was always putting a lot of effort into creating a good working climate and took care of our group excursions. Thanks to Laerte for his introduction into Italian cooking.

Also, I want to express my gratitude to Christoph Rohrer for technical support. He even made the countless maintenances in the beginning of the last year somewhat enjoyable. Thanks to Thomas Buchner, for the many scientific discussions and for sharing his broad knowledge of physics with me. I also acknowledge Tom and Chris for occasionally motivating me for having an after-work beer with them.

I am also indebted to Dr. Florian Albrecht, who always willingly shared his rich experience in AFM and STM with me, since I joined the group as a master student. I also liked listening to his passionate stories about chicken.

Thanks to Dr. Nemanja Kocić for proof reading this thesis and for scientific discussions.

I also thank, Tobias Preis, Gerhard Münnich, Andreas Pöllmann, Felix Simbürger, Nicole Kellner, Christoph Zernack, Sujoy Karan, Sophia Sokolov, and all other current and former members of the group.

I want to express my gratitude to Dr. Nikolaj Moll for the theoretical support in the CuPc charging project.

I acknowledge financial funding and training by the RTG 1570 during the first three years of my work.

My deepest thanks goes to my wife Judith, who always supported me. Thank you for accepting that I invested also some weekends in the lab instead of spending time with you, and for cheering me up and motiving me during the hard days.